Phosphonic Acid Dipole Layers for Band Edge Engineering of WO_3 and p-Si/TiO_2 Photoelectrochemical Devices

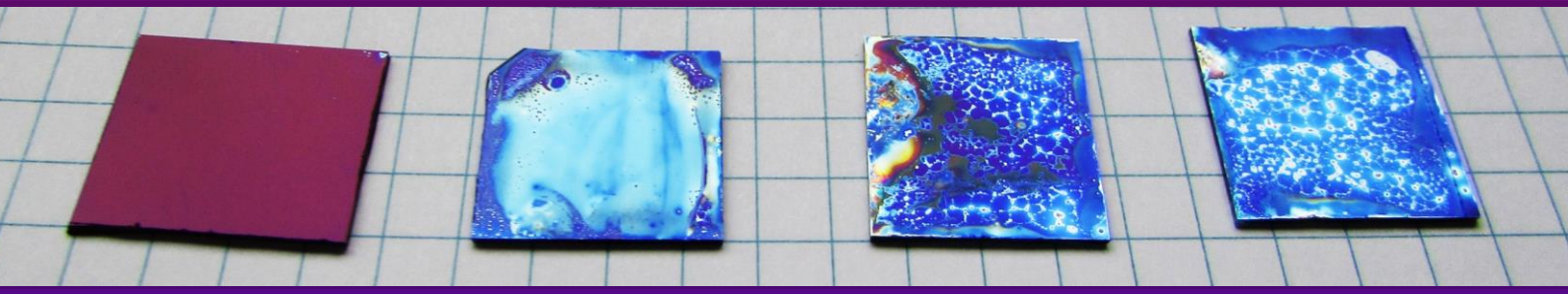

DISSERTATION
RENÉ WICK
2019

University of Zurich[UZH]

Phosphonic Acid Dipole Layers for Band Edge Engineering of WO_3 and p-Si/TiO_2 Photoelectrochemical Devices

---

Dissertation

zur

Erlangung der naturwissenschaftlichen Doktorwürde

(Dr. sc. nat.)

vorgelegt der

Mathematisch-naturwissenschaftlichen Fakultät

der

Universität Zürich

von

René Wick

von

Zuzwil (SG)

Promotionskommission

Prof. Dr. David Tilley (Vorsitz)

Prof. Dr. Roger Alberto

Prof. Dr. Jürg Osterwalder

Zürich, 2019

Für Evelyne und Noelia

Table of contents

Summary

The photovoltage, and therefore the efficiency, of any photovoltaic or photoelectrochemical device is critically dependent on the semiconductor's band positions. This thesis presents a strategy to increase the photovoltage in heterojunction devices for photoelectrochemical water splitting by dipole molecule assisted band engineering. Some initial studies were conducted on model metal oxide WO_3, onto which different substituted phosphonic acid dipole molecules were grafted. This system allowed us to draw some first conclusions: band engineering is possible, but stability is a critical factor and the band shift is only favorable for p-type substrates, not n-type. We therefore switched to p-Si as a substrate, which was then modified with a phosphonic acid (H_3PO_3) dipole layer and protected by a corrosion resistant TiO_2 layer. We have successfully shown that devices with a phosphonic acid layer exhibit a 200 mV larger photovoltage as compared to devices without phosphonic acid. p-Si and TiO_2 form a heterojunction, which can be operated as a photoelectrochemical device and also as a photovoltaic cell by depositing a different front contact. Herein, we demonstrate that the phosphonic acid layer strategy is applicable to both device types, giving equally large photovoltage increases for photoelectrochemical as well as photovoltaic devices. For both device types, the phosphonic layer does not negatively effect the stability of the devices, since the dipole layer is well protected by TiO_2. Multiple experiments as well as calculations support our theory that this effect arises from the phosphonic acid acting as a dipole by changing the electron density on the surface of the substrate. By varying the thickness of the phosphonic acid layer, we were able to precisely tune the magnitude of the band shift and therefore the photovoltage. In a last step, we applied the method to emerging photoabsorber materials such as Cu_2O and Sb_2Se_3, which also showed a photovoltage increase upon modification by a phosphonic acid layer. We envision that this method will be widely adopted as a simple and powerful new method for fine-tuning the efficiency of heterojunction photoelectrochemical and photovoltaic materials.

Abbreviations

ABPE	applied bias photon-to-current efficiency
AFM	atomic force microscopy
ALD	atomic layer deposition
AZO	aluminum doped zinc oxide
CB, E_{cb}	conduction band/ conduction band energy
CIGS	copper indium gallium (di)selenide (PV material)
DFT	density functional theory
E_{EA}	electron affinity
ED	electrodeposition
EDX	energy-dispersive X-ray spectroscopy
E_f	Fermi level
E_g	band gap
eV	electron volt
E_{vac}	local vacuum energy level
FF	fill factor
FTO	fluorine doped tin oxide
HOMO	highest occupied molecular orbital
IR	infrared (spectroscopy)
ITO	indium doped tin oxide
J-V curve	current density – voltage curve
J_{sc}	short circuit current density
KPFM	Kelvin probe force microscopy
M-S analysis	Mott-Schottky analysis
MS, HR-ESI-MS	mass spectroscopy, high resolution electron spray ionization-MS
Mtoe	million tons of oil equivalent
n-doping	adding extra electrons to a semiconductor
N_A N_D	acceptor density, donor density
p-doping	adding extra holes to a semiconductor
P3HT	poly(3-hexylthiophen-2,5-diyl)

PA	phosphonic acid (H_3PO_3); for substituted phosphonic acids see abbreviations in Figure 28 and Figure 29
PEC	photoelectrochemistry
PEG	polyethyleneglycole
ppm	parts per million
PV	photovoltaics
QD, QDPV	quantum dots, quantum dot photovoltaics
RHE, V_{RHE}	reversible hydrogen electrode, potential of RHE
SEM	scanning electron microscopy
T-BAG	tethering by aggregation and growth
TCO	transparent and conductive oxide
TDMAT	tetrakis(dimethylamido)titanium
TW, TWh	terawatt, terawatt hours
VB, E_{vb}	valence band, valence band energy
V_{bb}	band bending
V_{bi}	built-in potential
V_{oc}	open circuit voltage
V_{onset}	onset potential of the photocurrent
XPS	X-ray photoelectron spectroscopy

1 Introduction

1.1 Broader context

With increasing standard of living, our demand for energy has steadily increased in the past. In recent years, we have reached a turning point in many high-income societies, where the energy consumption per capita started to slowly decrease for the first time in centuries, due to technological advancements (improved insulation in buildings, more efficient cars and machines, etc.).[1] In large parts of the world, however, the population is still growing and will continue to do so in the next decades. The United Nations estimate a population of 10 – 16 billion people, strongly dependent on the scenario used.[2] The good news is that it is expected that many people living in low- and middle income countries will be able to improve their standard of living significantly and it's obvious that they will need energy to do so.[3] Figure 1A shows the global primary energy consumption as reported by the International Energy Association (IEA), which was 13'600 Mtoe in 2015 and is expected to increase to 18'000 Mtoe in 2040.[4] This figure also breaks down the primary energy consumption into the different energy carriers. The combustion of coal, oil and gas makes up more than 80% of the total energy supply, while nuclear power provides another 5%, hydropower supplies 2.5% and burning of biomass delivers roughly 10%. The remaining 1.5% contain geothermal, wind and solar energy. There are certain complications associated with our strong dependency on the fossil fuels. First of all, they are not renewable, meaning that we are burning resources in a short time that took millions of years to form.

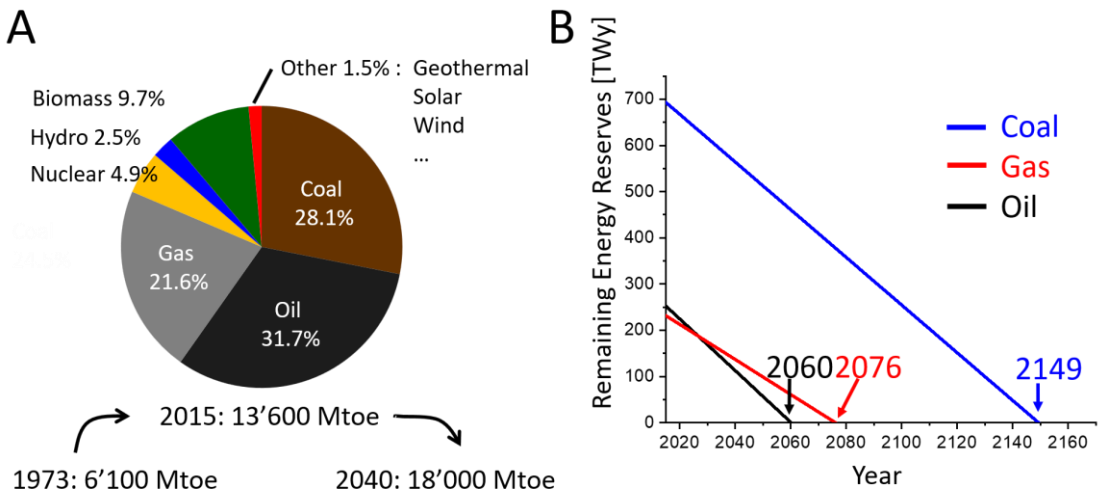

Figure 1. A: Breakdown of primary energy carriers for the global energy supply in 2015.[4] B: Fossil fuel reserves[5] divided by global consumption.[4]

Figure 1B depicts a very simplistic calculation of how long the fuel reserves will last if we constantly use as much as in 2015. While the number for fossil fuel reserves already includes estimates on

reserves that will be discovered in the future, it is predicted that the consumption will increase in the upcoming decades. Therefore, if fuel consumption keeps increasing, it is likely that the fuel reserves will run out even faster than calculated in Figure 1B, namely in a few decades for oil and gas and roughly a century for coal.

Nowadays, a vast majority of scientist (>97%) state that global warming is "extremely likely due to human activities".[6,7] This overwhelming consensus was reached in large parts thanks to the measurements of CO_2 concentrations in the atmosphere over decades by Charles David Keeling. The famous Keeling Curve presented in Figure 2A shows the atmospheric CO_2 concentration over the last 2000 years and the very steep increase since the beginning of the industrialization. Data reaching back 1 million years show that CO_2 levels have always fluctuated with ice ages and warmer periods, but CO_2 concentrations have never exceeded 300 ppm. Changes have never been as drastic as in the last centuries and mainly since 1950. Since roughly 30 years, the Scripps institute also measures O_2 concentrations, where small changes are much harder to detect since the atmosphere contains 21% O_2. The CO_2 and O_2 concentrations depicted in Figure 2B correlate strongly, providing further evidence that combustion of fossil fuels cause the CO_2 increase. CO_2 in the atmosphere absorbs infrared radiation and is therefore a major cause for anthropogenic global warming.[8]

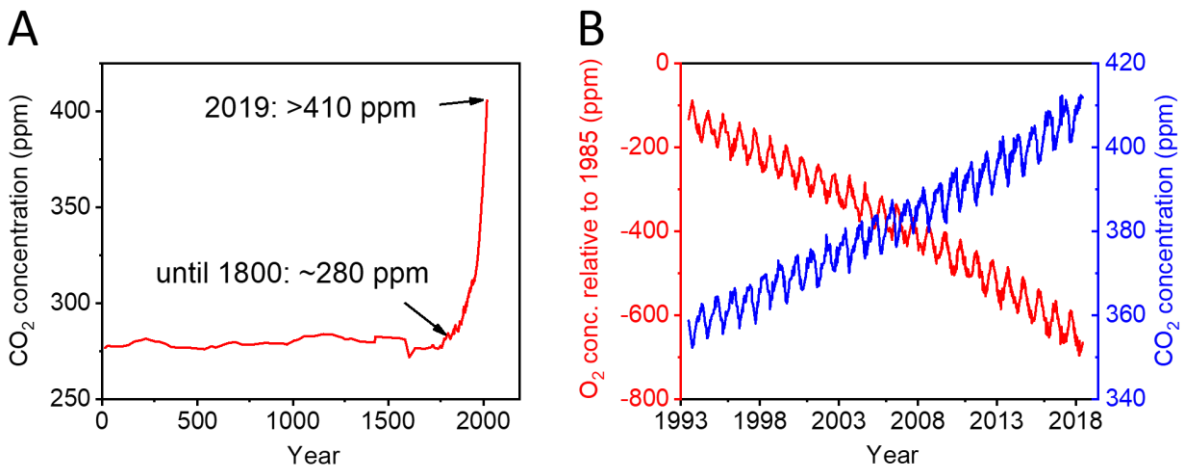

Figure 2. A: CO_2 concentration over the last 2000 years. After 1958: Measured on Mauna Loa, Hawaii.[9] Before 1958: Ice-core data.[10,11]

Huber and Knutti put it this way:

The warming induced by CO_2 will also persist for at least a thousand years as a result of the slow ocean carbon uptake, far longer than the warming from most other forcing agents. This emphasizes the need to focus on CO_2 in mitigating climate change.[8]

Luckily, there are several renewable alternatives to fossil fuels, some of which are listed in Figure 3.[12] If a large fraction of the future energy should be generated renewably, a combination of all possibilities seems to be the best option, with a focus on one or the other depending on the geographical, geological, climatical circumstances. However, the solar energy striking earth's surface is 86'000 TW and therefore orders of magnitude more than all other renewables combined and techniques harvesting the solar irradiation will most likely be the backbone of a renewable society, with wind, geothermic, hydroelectric and others acting as a support where it is locally appropriate.

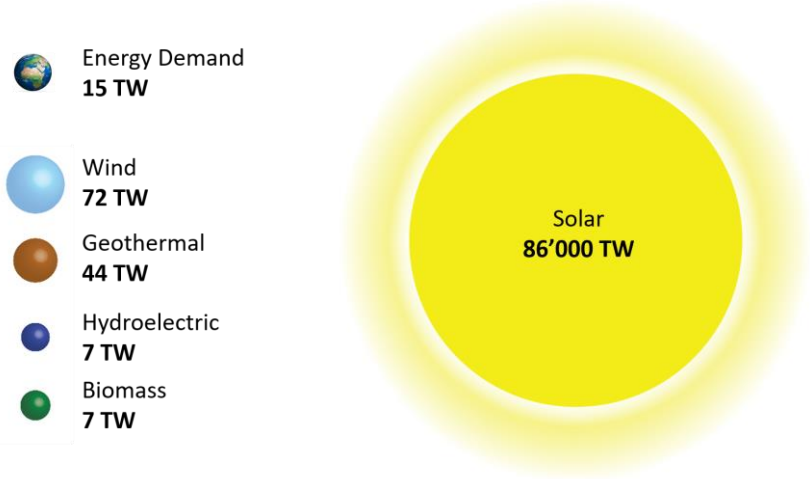

Figure 3. Global primary energy demand in 2015[4] and the most important renewable energy sources with their potential power output.[12]

The two most mature technologies for solar energy harvesting are photovoltaics and solar thermal. For both of them, power plants with hundreds of MW power as well as residential installations are in operation. Photovoltaic cells absorb photons to generate electricity as explained in detail below. Solar thermal devices (which will not be explained in detail here) absorb sunlight and heat up during that process. The heat is then used to directly heat buildings or water or another medium, which can then be used to generate electricity.

The largest drawback of technologies using sunlight is that the sun is not always shining, and day/night as well as summer/winter cycles have to be accounted for. On sunny days in summer, large amounts of PV electricity can easily overload the electrical grids, while no electricity is generated during nighttime. Two solutions for this are large batteries and pumped-storage hydro power plants. However, both options are not feasible for storage in the TWh magnitude either due to cost and

abundancy of the materials (batteries) or geographical and ecological reasons (pumped-storage power plants). A more favorable and scalable method is the conversion of solar energy into a solar fuel, with hydrogen being an attractive primary target. On one hand, H_2 can be produced by coupling an electrolyzer to a PV power plant (Figure 4A). Alternatively, photoelectrochemical cells (PEC cells) directly convert solar energy into chemical energy as explained in the next subchapter. PV as well as water electrolysis are well established, but there is currently no large-scale electrolyzer facility running solely on solar electricity, since electrolyzers usually degrade when not in use. PEC, however, is less mature, but has the potential of being significantly cheaper while using less material in the future.[13] Hydrogen is a candidate to be the fuel of the future since its applications are very extensive. As depicted in Figure 4B, it is used in fuel cells, which is also a commercial technology. Furthermore, H_2 can be converted into liquid fuels using well established processes such as the Fischer-Tropsch reaction, which converts H_2 and CO into longer chain hydrocarbons.[14] Large amounts of H_2 are also used in the Haber-Bosch process, converting H_2 and N_2 into NH_3, which is used to produce fertilizers.[15] Furthermore, hydrogen is required as a reactant in numerous reactions in the chemical and pharma industries.

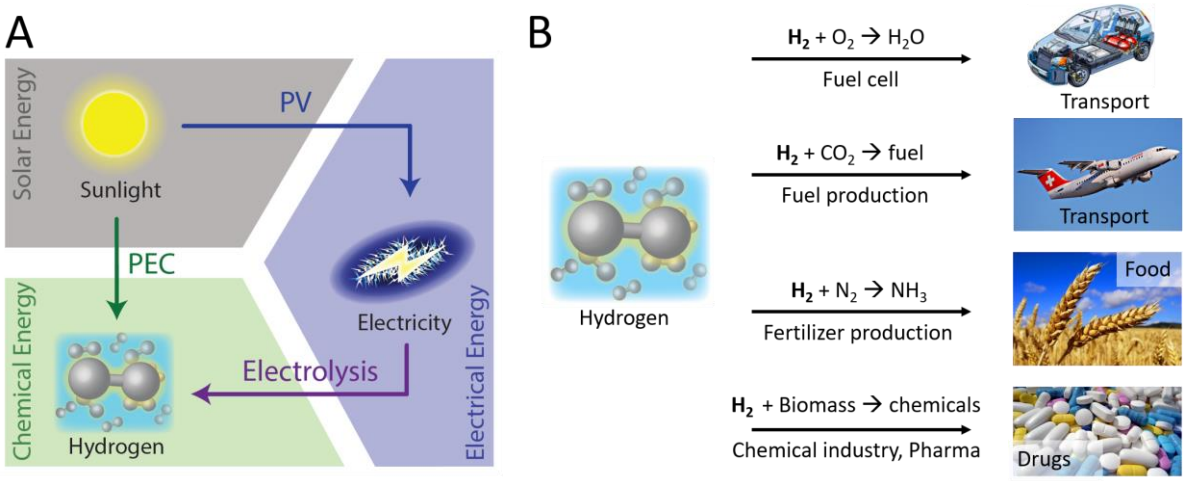

Figure 4. A: Generation of hydrogen by different pathways. Either directly (PEC) or indirectly (PV/electrolysis). B: different uses of H_2.

1.2 PV and PEC

According to Bohr's model of the atom, an atom's electrons are located in atomic shells with a certain energy level (Figure 5). If two atoms are brought closely together, the atoms interact and each energy level splits into two energy states. In a crystal, an almost infinite number of atoms interact, the

resulting energy levels are extremely close together and are therefore called energy bands.

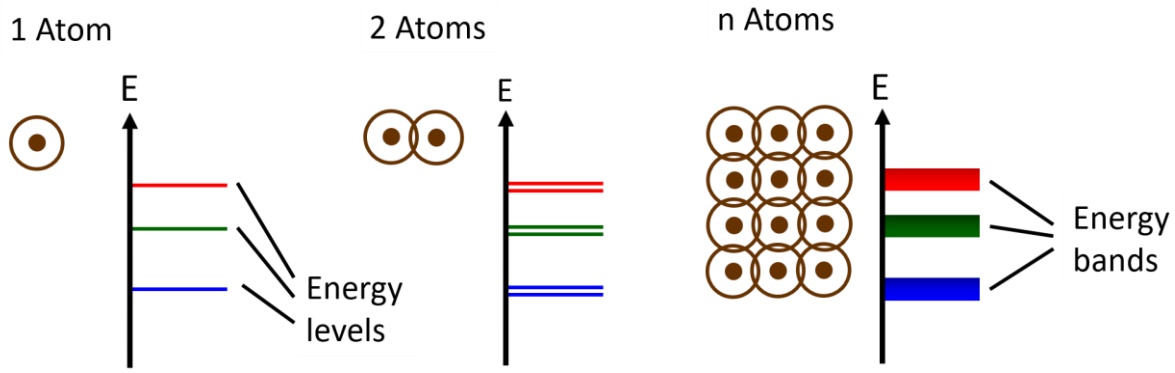

Figure 5. Interaction of atoms leads to splitting of the energy levels, leading to continuous energy bands if n → ∞. Adapted from ref 16.

The highest band occupied by electrons is called valence band (VB), while the lowest unoccupied band is called conduction band (CB). For an electron to jump from VB to CB, it has to overcome the band gap (E_g), the energy difference between VB and CB. If E_g is large (>3 eV), CB is empty even at room temperature, and the material is an insulator. Semiconductors are also insulating at low temperatures, but at higher temperatures (room temperature for example), the thermal energy is enough to promote some electrons into CB, since E_g is smaller ($0 < E_g < 3$ eV). The conductivity therefore increases with temperature. Metals, however, are conductive even at low temperatures since their CB and VB overlap.

A simplified two dimensional representation of Si, the best-studied and also commercially most important semiconductor, is represented in Figure 6A. Si wafers, such as in Figure 6B, were used in this thesis to a large extent.

If a semiconductor absorbs a photon with enough energy, an electron is excited from VB to CB, leaving a hole (h^+) behind in VB. In the case depicted in Figure 6C, the electron (hole) can diffuse in CB (VB), but has no driving force to preferentially go in one direction. On average, the electron flow will therefore be zero and the potential on both sides of the semiconductor will be equal. This can easily be demonstrated by holding the multimeter test probes against the front and back side if of a Si wafer (undoped, n- or p-doped). The measured voltage will hardly change when the Si wafer is illuminated, suggesting that no photovoltage is generated since the photoexcited electrons have no preferred

direction (Figure 6D). This device is certainly not a functioning solar cell.

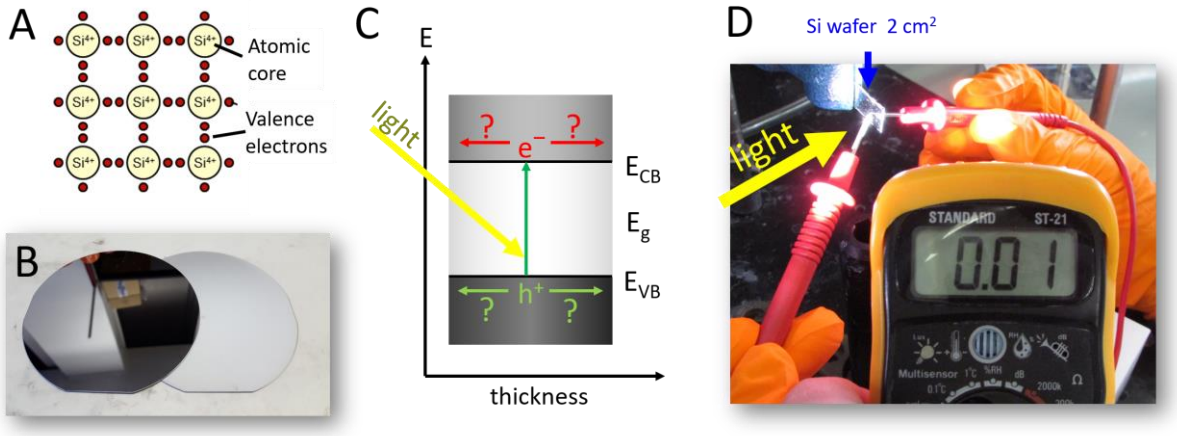

Figure 6. Two dimensional representation of a Si crystal (adapted from ref 16). B: Commercial 4 inch Si wafers with a polished front side and unpolished back side. C: Energy diagram for a semiconductor. D: n-Si is illuminated and the photovoltage between front and back side is measured with a multimeter. The photovoltage is almost zero, since the photogenerated charges have no preferred direction.

Semiconductors mainly gained so much importance over the last decades because one can influence their conductivity by doping. In order to do so, atoms of different elements are introduced into the semiconductor lattice. In the case of Si (with 4 valence electrons) doping with phosphorus atoms (with 5 valence electrons) will result in a free electron in the crystal lattice, since only 4 of P's electrons can be used for the bonds to neighboring Si atoms. The extra electron is only loosely bound to P and is mobile at room temperature (Figure 7A), leaving behind a localized positive charge on the P. The mobile electrons drastically increase the material's conductivity.

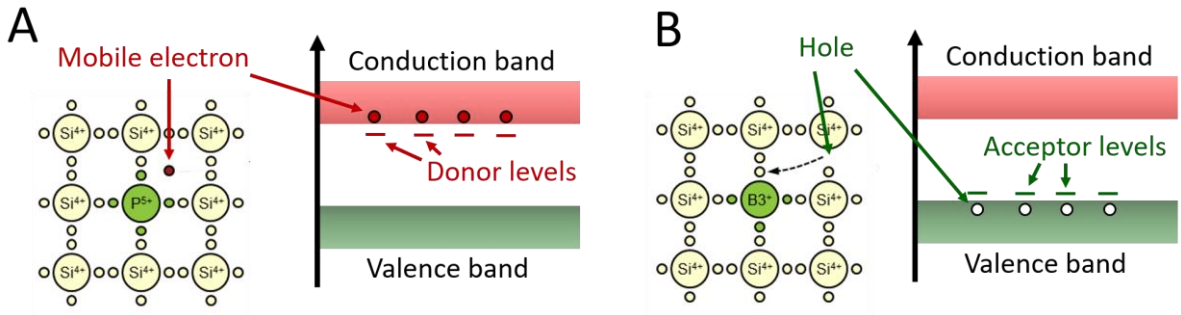

Figure 7. A: n-type doping of Si. Phosphorus has 5 valence electron, one of which is not needed for bonding and is therefore mobile. This creates donor levels in the band diagram, which are close to the conduction band. B: p-type doping of Si. Boron only has 3 valence electrons and one bond will not be occupied. A neighboring electron can fill this bond and create a mobile hole. In the band diagram, this manifests as acceptor levels close to the valence band. Figure adapted from ref 16.

The same effect can be obtained by replacing some Si sites by boron atoms with only 3 valence electrons. One bond to the neighboring Si atoms therefore remains unoccupied and can be filled with an electron from the valence band, which will then leave a hole. This hole is mobile at room temperature while the remaining negative charge on the B is stationary (Figure 7B). The strength of doping is revealed when n- and p-type doped semiconductors are brought into contact, forming a so called pn-junction. When n- and p-doped sides are the same material this is called a homojunction, while two different materials form a heterojunction.

In the moment after contact, electrons from the electron-rich n-type material flow to the electron-poor p-type material, where they recombine with mobile holes. This effect is driven by diffusion and therefore called diffusion current. The remaining stationary charges (positive in n-doped and negative in p-doped) cannot recombine and start forming an electric field which induces a field current in the opposite direction of the diffusion current. Therefore, when diffusion current = field current, an equilibrium is reached and not all mobile electrons recombine with all mobile holes, only the ones within a certain distance from the interface (Figure 8).

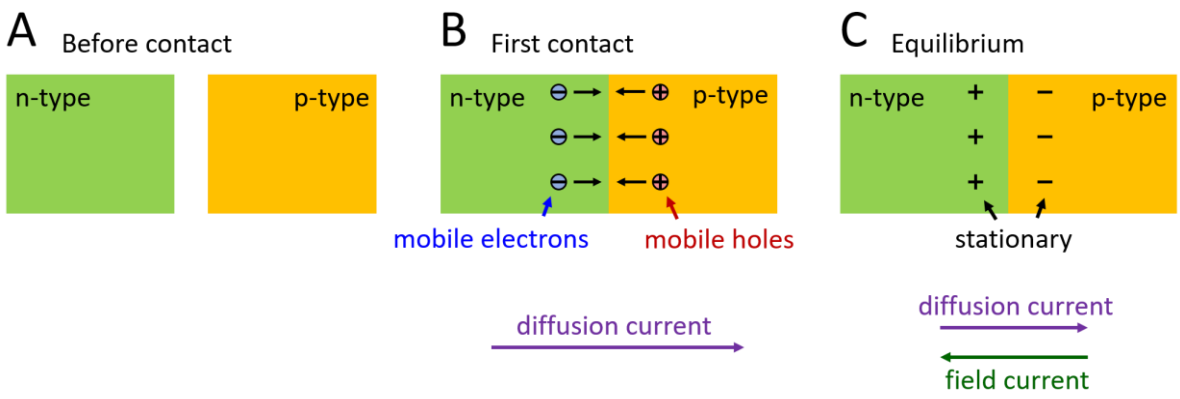

Figure 8. A: n- and p-type materials before contact. B: Upon contact, the diffusion current will drive mobile electrons from the bulk of the n-type to the interface where they recombine with mobile holes from the p-type bulk. C: This process leaves behind stationary charges on both sides, forming an electric field which drives charges in the opposite direction of the diffusion. The equilibrium is reached when diffusion current = field current.

For the next steps, a new concept has to be introduced: the Fermi level (E_f). Named after the Italian Noble laureate Enrico Fermi, this energy level is defined as the energy level with a probability of 50% of being occupied. In an ideal, undoped semiconductor this energy level lies exactly half-way between VB (filled) and CB (empty). As depicted in Figure 9A–B, E_f moves closer to CB, when a material is n-type doped and closer to VB if it's p-type doped, since the shallow donor or acceptor states (Figure 7) increase or decrease electron concentration. If the density of states (N_0) as well as donor- or acceptor density (N_D, N_A) are known, the energy difference between E_f and E_{cb} (or E_f and E_{vb}) can be calculated

according to the equations given in Figure 9. When n- and p-type materials are contacted, electrons and holes will recombine as already described in Figure 8. In equilibrium, E_f is constant across the whole device, as drawn in Figure 9C. This will lead to a potential change in CB and VB, which is called band bending. The band bending also represents the electric field and is strongest where the electric field is strongest, at the interface between n- and p-type materials. The potential step or built-in voltage (V_{bi}) can be quantified by subtracting ΔE between E_f and E_{cb} as well as E_f and E_{vb} from E_g. V_{bi} is also the maximal voltage that can be obtained as photovoltage if the pn-junction is used as a PV cell.

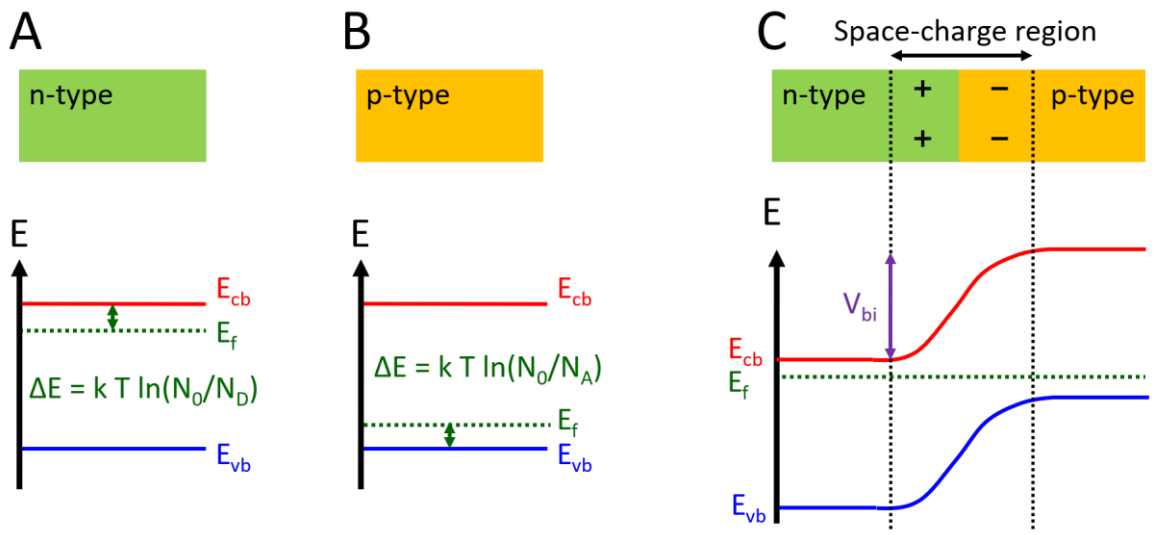

Figure 9. A: In a n-type material, E_f is close to E_{cb}. B: in p-type materials, E_f is close to E_{vb}. C: Bringing n- and p-type in contact equilibrates E_f throughout the pn- junction and leads to band bending within the space-charge region. The difference between E_f in n- and p-type before contact will then be the built-in potential (V_{bi}).

The electric field within the pn-junction (represented as band bending), allows the separation of light-generated charges. The absorption of a photon will generate an electron-hole-pair and under the influence of the electric field, the electron will be driven towards the n-type side, while the hole will migrate to the p-type side (Figure 10A). If both sides of a pn-junction are connected to a multimeter or potentiostat, a photovoltage can be measured upon light illumination (Figure 10B), representing a very basic PV cell.

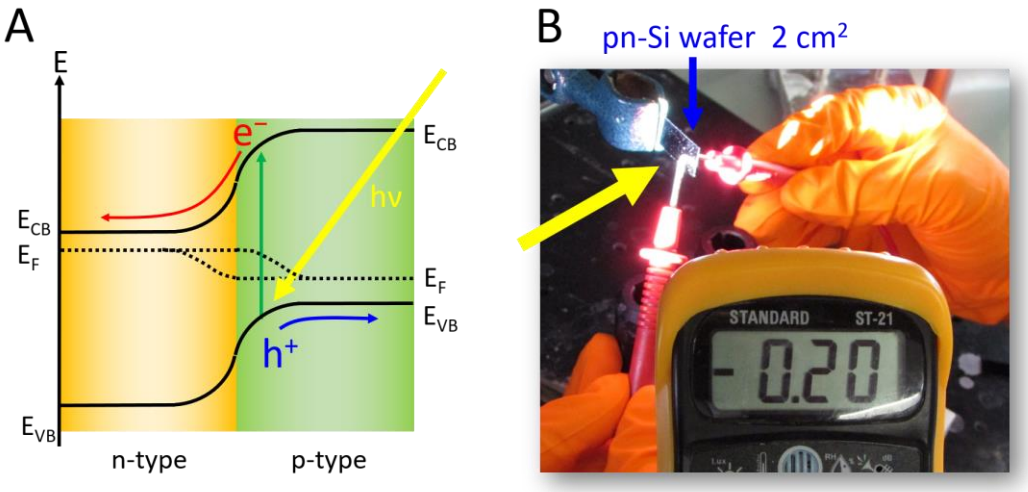

Figure 10. A: Band diagram of a pn-junction under illumination. A photon excited an electron into CB, leaving behind a hole in VB. Under the influence of the electric field, the charges are separated and a photovoltage as well as photocurrent can be measured by the help of a multimeter (B).

Photoelectrochemical (PEC) cells share many similarities with PV cells. They also need an internal electric field to separate photo-generated charges. This is achieved by immersing a semiconductor into an electrolyte. E_f of the semiconductor will equilibrate with the redox potential of the electrolyte. In case of an n-type semiconductor, electrons will flow into electrolyte, leading to band bending that drives photogenerated electrons to the back of the semiconductor and holes towards the surface and into the electrolyte, and vice versa for p-doped semiconductors (Figure 11). The band bending (V_{bb}) and therefore the maximum obtainable photovoltage in those devices is the difference between the fermi level of the semiconductor and the redox potential of the solution.

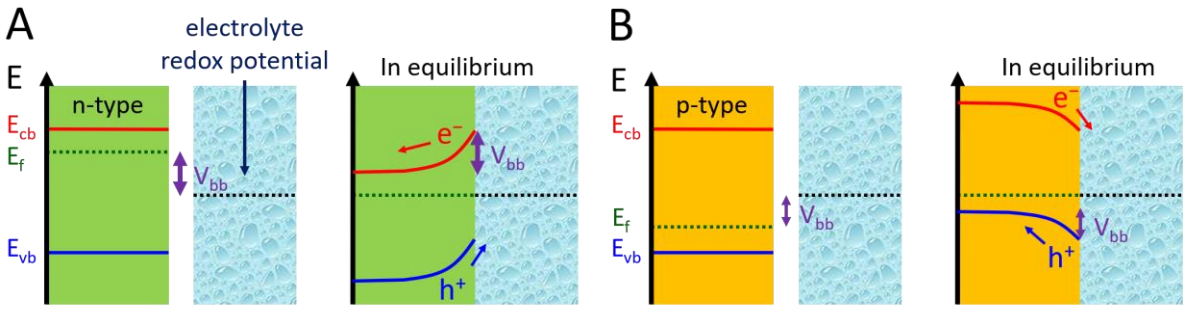

Figure 11. Semiconductor/electrolyte junction formation for n-doped semiconductor (A) and p-doped (B).

In a PEC cell, the potential difference between photoexcited electrons and holes is used to drive chemical reactions. At the (photo)cathode, electrons drive a reduction and at the (photo)anode, holes drive an oxidation. Figure 12 depicts the working principle of PEC water splitting. The photoanode is

brought in contact with the acidic electrolyte and an electric field (band bending) is formed. A photon is absorbed and excites an electron into CB, leaving a hole behind in VB. The hole is driven to the semiconductor/electrolyte junction and oxidizes water to O_2. The photoexcited electron moves to the back contact and through a wire to the cathode where it reduces protons to H_2. For the reactions to take place, the hole has to be at lower energy than the $H_2O \rightarrow O_2$ redox potential (1.23 V_{RHE}) and the photoexcited electron has to be higher in energy than the redox potential of $H^+ \rightarrow H_2$ (0 V_{RHE}).

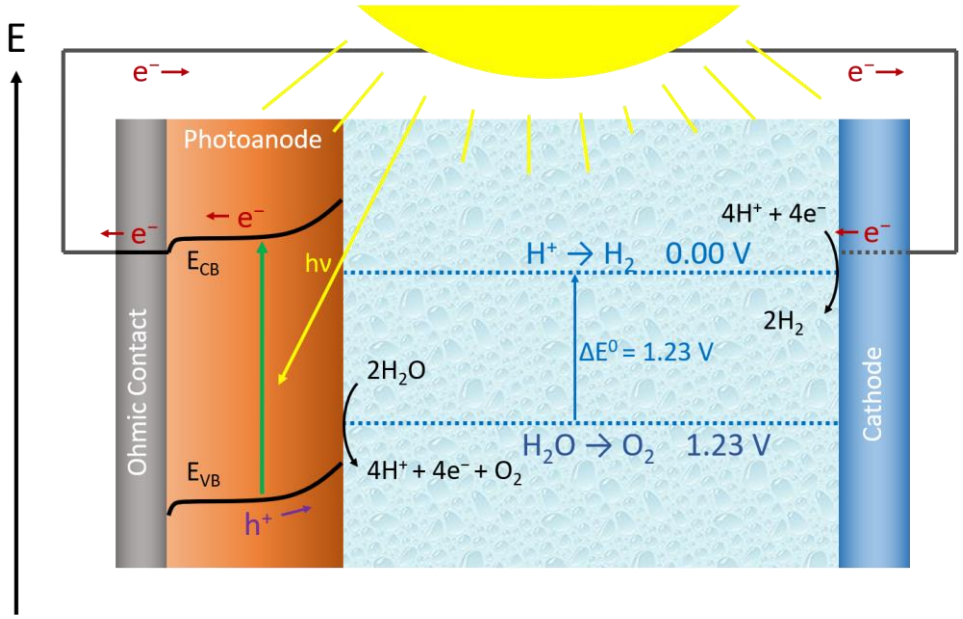

Figure 12. Working principle of PEC water splitting. Details in the main text.

In the context of this thesis, PEC is only used for water splitting, but large research communities also focus on photoelectrochemical CO_2 reduction[17,18] or PEC reduction of organic substrates[19] or biomass valorization.[20]

1.3 Dipoles on Semiconductors

The band positions of a semiconductor are classically defined by its electron affinity (E_{ea}), which, in solid state physics, is the distance between CB and the vacuum energy. On that basis, band diagrams of pn-junctions or semiconductor/electrolyte interfaces (such as in Figure 9 and Figure 11) are constructed using the electron affinity rule described by Anderson in 1960,[21] when also the Fermi levels (E_f) are known. The position of E_f within the band gap can be changed by doping as described above. E_{ea}, however, is strongly influenced by the surface properties. Surface impurities, moisture, dangling bonds etc. can all introduce a surface dipole which alters E_{ea} and therefore the built-in potential of PV

and PEC cells and in the end the performance of devices. Control over surface dipoles is a powerful tool to fabricate high efficiency PV and PEC cells.

Figure 13 shows three heterojunctions with different band alignment. In the first case (A), E_{cb} of the p-type side is much higher in energy than E_{cb} of the n-type partner and the same for E_{vb}. This is favorable in the sense that photogenerated electrons in the p-type can easily flow to the n-type, but not in the opposite direction. And in analogy, holes can flow to the back contact on the p-type side, but not to the front contact on the n-type. However, the energy difference between E_{cb} of n- and p-type side (ΔE_{cb}) is large and therefore the band bending and maximal photovoltage are small. The situation is different in (B). Here, E_{cb} of the p-type side is lower than E_{cb} of the n-type side. This leads to a barrier for electrons at the interface and limits the current. Small barriers might be acceptable if tunneling is possible, but larger barriers potentially shut down the current flow completely.

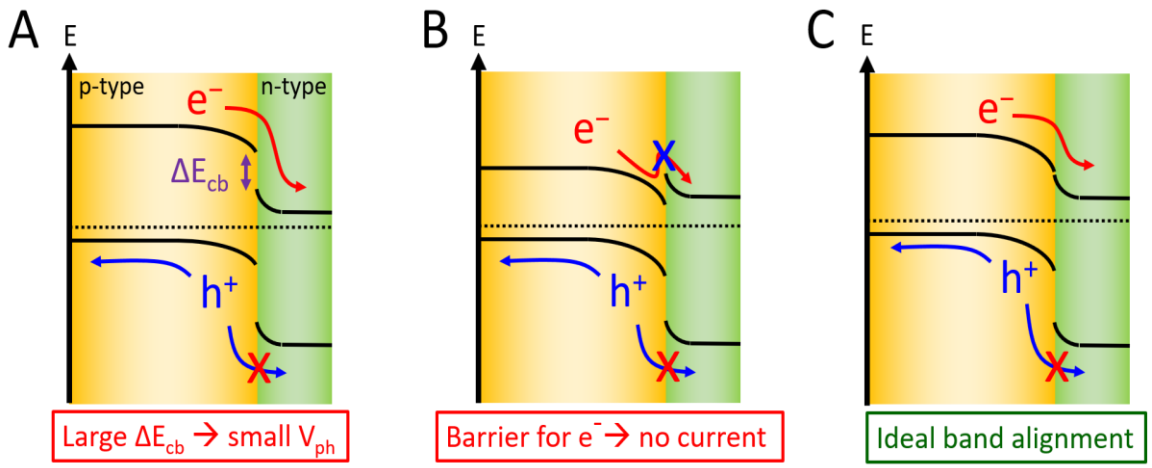

Figure 13. Illustration of different band alignments. A: ΔE_{cb} is large, which decreases the photovoltage that can be obtained. B: If the n-type side has a higher E_{cb} than the p-type side, a barrier for electrons will form upon contact and current flow is hindered. C: Ideal alignment, high photovoltage and unhindered electron flow.

Example (C) shows ideal band alignment. The band gap of the p-type partner is small, therefore absorbing most light, and most electron-hole pairs are generated on that side. ΔE_{cb} is minimal and the electrons can flow to the front contact unhindered, while holes are blocked from entering the n-type side. Furthermore, the small ΔE_{cb} yields a large photovoltage.

Band alignment optimization at heterojunctions for PEC and PV application is a key research area and numerous strategies have been reported in literature, some of which are briefly discussed here.

Fritsche et al. investigated the interface of CdTe/CdS heterojunctions in order to clarify the reason why a $CdCl_2$ activation step increases the performance of the devices. They found that the $CdCl_2$ activation leads to a graded CdTe/CdS junction instead of an abrupt interface with surface states. In the band

diagram, the grading is represented as a smooth band bending with a wide space charge region instead of a sharp step at the interface with a much narrower space charge region (Figure 14).[22]

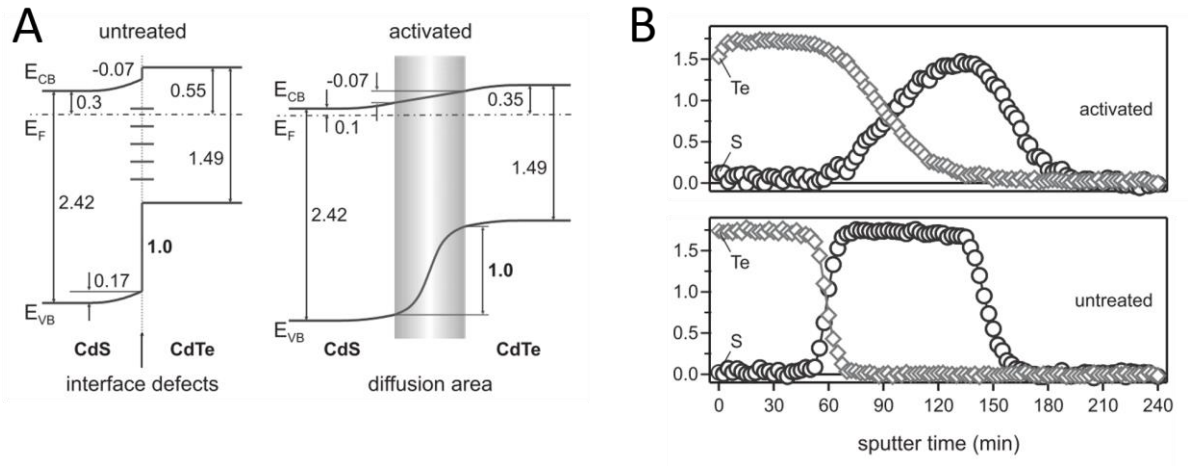

Figure 14 A: Band diagram of CdS/CdTe heterojunction PV cell without and with $CdCl_2$ activation. The untreated systems shows a sharp step at the interface, while the $CdCl_2$ activation leads to a graded interface and smooth band transitions. B: the difference between sharp and graded interface is clearly visible in XPS depth profiling experiments. Adapted with permission from ref [22].

The band structure of another example is presented in Figure 15A. Chuang et al. reported that J_{sc} as well as V_{oc} of quantum dot PV (QDPV) cells could be improved by the introduction of a layer of 1,2-ethanedithiol treated PbS QD on top of tetrabuthylammonium iodide treated PbS QD. In this case, the additional layer acts as an electron blocking layer and therefore reduces recombination at the front contact of the device.[23] A very different strategy was reported by Shaheen et al. (Figure 15B).[24] They tuned the work function of the acceptor material by doping it. This leads to a larger energy difference between the HOMO ($\approx E_{vb}$) of P3HT and the acceptor ZnO and therefore band bending is increased and a larger photovoltage is obtained (Figure 15B, bottom).

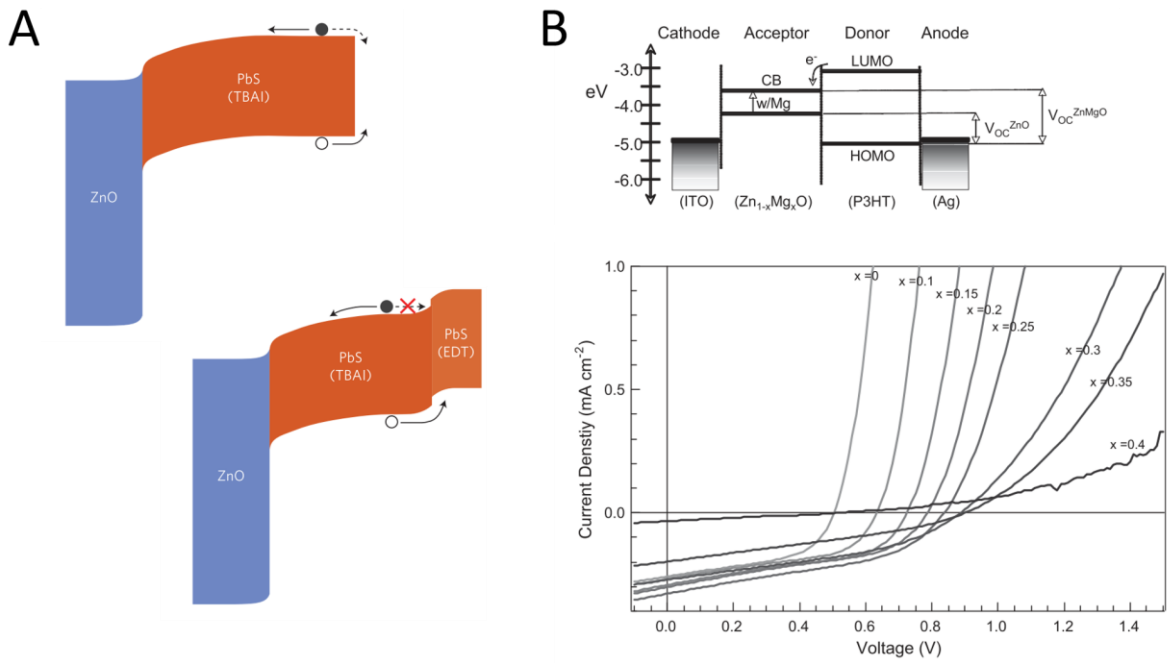

Figure 15. A: band structure in ZnO/PbS-TBAI (top) and ZnO/PbS-TBAI/PbS-EDT (bottom) devices at short-circuit conditions. The PbS-EDT layer prevents recombination of the charges. Figure adapted with permission from ref [23]. B: top: Band structure of a ZnO/P3HT heterojunction. The maximal photovoltage is the energy difference between the HOMO of P3HT and E_F of ZnO, which can be tuned by doping of the ZnO by Mg. Bottom: J-V plots showing the increased photovoltage with increasing Mg doping of ZnO. Figure adapted with permission from ref [24].

Siol et al. have studied defects at the interface of Cu_2O/ZnO devices and how the defects affect the band bending and ΔE_{cb} of the heterojunction.[25] Based on their results, they propose strategies to prevent defects and therefore decrease ΔE_{cb}, which potentially allows larger photovoltage.

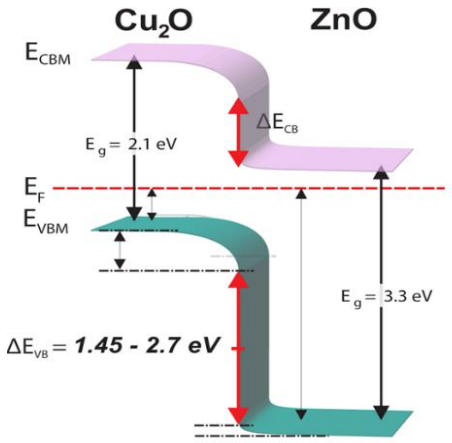

Figure 16. Band structure of Cu_2O/ZnO device. The influence of deposition methods on the band bending and ΔE_{cb} was studied. Reprinted with permission from ref 24.

Something all of the strategies presented above have in common is that they offer explanations and improvements for a very specific heterojunction. A more generally applicable method, and the topic of this thesis, is the usage of dipole layers to tune the band alignment of a heterojunction.

Extensive physical descriptions of the working principle of dipole layers can be found in some excellent reviews and textbooks.[26,27] The models described therein are often very mathematical and require the understanding of many advanced principles of materials science and solid state physics.

Here, a simpler derivation is presented, building up mainly on basics introduced in the previous subchapter as well as the concept of local vacuum energy level (E_{vac}). E_{vac} is a purely theoretical construct and describes the energy necessary to directly remove an electron from somewhere within a material into vacuum. In real systems, bulk electrons have to travel through the surface of a material in order to leave it and therefore they are affected by any kinds of dipoles on the surface of the material. The concept of E_{vac} is very useful when describing the effect of dipole surface modifications, because it allows to separate the electron affinity (E_{ea}) in the bulk of a material from the dipole induced effects on its surface.

A dipole sandwiched in between two materials has an electric field and therefore induces a step in E_{vac}, depending on the direction of the dipole (Figure 17). The electron density on the negative side of the dipole is increased and the bands are shifted upwards and vice versa. Figure 17 shows the different cases for a pn-homojunction. In Figure 17B, the dipole increases ΔE_f, but now E_{cb} is higher on the n-type side than on the p-type. Therefore, photoexcited electrons hit a barrier at the interface in analogy to the situation depicted in Figure 13B and current flow is diminished or completely blocked. A dipole in the other direction decreases the photovoltage obtained from the junction because it brings E_f of the junction partners close together (Figure 17C).

It is also obvious from the different cases shown in Figure 17 that a dipole layer is never beneficial for a homojunction. Therefore, all examples of successful applications of a dipole strategy in the literature and in this thesis only deal with heterojunctions.

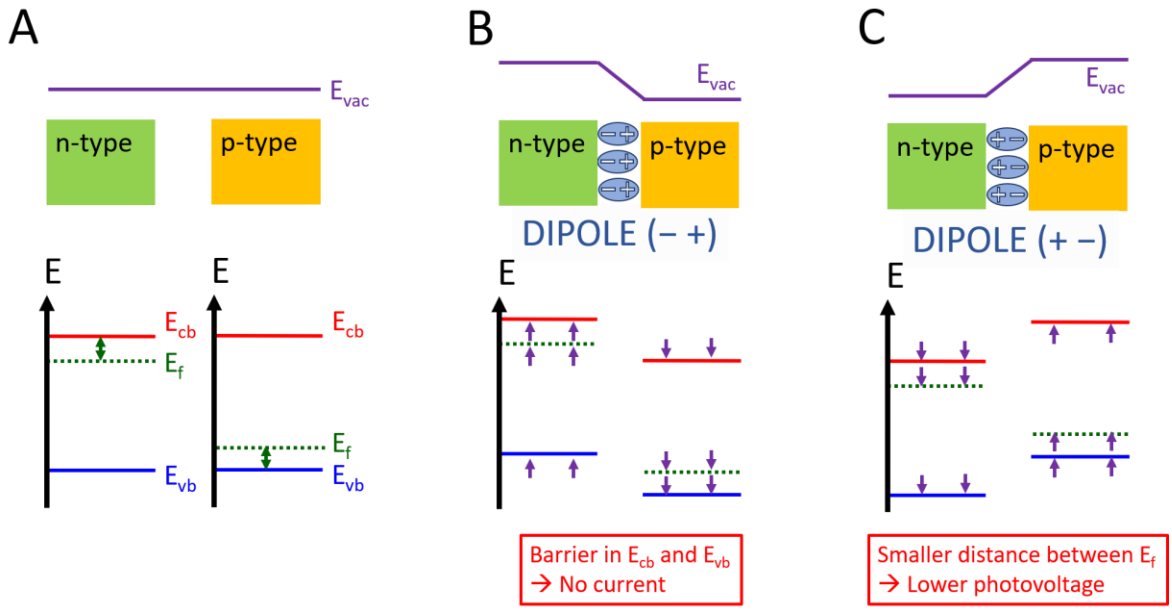

Figure 17. A: pn-homojunction band situation without dipole, and with dipole layer pointing in opposite directions (B, C). The dipole shifts the bands up on its (–) side and down on the (+) side.

In the vast majority of the literature, the dipole layer is a self-assembled monolayer (SAM) of an organic molecule where the molecule itself has an intrinsic dipole moment. The molecules are bound to the surface of a semiconductor substrate by a binding group, which is often a carboxylate[28,29] or phosphonate group[30,31] or thiol group for anchoring on Au substrates.[32–34]

We will now briefly discuss an illustrative example of how this method works on heterojunction solar cells (Figure 18).[35] The work was reported by Goh et al. and Figure 18A-C shows the band diagrams of a polymer/TiO_2 heterojunctions with and without a dipole layer pointing in different directions, in analogy to Figure 17. They used a library of substituted benzoic acids as dipoles, where the substituent in the para position determines the gas phase dipole moment of the molecule (Figure 18D). Electron withdrawing substituents lead to a dipole pointing away from the n-TiO_2, therefore decreasing electron density on the TiO_2 and shifting its bands down, relative to the p-type partner, the polymer layer. The effect can be observed in the J-V curves in Figure 18E. The devices with electron withdrawing dipole molecules have a smaller V_{oc}, because E_f of TiO_2 and polymer are brought closer by the dipole (Figure 18A).

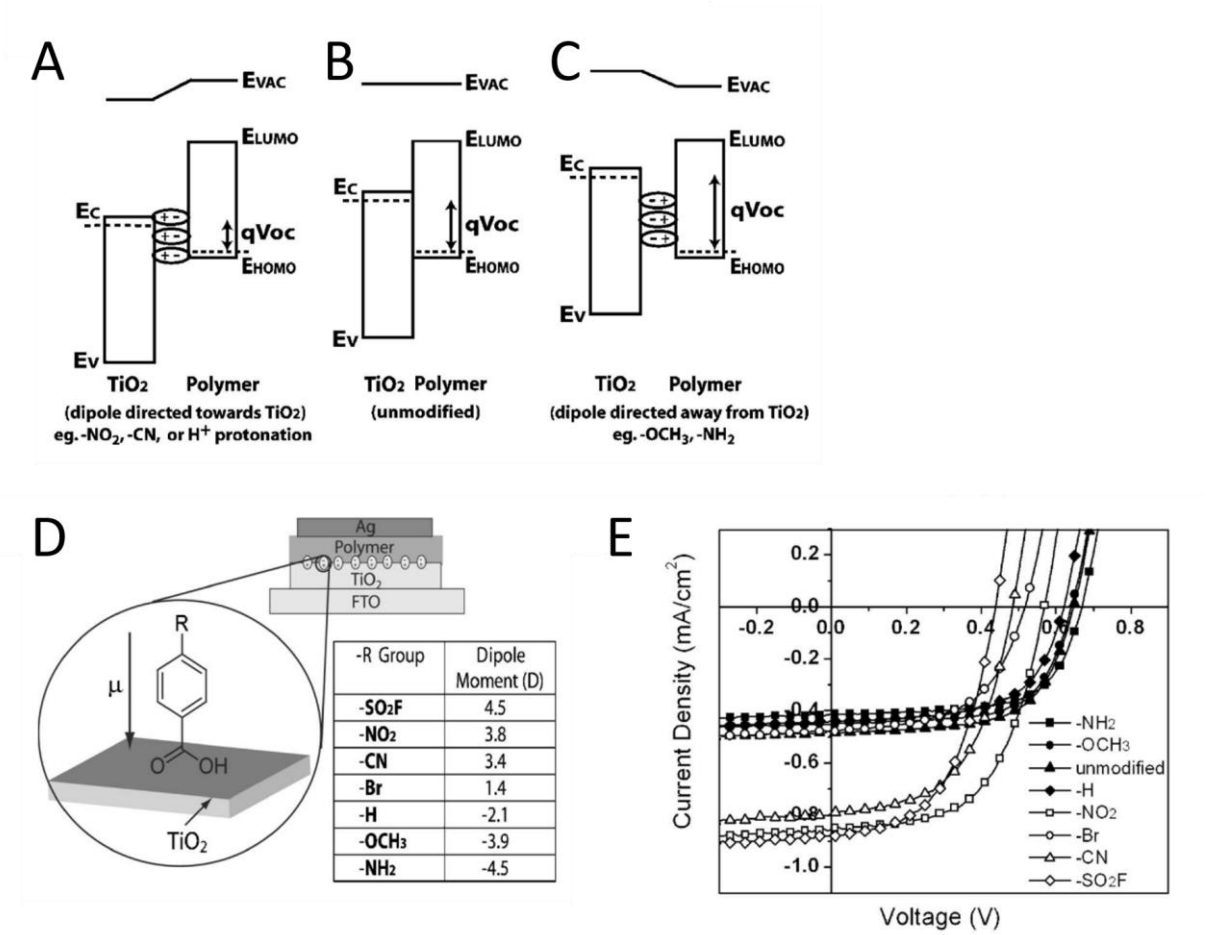

Figure 18. Band diagrams of n-TiO_2/p-polymer heterojunctions with a dipole pointing towards TiO_2 (A), without dipole (B), and a dipole pointing away from TiO_2 (C). D: The structure of the dipole molecules used in this study with a table of the calculated dipole moment for different substituent in para position. E: J-V curves of the PV devices with and without dipole layers. Adapted with permission from ref 34.

Similar studies have shown the successful application of the dipole layer strategy in organic PV,[36–38] perovskite PV[39,40] and quantum dot PV.[41–43]

In analogy to the heterojunction PV systems shown previously, the dipole strategy can also be employed in PEC. In the most simple case (a semiconductor in contact with an electrolyte) the dipole layer is grafted directly onto the semiconductor and is in contact with the electrolyte. Some proof-of-concept studies have shown that this strategy is possible, but those systems usually lack stability and the obtained V_{onset} shifts are small, since the electrolyte molecules can arrange themselves in a way that counteracts the desired dipole moment induces by the deposited dipole molecule.[44–47]

In the first part of the results in this thesis (chapter 2), such a simple system was investigated. Tungsten trioxide (WO_3), an n-type semiconductor with a band gap of 2.6 eV, was prepared using various synthetic methods and in a next step modified with phosphonic acid dipole layers. The band shifting effect of those dipole layers was then quantified by electrochemical impedance (more details on this

method in the experimental part) and by the photovoltage obtained under illumination. We found that WO_3 synthesis was more challenging than anticipated and the phosphonic acid induced band shifts were large, but not stable enough.

In the second part (chapter 3), we tried to overcome those limitations by using a well-studied, commercially available semiconductor as a model system and chose p-Si for this purpose. Si itself is not stable under operational PEC conditions (strongly acidic or basic electrolytes), and measures to protect the Si substrate as well as the dipole layer have to be taken.

One way to increase the stability of both photocathodes and photoanodes is the usage of a protection layer. For example TiO_2 deposited by atomic layer deposition (ALD) is widely used for this application.[48–51] Now, the photoabsorber is not in direct contact with the electrolyte anymore and also the photovoltage is not generated between photoabsorber and electrolyte, but between photoabsorber and protection layer. This is a so called buried junction PEC cell and can be viewed as a hybrid between PEC and PV.[52–54] The strategies developed to improve the photovoltage of buried junction PEC cells can therefore be applied for PV as well. TiO_2 has ideal band positions for hydrogen evolution with its E_{cb} just slightly more negative than the proton reduction potential (0 V_{RHE}). The band alignment of TiO_2 with most high performance photoabsorbers (such as Si, GaAs, CIGS, etc.) is very poor, which limits the photovoltage that can be obtained from p-Si/n-TiO_2 heterojunctions for example.[55,56] Dipole induced band shifting is therefore highly attractive also in the realm of buried junction PEC cells.

In a third part (chapter 4), we tried to generalize the dipole method by applying it to emerging thin film materials studied in our lab. We show successful examples (Cu_2O and Sb_2Se_3) and give explanations, why the method did not work in some other cases.

Conclusions are given along the way at the end of each chapter, and chapter 5 gives an overview over the work that is currently in progress and roughly sketches the direction of the project in the future.

2 Part 1: Phosphonic acid modification of WO_3

The first goal of this thesis was to demonstrate a dipole induced improved photovoltage for a model photoanode. We chose WO_3 as a model n-type semiconductor mainly for its stability in acidic electrolytes and ease of synthesis. An extensive review over the properties and applications of WO_3 was published by Zheng et al.[57]

The band gap of WO_3 is reported to be 2.6 eV, which is theoretically enough to enable full water splitting. For unassisted water splitting, roughly 1.8 eV are necessary (1.23 eV thermodynamic minimum + overpotentials for both half reactions).[58] However, as qualitatively depicted in Figure 19, the conduction band position of unmodified WO_3 is lower (more positive on RHE scale), than 0 V, the $H^+ \rightarrow H_2$ redox potential. Full water splitting is not possible, because the photoexcited electrons don't have enough potential to reduce protons to hydrogen. We therefore wanted to demonstrate a dipole induced band shifting that would ultimately allow full water splitting by WO_3. To reach this goal, firstly, reliable WO_3 synthesis methods have to be tested and secondly, suitable dipole modifications have to be found and thoroughly characterized.

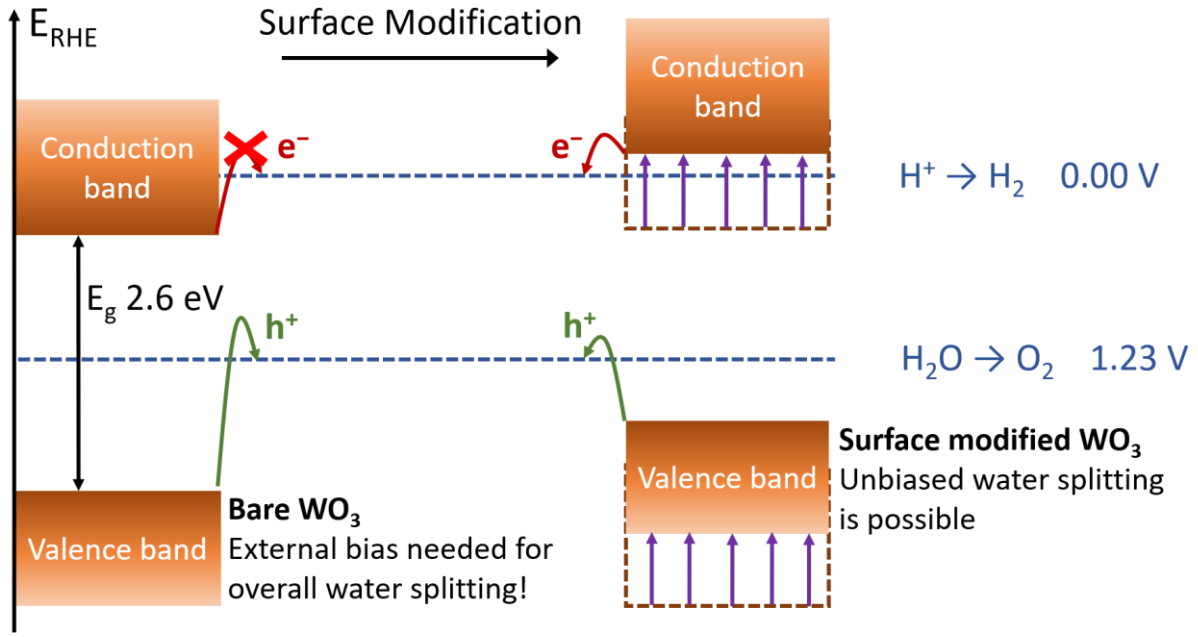

Figure 19. Qualitative band positions of WO_3. Left: E_{cb} of unmodified WO_3 is lower than hydrogen evolution potential. Unbiased water splitting is therefore not possible. Right: A surface modification induced band shift has moved E_{cb} high enough to allow unbiased water splitting.

2.1 WO_3 synthesis

2.1.1 Spin coating of WO_3

The spin coating technique is mostly used to fabricate WO_3 films for applications as electrochromic windows.[59,60] The procedures employed by Wang et al. and Deepa et al. and others included dissolving metallic tungsten in H_2O_2 (30 or 15%), followed by different procedures to decompose the excess of hydrogen peroxide. Spin coating of the obtained solutions onto FTO or ITO glass then gave amorphous WO_3, which was annealed at 150, 250 or 500 °C to give crystalline WO_3 with grain sizes depending on the annealing temperature.[59,60] The aforementioned research groups only tested their WO_3 films for electrochromic properties, but not for PEC applications. However, they seem to have obtained phase pure WO_3 using a very simple and potentially scalable technique, which is also an important prerequisite for PEC devices. In our approach, we also started by dissolving metallic tungsten in H_2O_2, but then used the most simple method to decompose the excess H_2O_2, namely by inserting a Pt mesh into the solution and heating it to 60-70 °C. The difficulty of this method is to find the right time to stop the heating, since WO_3 nano- or microparticles will start to precipitate after prolonged heating times when the H_2O_2 is fully decomposed. WO_3 particles in solution should be avoided because they will end up being spin coated onto the substrate, making the obtained films very inhomogeneous. The same effect was observed for films electrodeposited from old tungsten solutions (see chapter 2.1.4). After H_2O_2 decomposition, the aqueous solution was diluted with ethanol to improve the wetting properties of the solution, which is crucial for spin coating. Spin coating onto FTO glass and annealing at 500 °C gave pale yellow WO_3 films (Figure 20D). SEM imaging confirmed the presence of grains with diameters of 100 nm as reported by Deepa (Figure 20C).[60] Furthermore 1-2 µm wide cracks separate the WO_3 film into 100-1000 μm^2 islands (Figure 20A). These cracks are formed during the annealing step as the solvent (EtOH and H_2O) incorporated in the unannealed film evaporates leading to a substantial decrease of film thickness, inducing mechanical stress. Some WO_3 microparticles formed during H_2O_2 decomposition were also found incorporated into the film (Figure 20B).

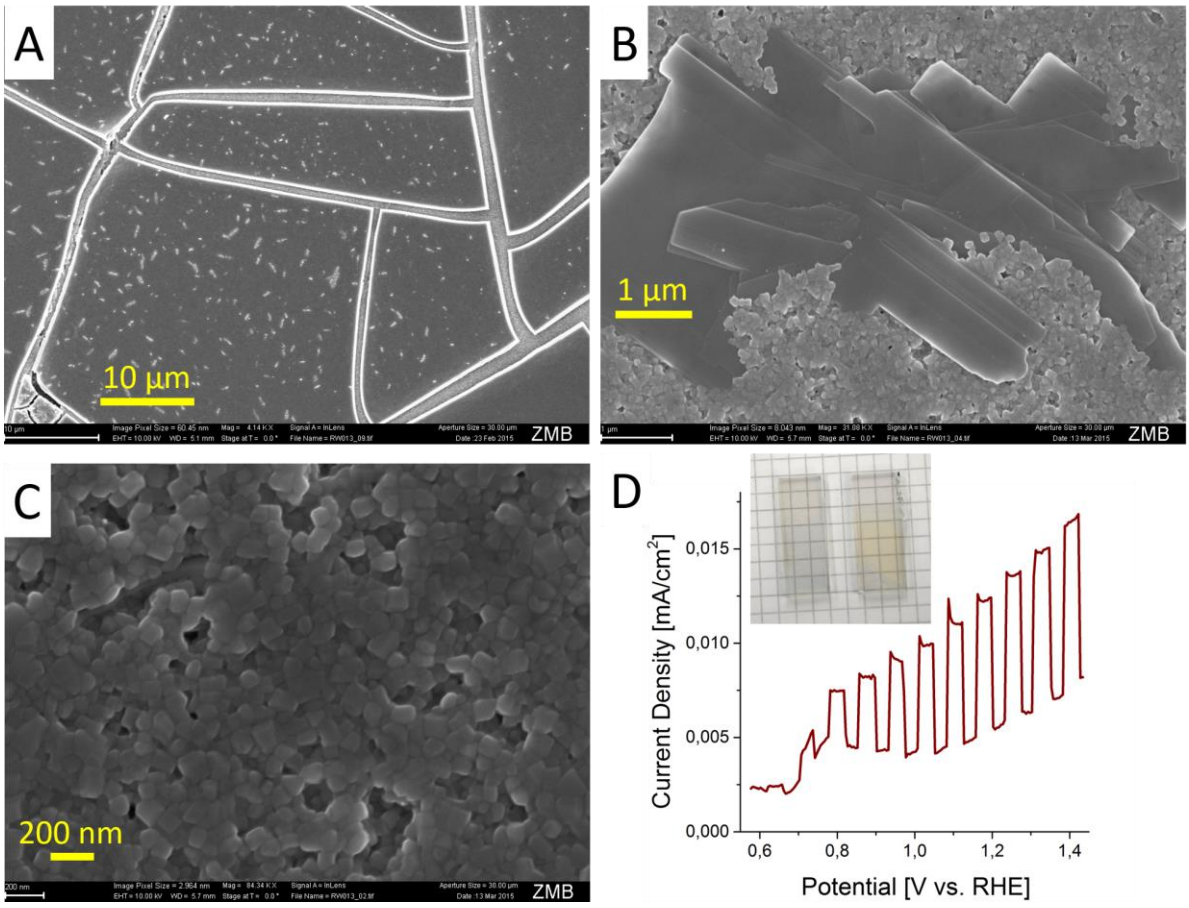

Figure 20. SEM images of spin coated WO_3 on FTO substrate at different magnifications. A: 4'000x; B: 34'000x; C: 85'000x. D: . J-V curve of spin coated WO_3 in 1M H_2SO_4 under chopped 1 sun illumination. Inset: Photography of spin coated samples.

The spin coated WO_3 samples were then tested for their photocatalytic activity in three electrode PEC measurements under chopped 1 sun illumination. Usually, the samples were illuminated from the front and the potential was swept from negative to positive, and it turned out that backside illumination did not substantially change the J-V behavior since charge transport (electrons as well as holes) seems not to be a limiting factor in these samples. A representative example of such a J-V curve is presented in Figure 20D. All samples showed very poor photocurrents of 1 – 20 µA/cm^2 and substantial dark currents in the same order of magnitude as the photocurrent. In summary, we were not able to obtain reasonable photocurrents (> 0.5 mA/cm^2) with this method and instead of optimizing all conditions (especially H_2O_2 decomposition, which seems to be of crucial importance) we went on to use different WO_3 synthesis techniques.

2.1.2 Doctorblading of WO_3

So called doctor blading technique is another fast and potentially very cheap thin film deposition technique. We used a very low-tech variant where the eponymous doctor blade is a simple glass rod, which is used to spread the precursor solution across the substrate in a linear motion. The film thickness is primarily defined by the thickness of the spacer used in the process. In our case, the tape used to fixate the substrate to the working surface served this purpose. Despite being very low-tech many research groups have successfully used doctor blading to fabricate some of the highest efficiency WO_3 devices in the literature. Especially the Augustynski group has used the technique for decades showing current densities of 3 mA/cm^2 at 1.23 V_{RHE} and energy conversion efficiencies of 0.8 %.[61]

We reproduced the procedure developed in Augustynski's lab.[62] Tungstic acid (H_2WO_4) was freshly prepared by running an aqueous Na_2WO_4 solution through a cation exchange column. The solution was then concentrated by evaporation of water and polyethyleneglycol (PEG) was added to stabilize the solution and increase the viscosity. This solution was then doctor bladed onto FTO glass slides, dried in ambient conditions and annealed at 500 °C. Figure 21 shows SEM images of a representative WO_3 sample prepared by doctor blading. All the images in Figure 21 were obtained from only one sample, showing that the WO_3 morphology is very irregular. A wide range of flake-like microstructures (Figure 21A), plates, rods and nanospheres are present in different spots of the sample, and different morphologies are often intertwined (Figure 21B). Control over the morphology was found to be not trivial and all attempts to optimize the conditions for preparation of the precursor solution, the doctor blading procedure and the annealing failed to reproducibly give the desired worm-like structures (Figure 21C,E).

The difficulties to obtain homogeneous WO_3 morphologies were also replicated in the device performance. For some samples the current density as well as onset potential and fill factor were quite promising (Figure 21F). However, the reproducibility issues were not resolved and the range of WO_3 morphology as well as PEC performance was not sufficient to use doctor blading for further studies.

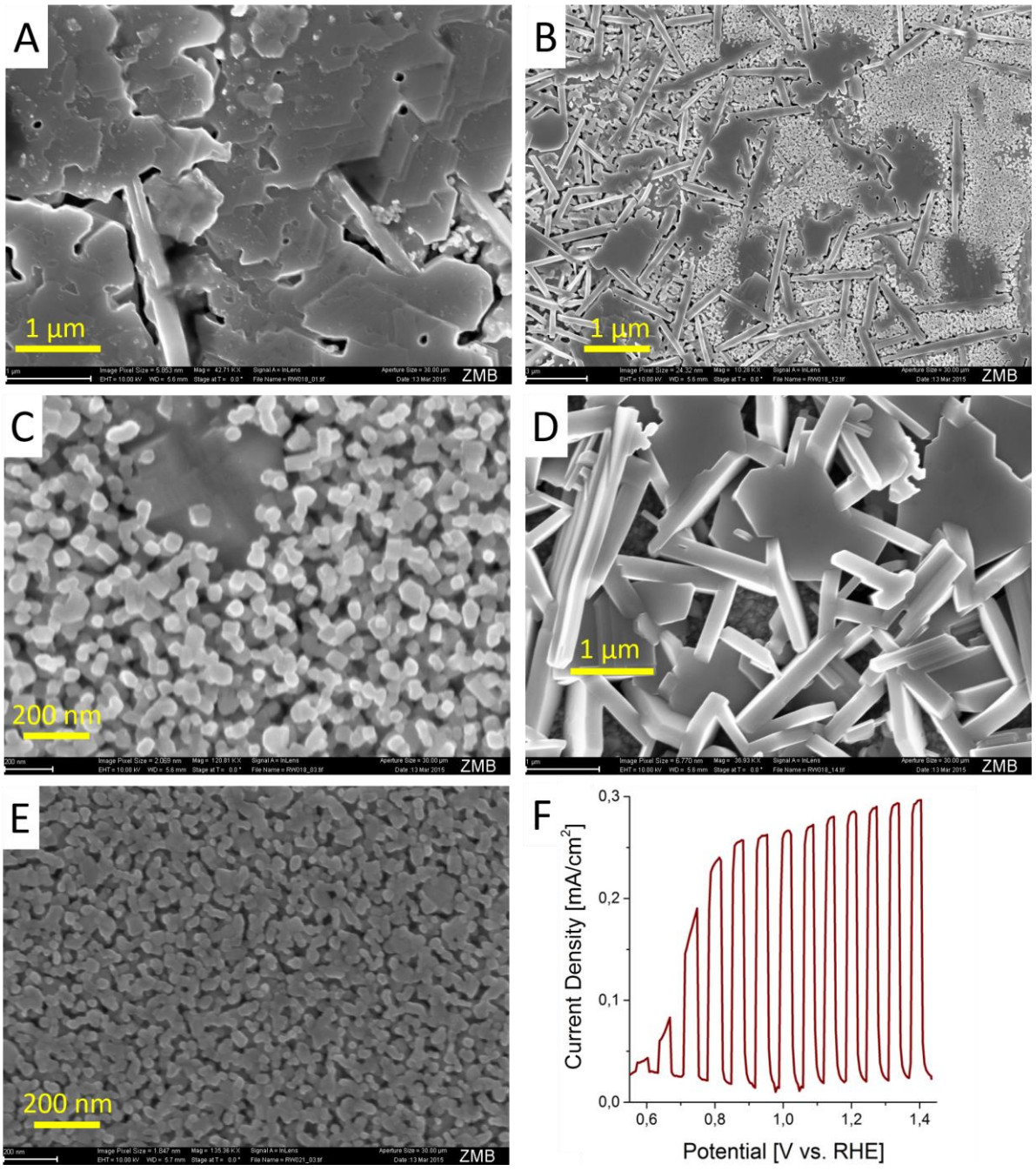

Figure 21. A-E: SEM images of WO_3 deposited on FTO by doctor blading showing the big variety of different morphologies obtained with this synthesis method. F: J-V curve of doctor bladed WO_3 in 1M H_2SO_4 under chopped 1 sun illumination.

2.1.3 Spray coating of WO_3

Hodes et al. reported in 1976 that spraying ammonium tungstate onto gold coated glass followed by annealing gave WO_3 films with current densities of 0.6 mA/cm^2.[63] Spraying or spray pyrolysis (if the substrate is heated to immediately decompose the precursor) is another low-tech method which can be scaled up to industrial scales. Instead of ammonium tungstate, we used a similar precursor solution as for the doctor blading experiments, namely tungstic acid in H_2O/EtOH (1:8), which was then sprayed onto a FTO coated glass substrate heated to 200 °C on a hot plate. After annealing, the samples showed a yellow coloration, with color intensities dependent on the volume of precursor solution sprayed onto the substrate (Figure 22C). The SEM images in Figure 22 show that the film is quite homogeneous on the nanoscale with tightly interconnected grains of 100 – 300 nm diameter (Figure 22B). However, the film is cluttered with cracks on the microscale (Figure 22A) and the adhesion of the WO_3 to the FTO substrate was poor.

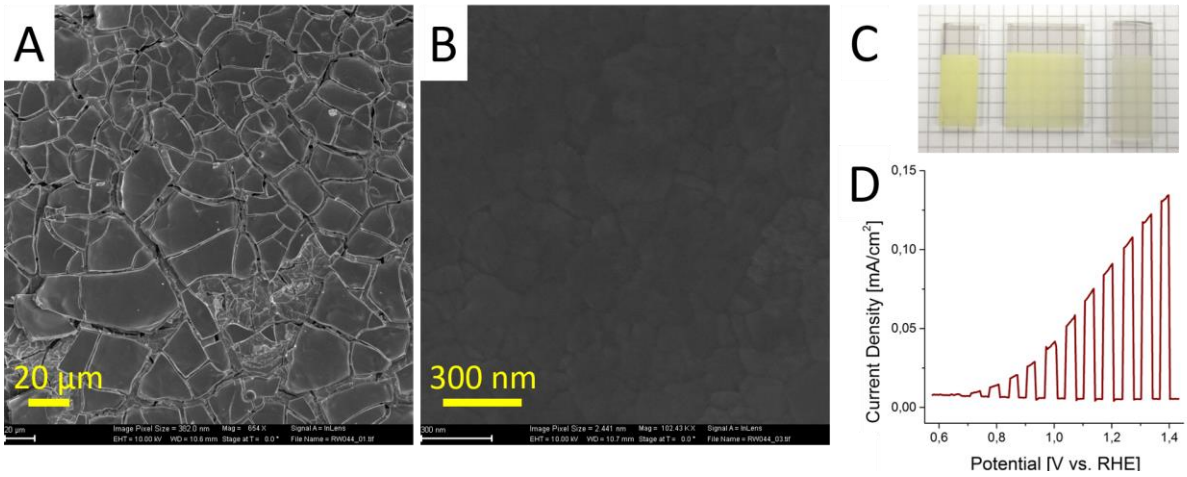

Figure 22. SEM images of spray coated WO_3 on FTO. A: magnification 654x, scale bar 20 µm; B: magnification 102'000x, scale bar 300 nm. C: Optical photograph of WO_3 film on FTO glass substrate fabricated by spraying (from left to right) 2, 1.5 and 1 ml of the precursor tungstic acid solution. D: J-V curve of WO_3 deposited by spraying and recorded in 1M H_2SO_4 under chopped 1 sun illumination.

We think the poor contact of the WO_3 to the back contact is also responsible for the poor PEC performance we measured for the sprayed samples (Figure 22D). The slow increase in photocurrent indicates a largely increased series resistance as compared to samples fabricated by doctor blading or electrodeposition. Current densities obtained at 1.23 V_{RHE} scaled with film thickness, which in turn was controlled by either the volume of precursor solution sprayed onto the substrate or the concentration of tungstic acid in the precursor solution. Nevertheless, the highest photocurrents obtained were on the order of 0.1 mA/cm^2 and were therefore outperformed by samples deposited by other methods.

Furthermore, the very basic tools we used for spraying make is almost impossible to reliably control the thickness and keep the sample variance low.

2.1.4 Electrodeposition of WO_3

The procedure we used to electrodeposit WO_3 was adapted from Lewis's research group.[64,65] Shaner et al.[65] as well as Mi et al.[64] have fabricated devices with photocurrents of approximately 1 mA/cm^2 at 1.23 V_{RHE}. The electrodeposition solution was prepared by dissolving metallic tungsten in H_2O_2 and then decomposing the excess of H_2O_2 by adding a platinum catalyst. After the O_2 gas formation had ceased, the yellow solution was diluted by adding isopropyl alcohol and water. Electrodeposition on FTO coated glass gave a deep blue WO_3 film with the blue coloring induced by intercalated protons. Thick WO_3 films (>2 µm) are desirable to absorb a high proportion of the light in PEC experiments, but we found that the deposition time and current had to be carefully optimized to avoid the formation of brittle films, where mechanical stress led to flaking off of the WO_3. Deposition current densities of -0.1 mA/cm^2 for 15 minutes, followed by a pre-annealing or drying at 275 °C yielded stable films. This cycle could be repeated 4 -5 times to obtain reasonably thick layers which were in the end annealed at 550 °C for 1 hour. A sample fabricated using this procedure is shown in Figure 23A, B. The top view image in Figure 23A reveals that the WO_3 is deposited quite homogeneously over large areas of the device but some cracks here and there could not be avoided. The typical thickness of those layers was approximately 1 µm (Figure 23B). The electrodeposition solution was stored in the fridge and used for a few days before WO_3 nanoparticles started to precipitate. If this aged solution was used for electrodeposition the nano- or microparticles were incorporated into the WO_3 film (Figure 23C, D), which gave opaque samples due to light scattering at the particles. Although samples fabrication was not very reproducible, we obtained some of the highest photocurrents with those samples, exceeding 1 mA/cm^2 at 1.23 V_{RHE} (Figure 24A). Despite the good performance, we only used flat WO_3 films obtained from fresh electrodeposition solutions due to better reproducibility and less complications associated with the increased, but unpredictable surface area of the "aged" samples. The flat WO_3 films usually gave 0.3 – 0.5 mA/cm^2 photocurrent at 1.23 V_{RHE} and a V_{onset} of 0.6 V_{RHE}. Mott-Schottky analysis performed on data obtained by EIS measurements in the dark revealed the n-type doping of WO_3 and a flat band potential of 0.43 V_{RHE} which is in good agreement with literature.[66–69] The cited references just calculated the capacitance at one frequency, while we performed a full fitting of the EIS data over a large frequency range of 1 MHz to 1 Hz (Figure 24B). This should make our M-S analysis and the obtained E_{fb} value more reliable. However, we kept getting extremely high doping densities on the order of $N_D = 10^{23}$. The reasons for this observation are unclear, we assume that intercalated protons or water contribute to the high donor density.

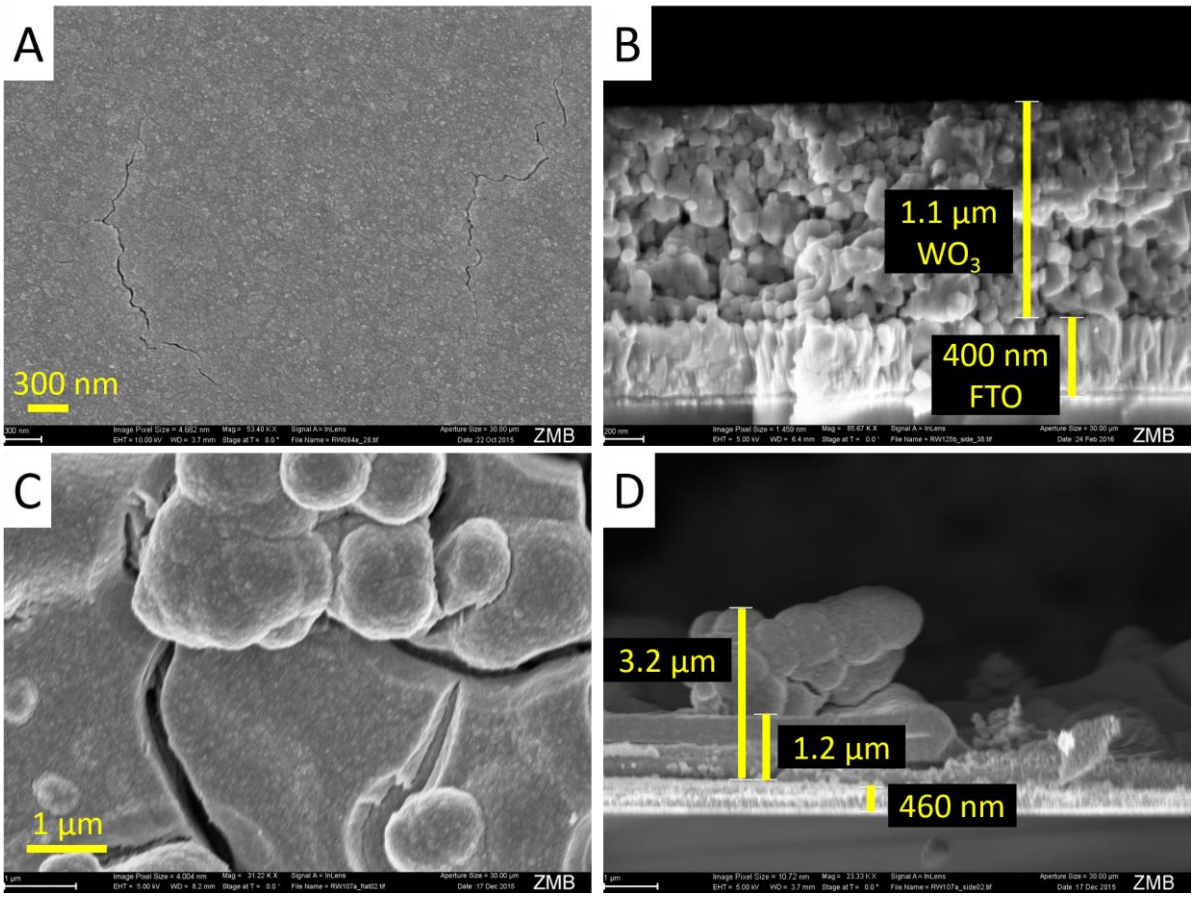

Figure 23. SEM images of electrodeposited WO_3. A,B: top- and sideview of very flat and homogeneous WO_3 with some cracks in the film. B. top layer: WO_3; bottom layer: FTO. C, D: WO_3 electrodeposited from old precursor solution showing µm sized spheres and high crack density.

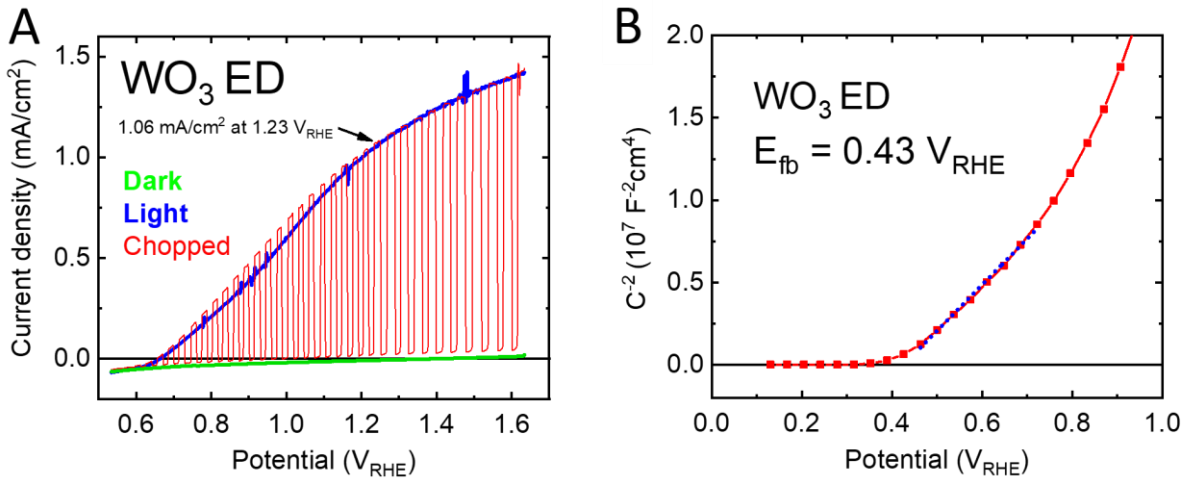

Figure 24. A: J-V curves of WO_3 electrodeposited (ED) from an aged precursor solution. Recorded in 1M H_2SO_4 in the dark, 1 sun illumination and chopped light. B: Mott-Schottky plot of WO_3 ED, measured in the dark in 1M H_2SO_4.

2.1.5 Overview

Figure 25 provides an overview over the four different WO_3 synthesis techniques we tested including representative SEM images and J-V curves as well as a list of advantages and disadvantages. To sum up, spin coating, doctor blading and spraying were all fast and easy but they yielded WO_3 with very poor to moderate photocurrents and had the critical disadvantage of not being reproducible enough. Only the electrodeposited samples performed reasonably well, while they were also reproducible. We therefore exclusively used electrodeposited samples for all further studies with phosphonic acids.

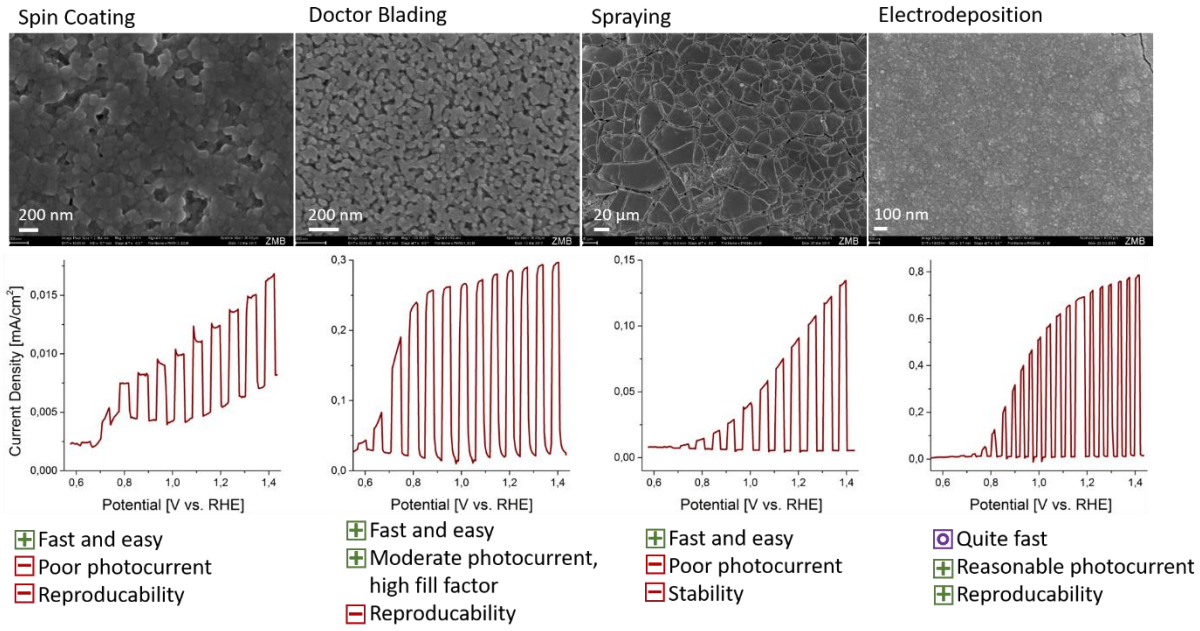

Figure 25. Overview over WO_3 synthesized with different methods.

2.2 Phosphonic acid modification

2.2.1 Why phosphonic acids?

Having a large enough quantity of decently performing WO_3 samples and a reproducible method to fabricate them, we investigated how the properties and especially the band positions of WO_3 can be influenced by surface modifications. Grafting of molecules to semiconductor surfaces typically makes use of an anchoring group that binds strongly to the substrate. For metal oxides, the most typical anchor groups are carboxylic acids and phosphonic acids. Those molecules are often grafted onto a surface by immersing the substrate into a solution of the target molecule for a few hours up to few days. This procedure was reported to yield self-assembled monolayers (SAM) in a reliable way for many anchor molecules and different substrates. For example, Rühle et al. grafted phosphonic acids and benzoic acids onto TiO_2 and fabricated dye-sensitized solar cells with different photovoltages depending on the dipole moment of the anchored molecule.[70] McNei et al. showed that the work function of ZnO can be changed by grafting phosphonic acids onto its surface.[71] We therefore decided to start our investigations by modifying WO_3 with a library of commercially available phosphonic acids, since they are reported to bind strongly and reliably to many metal oxides.

Please note that the abbreviation PA stands for the whole class of molecules bearing the $-PO_3H_2$ group as well as unsubstituted phosphonic acid (H_3PO_3). In this chapter, we are only dealing with substituted PAs, while in the next chapter unsubstituted PA (H_3PO_3) will be in the focus.

2.2.2 Substituted phosphonic acid deposition by T-BAG method

One method for phosphonic acid modification of metal oxides frequently reported in the literature is soaking of a substrate in a solution containing the PA. There is a large range for the conditions used but PA concentration is around 1 mM and soaking durations of 12 h are common. Depending on the solubility of the target PA, the solvent of choice is often water or ethanol.

To start with, we immersed electrodeposited WO_3 samples in aqueous 1 mM phenylphosphonic acid (PPA) and ethanolic 1 mM 4-pyridylphosphonic acid (PyPA, insoluble in water), sealed and shielded the vials from light. After 16 h, the samples were rinsed with water, dried and then used for electrochemical measurements. Figure 26A shows very similar J-V curves for blank WO_3 and WO_3 samples immersed in solutions of two different PAs. Most importantly, the onset potential of all three samples lies within 10 mV, and the small differences in current density are attributed to sample variance. Therefore, either the PA modification of the surface did not occur or the PAs are anchored

to the substrate but do not induce a band shift in the WO_3. As a third option, PA might induce a band shift that is not manifested as change in onset potential because the latter is limited by surface states.

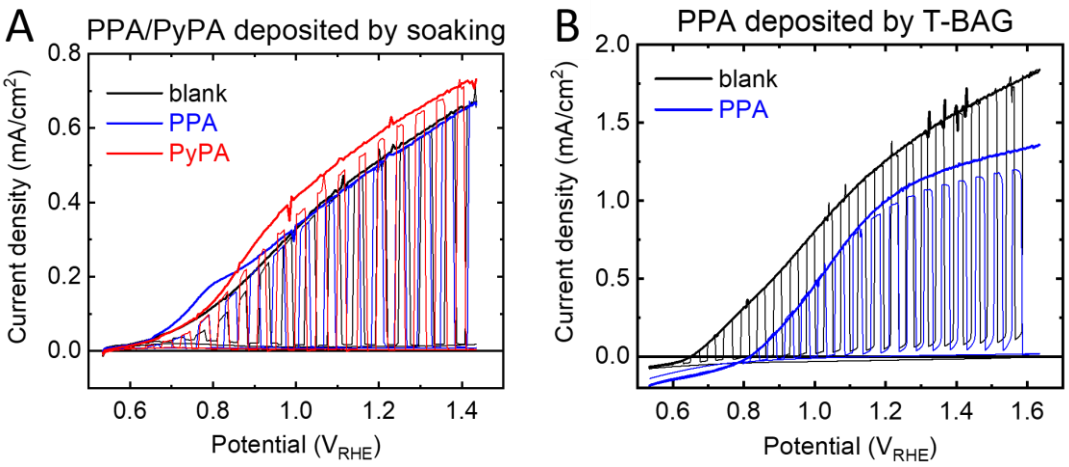

Figure 26. J-V plots of blank WO_3 (black) and WO_3/PPA (blue) and WO_3/PyPA (red). A: PPA and PyPA modification by soaking method; B: PPA modification by T-BAG method. All spectra recorded in 1 M H_2SO_4 under 1 sun illumination, chopped illumination and in the dark.

Before investigating the reason for the unchanged onset potential, we used a different PA deposition technique which was named "T-BAG" (tethering by aggregation and growth) by Hanson et al.[72] In this method, the substrate is placed vertically in an ethanolic solution of the target PA. The solvent is allowed to evaporate and the PA is transferred to the substrate surface as the solvent meniscus slowly traverses the sample. This process takes hours to days, strongly depending on the glassware used and the surrounding conditions (temperature, humidity). After the solvent is not in contact with the sample anymore, the samples are heated to 100 – 140 °C for up to 48 h to bind the physisorbed PA covalently to the metal oxide substrate. In our typical experiments, we used 10 mM phenylphosphonic acid (PPA) ethanolic solutions and solvent evaporation took approximately 24 h. Then, the samples were heated to 140 °C for 3 h. After that, a white residue was visible on the WO_3 substrate (crystalline PPA), which was washed off with water. The representative J-V curves in Figure 26B show that the onset potential of the modified WO_3 samples is clearly shifted to more positive potentials by 200 mV. This, together with the fact that the slope of the current after V_{onset} is the same for blank and PPA modified samples suggests that the PPA induced a band shifting in the WO_3.

This claim was further proven by Mott-Schottky analysis conducted with impedance data from the same blank and PPA modified WO_3 samples presented in Figure 26B. The Mott-Schottky plots in Figure 27 clearly show that the flat band (E_{fb}) of WO_3 is shifted to more positive values (by roughly 300 mV) upon PPA modification. It should be noted that we had to use different scale bars in Figure 27 since the capacitance of the WO_3 decreased drastically when it was modified with PPA which would indicate

that the doping density decreased. The reason for this is not clear, we hypothesize that surface states on WO_3 and their passivation by PPA play a role.

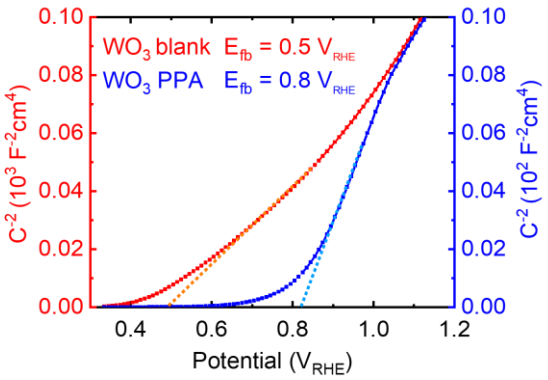

Figure 27. Mott-Schottky plot of blank WO_3 (red) and PPA modified WO_3 (blue). Data extracted from impedance measurements in 1 M H_2SO_4 in the dark at 1 Hz.

Up to now, we successfully showed that the bands of WO_3 can be shifted by depositing a layer of PPA. Later results (See Part 2: p-Si/PA/TiO_2) suggest that the PPA layer is indeed thicker than a monolayer, but this possibility was not considered at the time of the PPA on WO_3 experiments, since phosphonic acid multilayers were never reported in literature to the best of our knowledge. Although the magnitude of the band shift was encouraging and a valuable proof of principle (phosphonic acid induced band shifting has been shown in literature on TiO_2, but never on WO_3), the bands (and therefore the onset potential) of WO_3 are shifted in the "wrong" direction. The PPA layer moves the bands to more positive potentials and decreases the energy difference between WO_3 fermi level and H_2O/O_2 redox potential of the solution (+1.23 V_{RHE}) and results in a smaller photovoltage as compared to the unmodified WO_3. The dipole moment of PPA was calculated to be +1.4 D (Figure 28), pointing towards the surface of the substrate. For a dipole in this direction, we expected that the PPA would increase the energy of the substrate bands and therefore shift them to more negative potentials on the RHE scale (or more positive on vacuum energy scale). However, what we observed was a large band shift in the opposite direction upon PPA modification. The reason for this behavior was also discovered much later and is described in detail in chapter 3.4. In brief, the band shift is not primarily determined by the gas phase dipole of the phosphonic acid used, but arises from the fact that highly electron donating OH groups on the surface of a metal oxide are replaced by less donating phosphonate groups. This decreases the electron density in the semiconductor and therefore shifts the bands to more positive values (on RHE scale).

Similar studies on TiO_2 suggest that the band shift can be tuned by using phosphonic acids with different gas phase dipole moments.[47] In a next step, we wanted to test a library of different

phosphonic acids with very different substituents including methyl-, aminomethyl-, phenyl- and benzyl-groups (Figure 28) and a selection of benzylphosphonic acids with different substituents at the para position of the benzyl ring (Figure 29). All of those phosphonic acids are commercially available and our collaborator Dr. Tiziana Musso calculated their gas phase dipole moments along the P-C bond (Z-direction). The selection covers a large range of dipole moments from very negative to very positive.

Name	Structure	DFT structure	Dipole direction	Dipole along Z direction
Phenyl-phosphonic acid **PPA**	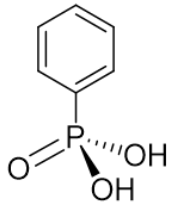	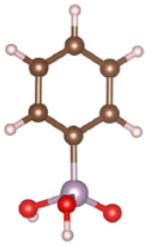		+1.4 D
Methyl-phosphonic acid **MPA**	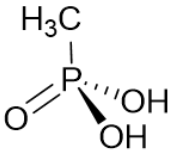	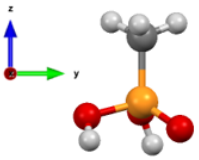		+0.6 D
Aminomethyl-phosphonic acid **AMPA**	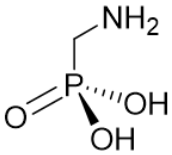	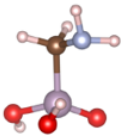		+3.9 D
Benzyl-phosphonic acid **BPA**	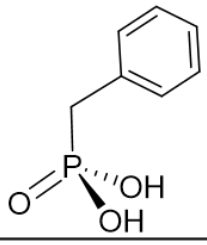	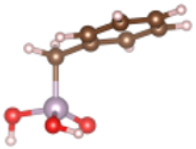		+0.7 D

Figure 28: Comparison of different phosphonic acids used to modify WO_3 substrates. Structures and dipole moment along z-direction calculated by T. Musso.

Name	Structure	DFT structure	Dipole direction	Dipole along Z direction
Benzyl-phosphonic acid **BPA**	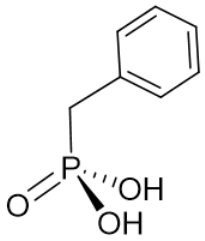	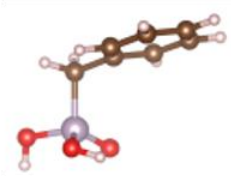		+0.7 D
Fluorobenzyl-phosphonic acid **FBPA**	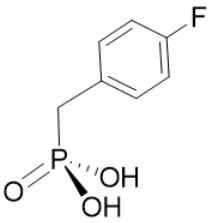	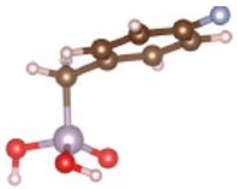		+0.0 D
Bromobenzyl-phosphonic acid **BBPA**	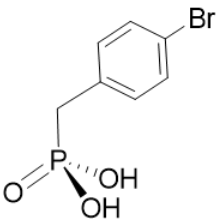	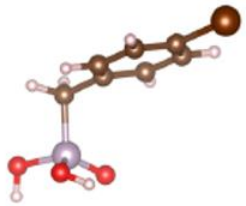		-0.1 D
Nitrobenzyl-phosphonic acid **NBPA**	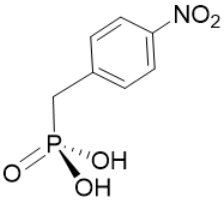	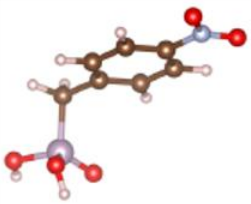		-1.7 D
Hydroxybenzyl-phosphonic acid **HBPA**	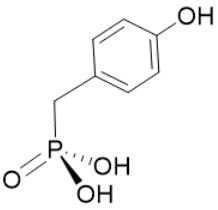			+4.8 D

Figure 29: Comparison of different phosphonic acids used to modify WO_3 substrates. Structures and dipole moment along z-direction calculated by T. Musso.

Electrodeposited WO_3 substrates were modified with the different phosphonic acids using the T-BAG method and the flat band energies obtained from Mott-Schottky analysis are summarized in Figure 30. The results of the flat band measurements nicely confirm our hypothesis. All phosphonic acid modifications lead to a positive E_{fb} shift, even if the gas phase dipole moment of the phosphonic acid derivative is very positive. This is in agreement with our expectations, because in all cases, we replaced OH groups on the WO_3 surface with less electron donating phosphonate groups. Even in the case of a

very positive gas phase dipole moment (e.g. AMPA), once bound to the surface, the AMPA molecule is still less electron donating than OH and shifts the bands down. But still, we also observe differences in the magnitude of the E_{fb} shift and a linear correlation with the dipole moment. The E_{fb} shift is shown in Figure 30 and corresponds to -29 mV/D. In a similar study, where Rühle et al. absorbed different phosphonic acids and carboxylic acids on TiO_2 and measured the V_{oc} of dye sensitized solar cells fabricated from the modified TiO_2, they found a dipole dependent shift of 6-9 mV/D, but with lower surface coverage of the dipole molecules.[70] Furthermore, they also observed that all of the modified samples showed a lower V_{oc} than the blank samples, which makes us believe that they found the same effect (replacing electron donating OH groups on the metal oxide), without explicitly naming it.

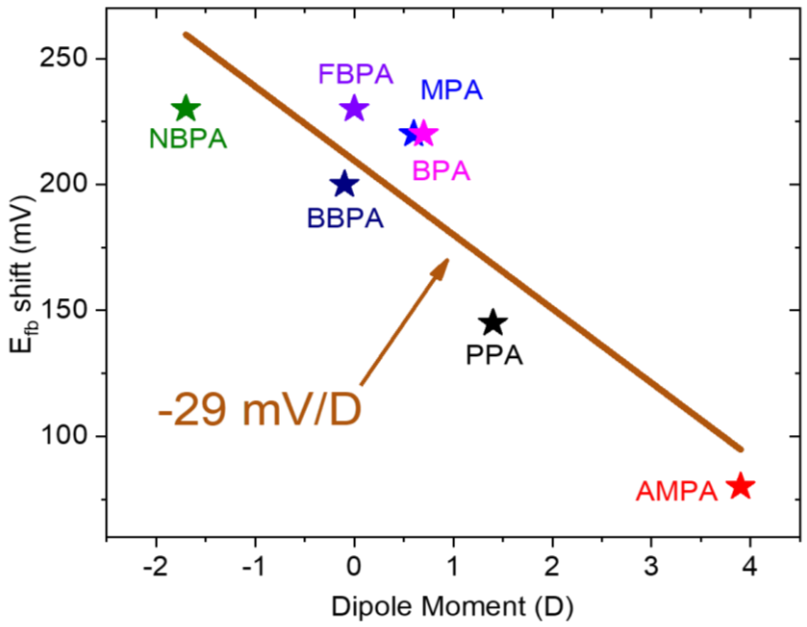

Figure 30: Molecular dipole moment versus E_{fb} shift with linear fit. E_{fb} values obtained from Mott-Schottky analysis.

Characterization of the phosphonic acid layer was a major challenge due to the very low concentration of the analyte. In some reports, authors have observed the P=O stretching frequencies in FT-IR, even for a monolayer of octadecylphosphonic acid on a flat TiO_2 surface.[72] We were not able to reproduce those results for our phosphonic acids on WO_3 and therefore made use of 4-nitrobenzylphosphonic acid (NBPA), bearing the strong NO_2 IR tag, for IR measurements. Figure 31A shows the strong and characteristic N-O stretching vibrations at 1517 cm^{-1} (asymmetrical) and 1342 cm^{-1} (symmetrical, black trace), while the characteristic peaks of blank WO_3 are at 1038, 798 and 720 cm^{-1} (blue trace). NBPA was then drop casted onto WO_3 and annealed at 140 °C. This procedure results in a very thick NBPA film, visible as an opaque crust, on WO_3. The IR spectrum of this sample clearly shows all the WO_3 as well as the NBPA powder peaks (red trace). After rinsing with water, the NBPA layer is not visible anymore and also in IR only the strongest N-O peaks are observed. Furthermore, after one impedance

measurement (where the sample was immersed in 1 M H_2SO_4 for a total of 1 hour in the dark) the N-O intensity decreased by roughly 50% and vanished almost completely after a chronoamperometric measurement at 1.6 V_{RHE} under illumination for 5 minutes. Those findings led us to the issues that were investigated next, phosphonic acid stability on WO_3 in the dark and under illumination.

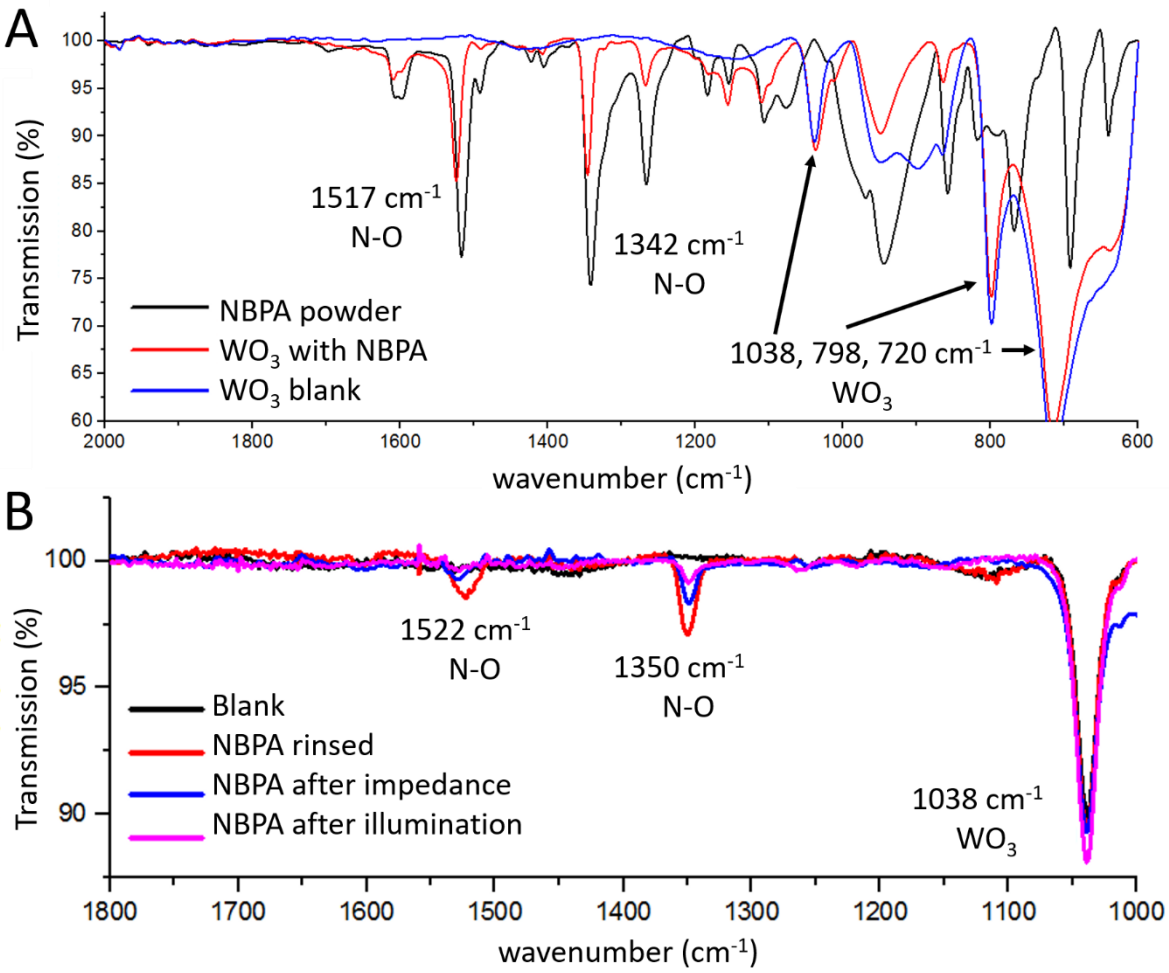

Figure 31: FT-IR measurements. NBPA (A, black) was measured as a powder, while all other measurements used WO_3 on FTO as substrate. For A, no reference was used ("air"), while measurements in B are referenced to FTO on glass.

2.2.3 Stability

We assessed the stability of a BPA layer on WO_3 by subsequent impedance measurements. As depicted in Figure 32, E_{fb} of this sample shifted from +0.40 V_{RHE} to +0.62 V_{RHE} upon modification with BPA. After another measurement (each one took 15 minutes) E_{fb} was shifted back to +0.57 V_{RHE}. After ten impedance measurements in total, the E_{fb} was +0.48 V_{RHE} and therefore 70% of the initial E_{fb} was lost after a total measuring time of 2.5 hours. However, towards the end, E_{fb} seemed to stabilize at a value of 0.48 V_{RHE} , which corresponds to a band shift of +80 mV as compared to the blank sample. We

concluded that large, stable band shifts cannot be obtained with unprotected phosphonic acids in contact with strongly acidic electrolyte.

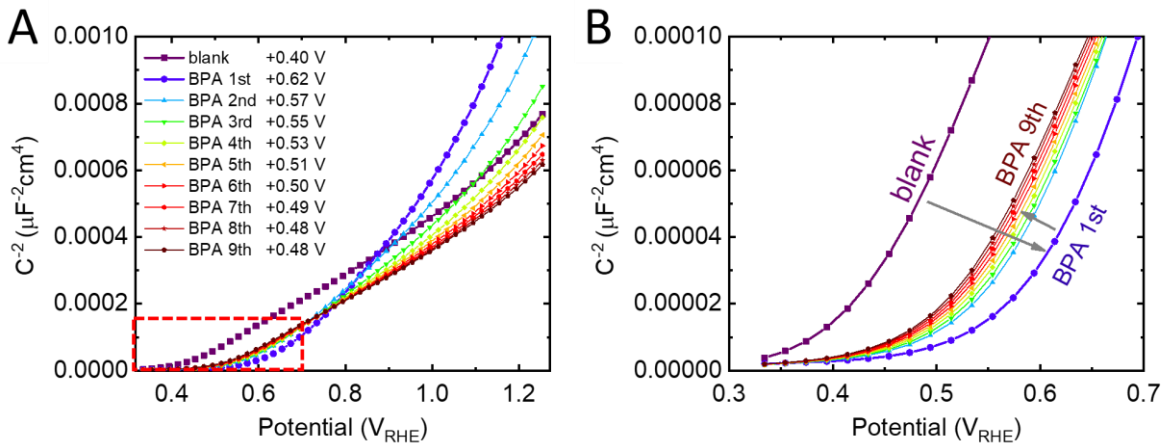

Figure 32. A: Mott-Schottky plots of blank WO_3 and 9 subsequent measurements of WO_3 modified with BPA. Data obtained from impedance measurements at 1 Hz in 1 M H_2SO_4. B: zoom-in of the region in the red rectangle in A.

When we measured chronoamperometry of freshly modified samples, we noticed that all samples showed an increased current when the illumination was turned on for the first time (Figure 33A, light blue area). In subsequent CA measurements this transient current was not observed (Figure 33A, red trace). We attributed the increased current to an oxidation of the BPA or other phosphonic acids, which showed the same behavior. TiO_2 is very well known to degrade organic molecules on its surface under illumination due to the very high energy of photogenerated holes. TiO_2 has its valence band at approximately +3 V_{RHE} and this value should be similar for WO_3. We know the band gap of WO_3 to be 2.6 eV and measured E_{fb} (or the fermi level energy) to be +0.4 V_{RHE}. From the very high doping density assumed for WO_3, we estimate the conduction band to be around +0.3 V_{RHE}, which would place its valence band at +2.9 V_{RHE}. Therefore, we conclude that degradation of organic molecules on WO_3 should be similarly feasible than on TiO_2. The transient photocurrent observed in Figure 33A integrates to 0.4 mC, which corresponds to the oxidation of 2 nmol BPA. On our active area of 0.283 cm^2, 2 nmol BPA is roughly 40 molecules per nm^2, a number that clearly indicates that we were dealing with BPA multilayers. Together with the intrinsic instability of the phosphonate anchor layer (Figure 32), the

photooxidation of BPA is another hint that protection of the phosphonic acid layers is crucial to obtain stable anchoring and large band shifts.

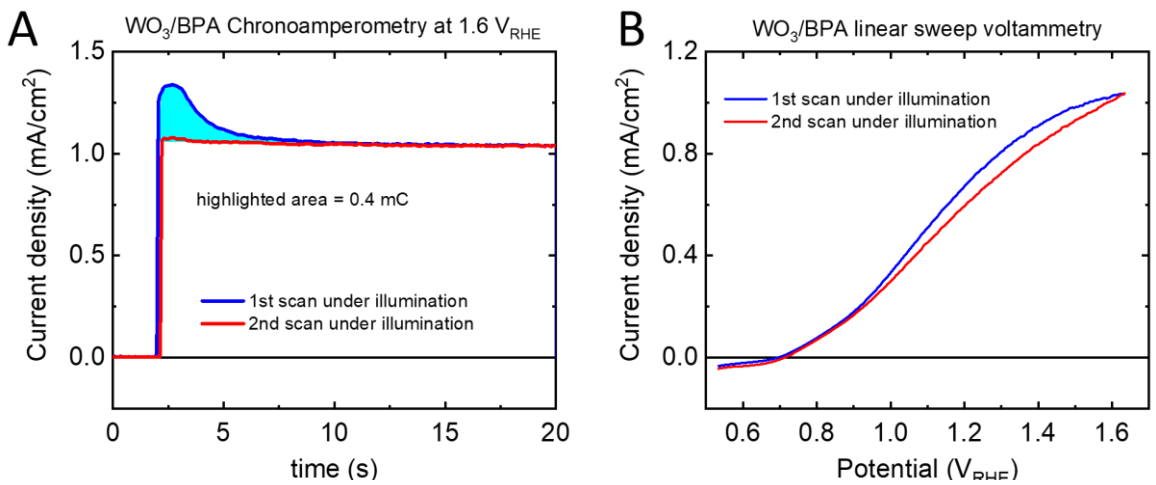

Figure 33. A: CA measurement at 1.6 V_{RHE}. The first scan shows an increased photocurrent when the illumination is turned on (light blue area).

2.3 Conclusions

In this first part, we traced our effort on making WO_3 films and modifying them with phosphonic acids to shift the WO_3 bands. WO_3 was chosen as a model substrate due to its stability and simplicity of fabrication. In fact, many different synthesis methods were reported in literature and we tried to reproduce some of them. The spin coating, doctor blading and spray pyrolysis methods were very straightforward, but gave very low performance WO_3 samples (with some exceptions, but the samples with reasonable performance could not be reproduced). Finally, we were able to synthesize WO_3 with acceptable performance (1 mA/cm^2) and reproducibility by electrodeposition and annealing. The morphology of the samples was characterized by SEM, and electrochemical measurements in 1 M H_2SO_4 in the dark and illumination were performed to obtain the onset potential (and therefore the photovoltage) and the photocurrent. Electrochemical impedance and Mott-Schottky analysis revealed the position of the fermi level under flat band condition, which matched well with the onset potential.

In a next step, the conditions for anchoring of different phosphonic acids onto WO_3 substrates were optimized and the T-BAG method showed promising results as E_{fb} of the PPA modified WO_3 samples was increased by 300 mV as compared to blank WO_3. Screening of ten different phosphonic acids with very different dipole moments revealed that all modifications led to a positive shift in E_{fb}. This contradicted our expectations of a positive shift with positive dipoles (dipole pointing towards the WO_3) and a negative shift with negative dipoles (dipole pointing away from WO_3). We therefore

hypothesize that the main contribution leading to a band shift is the replacement of electron donating OH groups on the WO_3 by less electron donating phosphonate groups. We showed that the dipole moment of the phosphonic acids only plays a minor role and influences the magnitude of the band shift, but not the direction of the shift.

The experiments up to this point served as a proof of concept that band shifting of WO_3 by phosphonic acids is possible, but also revealed some major drawbacks, which were then addressed in the next section. Firstly, all the band shifts were in the positive direction, which is unfavorable for photoanodes, as it decreases the photovoltage. However, for photocathodes, the positive shifts we obtained (up to +250 mV) are very attractive, so we tried to modify p-type semiconductors next. Secondly, the fabrication of WO_3 was not as simple as expected, another reason to abandon WO_3 and use other substrates (p-type) instead. Thirdly, our experiments indicate that the phosphonic acids are not stable in direct contact with the electrolyte. The usage of protection layers to circumvent this issue was tested in the next chapter.

3 Part 2: p-Si/PA/TiO_2

In this chapter we trace our efforts to overcome the limitations of our work on WO_3 modified with phosphonic acids. Most importantly, we exchanged our n-type model substrate WO_3 with p-type silicon. The silicon was purchased as a high quality wafer, allowing us to focus solely on modification of the substrate, rather than its fabrication, which was more time consuming than expected in the case of WO_3. A p-type material was chosen, since up to now, all the surface modifications have led to a positive band shift, which is unfavorable for n-type semiconductors, but desirable for p-type materials. Furthermore, the flatness of Si wafers allowed additional characterization methods such as ellipsometry, which proved very helpful as a fast and easy tool to measure the thickness of anchor-, protection- or dipole layers on the substrate. The implementation of protective layers was another important issue in order to increase the longevity of the dipole induced band shifts.

Parts of this chapter were published in *Energy & Environmental Science* and some figures herein were reprinted or adapted from that publication.[73]

3.1 PA on TiO_2

As already mentioned in the WO_3 chapter, the dipole in our system arises from the replacement of OH groups by phosphonate groups on the surface of the substrate material. In the long term, we want to be able to apply our method to different substrates with as few changes as necessary. To achieve this, we made use of an anchor layer on top of the substrate. This very thin layer would then assure that the binding of the phosphonic acid to the anchor layer is always the same since it is not directly bound to the photoabsorbing substrate. We chose TiO_2 fabricated from ALD as a starting point for our investigations since ALD allows the deposition of thin, homogeneous layers with controllable thickness.

The anchoring of different phosphonic acids onto TiO_2 was tested on a thick ALD-TiO_2 layer without photoabsorbing substrate to facilitate the impedance analysis. Some results on WO_3 suggested that spin coating of phosphonic acid could be used to modify the substrates instead of the T-BAG method. Spin coating was much faster and gave similar band shifting. PPA, NBPA and PA were spin coated as ethanolic solutions onto TiO_2 and then annealed at 120 °C before rinsing with ethanol. Surprisingly, the Mott-Schottky plots of the modified samples revealed very small shifts of only 50 mV for PPA and NBPA, but 300 mV for the PA modified sample (Figure 34A), the biggest E_{fb} shift observed so far. Other samples were modified with PA and then protected with 1 or 5 nm of ALD-TiO_2. The E_{fb} of the sample with 1 nm TiO_2 protection was even more positive, probably, because in the unprotected case, some

of the PA is already lost during the measurement (compare Figure 32). However, if the protection layer was thick (5 nm or thicker), the protection layer TiO_2 is thick enough to develop its own band bending and therefore flat band behavior. The blue trace in Figure 34B shows two clear regions. At positive potentials the capacitance of the substrate TiO_2 layer is probed, with a E_{fb} of +0.22 V_{RHE}, while at potentials around 0 V_{RHE} the protection layer TiO_2 is probed, which is on the same side of the dipole layer as the reference electrode and shows an E_{fb} close to unmodified TiO_2. This is an illustrative example to explain how two capacitances in series are summed up according to:

$$\frac{1}{C_{tot}} = \frac{1}{C_1} + \frac{1}{C_2}$$

It is obvious from this equation that the smaller of the two capacitances in series will dominate the overall capacitance and that is exactly what we observe in the sample with two TiO_2 layers (Figure 34B). At potentials around +0.4 V_{RHE} the C of the PA modified sample (red trace) is lower than C of the blank (black trace). Therefore, if a shifted and an unshifted TiO_2 layer are present in one sample (blue trace), the C at +0.4 V_{RHE} is dominated by the layer with lower C, namely the shifted substrate TiO_2 and vice versa at lower potentials <0.2 V_{RHE} where C of the protection TiO_2 is lower and mainly dictates the overall C.

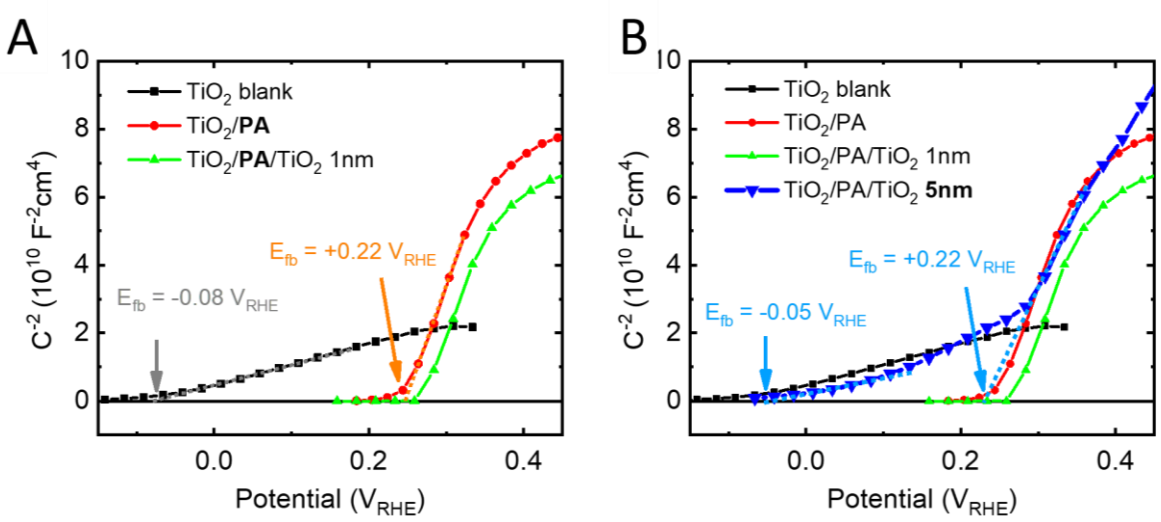

Figure 34. A: Mott-Schottky plots of samples with 100 nm of TiO_2 on ITO substrate. The dotted lines represent a linear fit, pointing to E_{fb} when extrapolated to C^{-2}=0 and the obtained E_{fb} values for blank and PA modified samples are indicated. B: The M-S of a sample with thicker TiO_2 protection layer was added (blue trace), showing a behavior that can be explained by a sum of the capacitances of unmodified TiO_2 (protection layer) and shifted TiO_2 (substrate TiO_2). Dotted lines represent the linear fits of the two distinct linear regions, pointing to E_{fb} values which are very close to the ones obtained in A.

This behavior can only be observed in a narrow TiO_2 protection layer thickness window, because for very thin films, the TiO_2 does not fully develop band bending and E_{fb} cannot be obtained. On the other land, thick TiO_2 protection layers completely shield the shifted TiO_2 substrate and only the E_{fb} of the protection layer is measured.

The Mott-Schottky results presented in Figure 34 suggest firstly, that E_{fb} of TiO_2 can be shifted by +300 mV and secondly, that if a thick protection layer is used, the E_{fb} of the underlying TiO_2 substrate is still shifted by the same amount, but cannot be measured by impedance if the protection layer is thicker than 5 nm.

3.2 p-Si/anchor layer/PA/TiO_2

The first step to implement a p-type Si substrate was to deposit the same layer stack used in the previous paragraph and deposit it on p-Si instead of ITO. With the sample architecture p-Si/TiO_2(100nm)/PA/TiO_2(4nm)/Pt, we wanted to measure the shifted E_{fb} of the 100 nm TiO_2 layer and the p-Si substrate. However, this more complicated system made the collection of accurate E_{fb} values impossible due to large uncertainties induced by the additional capacitive elements. Furthermore, the J-V curves of those samples did not show an early V_{onset} as compared to blank samples lacking the PA layer. This behavior was in agreement with our theory, since the photovoltage is generated inside the heterojunction formed by p-Si and 100 nm of n-TiO_2. A dipole placed outside that heterojunction will not increase the photovoltage (We also observed this when we compared n-Si, p-Si and pn-Si substrates, see chapter 3.4). This last statement directly brings us to an important factor that has to be considered when trying to fabricate samples which actually show an increased photovoltage. The thickness of the anchor layer has to be less than a few nanometers, otherwise the anchor layer itself forms a heterojunction with the photoabsorber substrate and the dipole layer on top of that is futile.

Figure 35 shows the band diagrams of unmodified p-Si/TiO_2 and p-Si/anchor layer/PA/TiO_2 devices. The dipole is drawn across the anchor layer/PA interface, and will be explained below in much more detail and supported with experiments and DFT calculations. If the band positions in Figure 35B and C are qualitatively correct, we would expect an increased photovoltages for devices with an internal dipole layer.

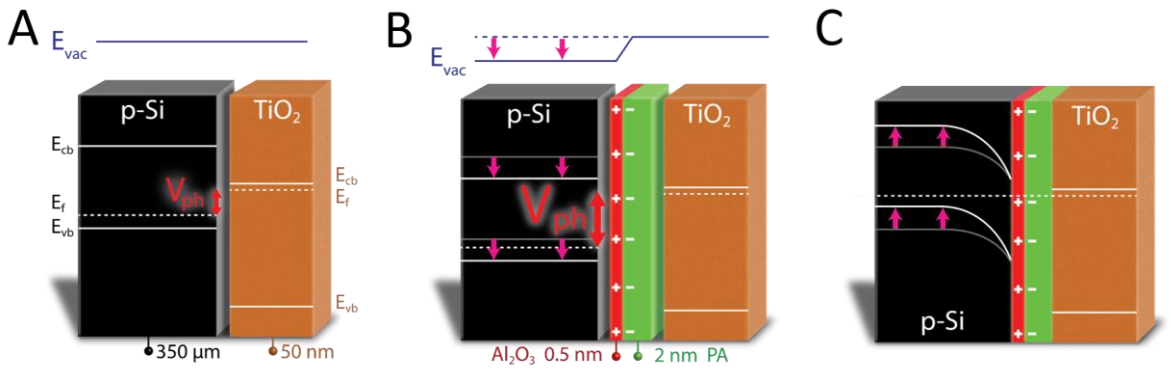

Figure 35. A,B: band diagrams of p-Si/n-TiO_2 and p-Si/anchor layer/PA/n-TiO_2 in flat band condition, and (C) in equilibrium, showing the increased band bending that is obtained with a dipole layer. The dipole layer induces a shift in the band edge, represented by a step in the vacuum energy level (E_{vac}), and therefore higher photovoltage (V_{ph}) can be obtained. Due to the high doping of TiO_2, band bending in the TiO_2 was omitted. Adapted with permission from ref 73.

As a proof of principle we fabricated devices with a 1 nm TiO_2 anchor layer on p-Si, spin coated PA on top, annealed at 120 °C and protected with 20 nm of TiO_2. Pt catalyst was then deposited by photoelectrodeposition (details in experimental section). The blank sample underwent the same treatment, but pure EtOH was spin coated instead of 50 mM PA in EtOH. This allowed us to exclude differences between the samples arising from the EtOH treatment or annealing. Indeed, the PA modified device showed an increased V_{onset} by 200 mV (Figure 36A). V_{onset} of the blank sample is at +0.2 V_{RHE} a value that is commonly reported in literature for p-Si/n-TiO_2 heterojunctions,[56] while the V_{onset} of +0.4 V_{RHE} for the PA sample brings us close to the values reported for pn-Si homojunctions protected with TiO_2.[74] Furthermore, the slope of the photocurrent was very similar in both samples, from which we conclude that the series resistance of the PA modified device is not increased. This finding was surprising, since we used ellipsometry to measure the thickness of the PA layer and found it to be in the order of 10-20 nm. For such thick PA layers, which are thought to be insulating, we expected a largely increased series resistance and therefore lower fill factor.

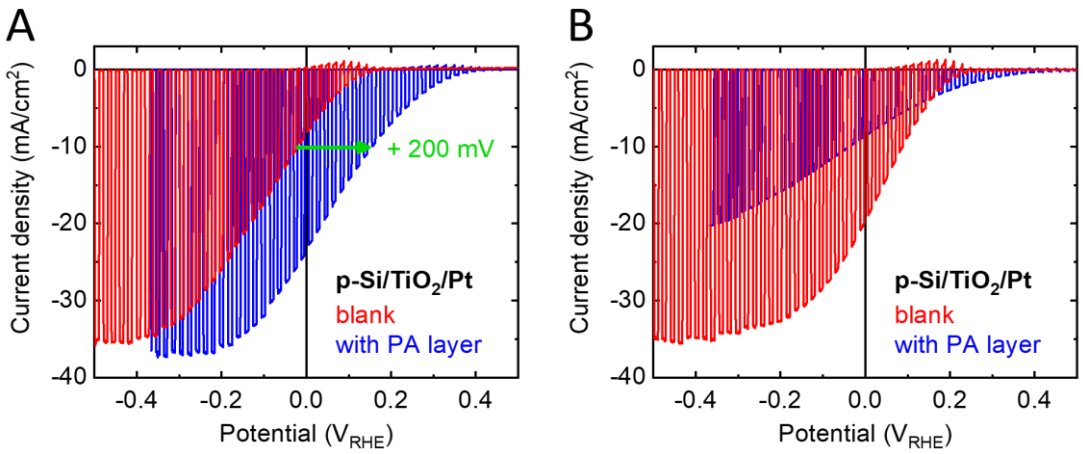

Figure 36. A: J-V plot of blank p-Si/TiO_2(21nm)Pt (red) and p-Si/TiO_2(1nm)/PA/TiO_2(20nm)/Pt (blue) recorded in 1 M H_2SO_4 under chopped illumination. B: the same two device architectures from a different sample batch.

When we tried to reproduce and optimize the samples from Figure 36A, we noticed that the resistivity of the samples with PA layer changed very drastically from batch to batch, even when we used the same deposition conditions. An example of this is given in Figure 36B, where the same fabrication procedure led to a very resistive device, as apparent from the poor fill factor and slope in the blue trace. The V_{onset}, however, is still shifted by 200 mV as compared to the blank sample. For the PA modified samples in Figure 36, we used a 50 mM ethanolic PA solution for spin coating. In the next experiments, we found a strange correlation between PA concentration and the resistivity of the resulting devices. Lower PA concentrations of 25 mM always gave very resistive samples, 50 mM samples were sometimes resistive, but not always (as apparent from Figure 36), while 100 mM almost exclusively gave samples with good resistivity and performance.

The reason for this behavior became more clear when the samples were studied in SEM (Figure 37). Apparently, 25 mM PA solution, spin coated and annealed, yields a very homogeneous PA layer of approximately 20 nm thickness (Figure 37C). On the other hand, PA layers deposited from higher PA concentrations yield a thicker PA layer, which then undergoes Ostwald-ripening under annealing conditions and PA nanospheres are formed on the substrate (Figure 37D). A side view SEM image of the same sample confirms that no PA layer is present underneath the TiO_2 protection layer, except for the PA nanospheres.

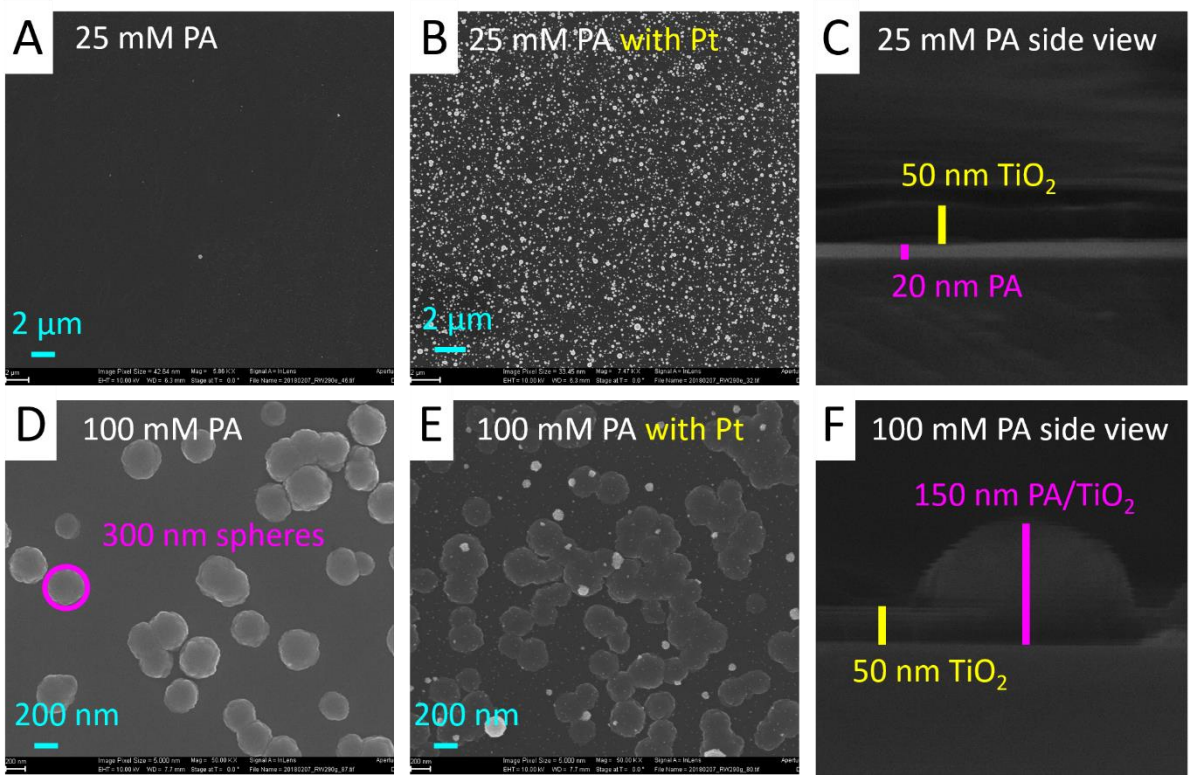

Figure 37. SEM images of p-Si/PA/TiO_2 samples with PA layers made from 25 mM solution (A-C) and 100 mM (D-F). A: flat PA film; B: Pt particles deposited; C: Side view showing a homogeneous 20 nm PA layer covered with 50 nm TiO_2; D: 100 mM PA forms spheres after annealing; E: same sample covered with Pt particles; F: side view showing no homogeneous PA layer underneath the 50 nm TiO_2, but 150 nm high and 300 nm wide PA/TiO_2 particles (including 50 nm of TiO_2, therefore the PA particle itself is 100 x 200 nm).

Our explanation is summed up in Figure 38. Different concentrations of PA solutions spin coated onto a substrate lead to different PA thicknesses. When these PA layers are annealed, they undergo Ostwald-ripening above a certain thickness threshold. We found experimentally, that the driving force for Ostwald-ripening is only large enough for PA layers above 20 nm. This value, however, is very sensitive towards some unidentified experimental conditions, which could be ambient moisture, temperature gradient during annealing, the exact duration of heat-up, annealing and cooldown, the age and impurities of the PA solution etc. This also explains why we obtained very different results for samples fabricated from 50 mM PA solutions, but more consistent results for 25 mM and 100 mM. The protecting layer TiO_2 either covers the flat PA film, or the PA spheres. In the first case, the homogeneous PA layer is very blocking, while in the latter case, the protective TiO_2 is in most of the area in direct contact with the substrate, allowing unhindered electron flow.

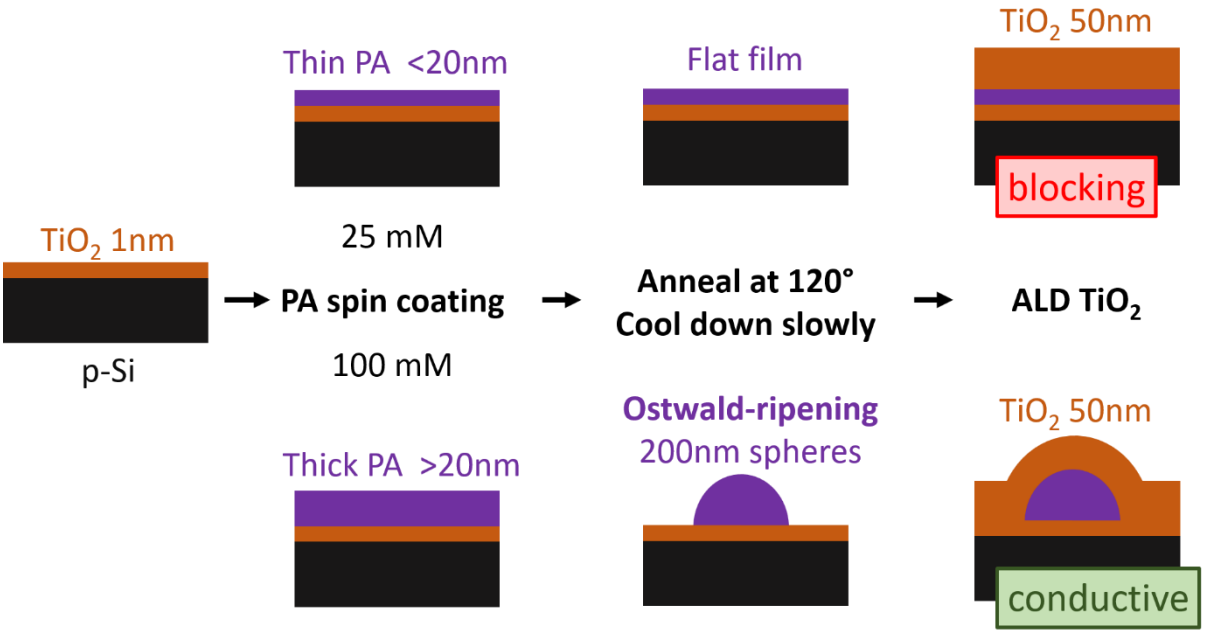

Figure 38. Schematic representation of the sample fabrication process. Different PA concentrations in spin coating give different PA thicknesses. During annealing, Ostwald-ripening takes place, but only for PA layers above a certain thickness. When coated with TiO_2, the flat PA layers acts as an insulator, while PA spheres allow an unhindered electron flow from the substrate to the protective TiO_2.

Another batch of p-Si/PA/TiO_2 samples is presented in Figure 39. In this experiment, different annealing conditions were tested, namely 120 °C in air (the standard conditions, see Figure 36 for more examples) and 80 °C in argon atmosphere. Lower temperatures and oxygen-free conditions are crucial when the whole dipole strategy is applied to substrates which tend to oxidize quickly. The very resistive sample in Figure 39A is one example, where nanosphere formation was not observed, despite 100 mM PA solution being used to deposit the PA layer. On the other hand, when the PA was deposited identically, but the sample was annealed at only 80 °C in argon, the PA sphere formation happened and the sample performed well with a V_{onset} shift of 200 mV and good FF (red trace). However, SEM revealed, that the PA spheres present on this sample are 50 – 100x bigger than the ones show in Figure 37. The increased PA sphere size allowed us to measure EDX and prove directly that the spheres consist of PA due to their high P and O content. This sample batch showed us once more that the PA sphere formation is hard to predict and control and led us to investigate further into very thin PA layer, where Ostwald-ripening is insignificant and tunneling is possible. The PA layer should therefore be thin enough to be conductive, but thick enough to give a large band shift.

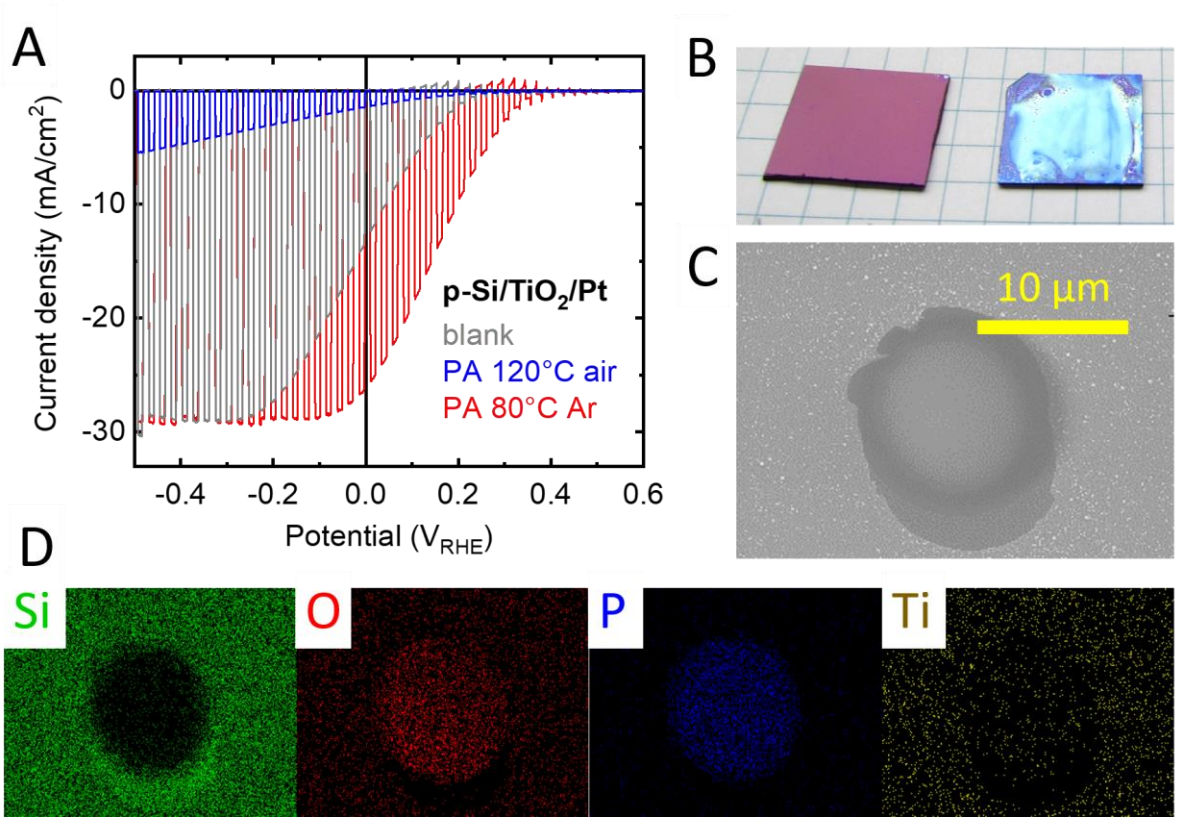

Figure 39. A: J-V plot of blank p-Si/TiO_2(21nm)Pt (grey) and p-Si/TiO_2(1nm)/PA/TiO_2(20nm)/Pt with the PA layer annealed at 120 °C in air (blue) and at 80 °C in Ar (red), recorded in 1 M H_2SO_4 under chopped illumination. B: Photo of the blank and 80 °C Ar samples from A. C: SEM of the same PA modified sample with 10 µm microspheres of PA on the substrate. D: The composition of the microspheres is revealed by EDX, showing the high P and O content.

Thin PA layers were deposited by spin coating PA solutions with concentrations of 1 – 10 mM onto p-Si/TiO_2(1nm). After annealing, rinsing and deposition of protective TiO_2 as well as Pt catalyst, those samples showed an increase in V_{onset} shift with increasing PA layer thickness (Figure 40A). However, already a PA layer made from 5 mM solution has an increased resistivity as compared to the blank sample or samples with thinner PA layer. And the sample with thicker PA layer (10 mM PA; green trace) was too resistive, so that also the V_{onset} is affected and is therefore less shifted than for 5 mM PA. The stability of these devices was compared by keeping them under water splitting conditions at 0 V_{RHE} for 1 hour (Figure 40B). All devices show a modest stability and lost approximately 5 mA/cm^2 of photocurrent after 1 hour. In our system the Pt catalyst is most likely the limiting stability factor and replatinization could bring back some of the lost photocurrent. Here, we did not want to optimize the Pt catalyst for longer stability, instead, the experiment clearly indicated that the PA dipole layer is not limiting the stability and is therefore well protected under the thick TiO_2 layer. This is also obvious from the J-V curves before and after this stability measurements in Figure 40C. Both samples, blank and PA modified, show a decreased FF and photocurrent, but the difference in V_{onset} between the samples is stable at 200 mV.

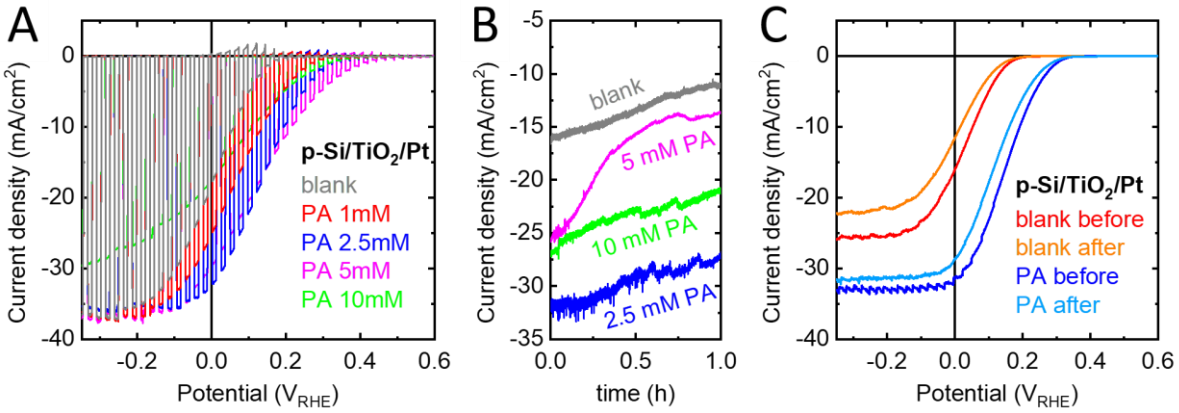

Figure 40. A: J-V plot of blank p-Si/TiO_2(21nm)/Pt and p-Si/TiO_2(1nm)/PA/TiO_2(20nm)/Pt with the PA layers deposited from different PA solution concentrations. Recorded in 1 M H_2SO_4 under chopped illumination. B: 1 hour stability measurements at 0 V_{RHE} under 1 sun illumination. C: J-V plots under illumination recorded before and after a 1 hour stability measurement.

So far, TiO_2 was always used as anchor layer and protection layer, but there are many possible metal oxides that could serve as anchor layer, and ALD is a powerful method to deposit them as very thin and homogeneous layers. And since we only use approximately 1 nm thick anchor layers, we are not restricted to conducting materials, since even insulators are expected to allow tunneling. We therefore fabricated blank samples with the general architecture p-Si/anchor layer/TiO_2(50nm)/Pt. Ga_2O_3 and Al_2O_3 were tested as anchor layer candidates besides TiO_2 and native SiO_2 (Si wafers naturally grow 1.5 nm of SiO_2). For the blank samples, the TiO_2 device performed best (there is actually no anchor layer in that device, just TiO_2 protection layer with 51 nm thickness instead of 50 nm). All other samples showed a later V_{onset} by approximately 50 mV (Figure 41A, dotted lines). This picture changes completely when we measured the devices with different anchor layers and PA layer. As apparent from Figure 41A (solid lines) the PA modified samples all showed an improved V_{onset} as compared to their corresponding blank sample. The SiO_2 device is very resistive, because the native SiO_2 is 1.5 nm thick, slightly more than the ALD deposited layers, and tunneling already becomes difficult. The behavior of the TiO_2 device confirms what we have observed in Figure 40A. Relatively thin PA layers (made from 5 mM PA solution) on TiO_2 already lead to an increased resistivity, but the V_{onset} shift is large (>200 mV). In contrast to this, both, Ga_2O_3 and Al_2O_3 do not show an increase in resistivity as compared to the blank samples. And while the shift of the Ga_2O_3 sample is similar to the TiO_2 sample, we measured an astonishing V_{onset} shift of 400 mV for the Al_2O_3 sample!

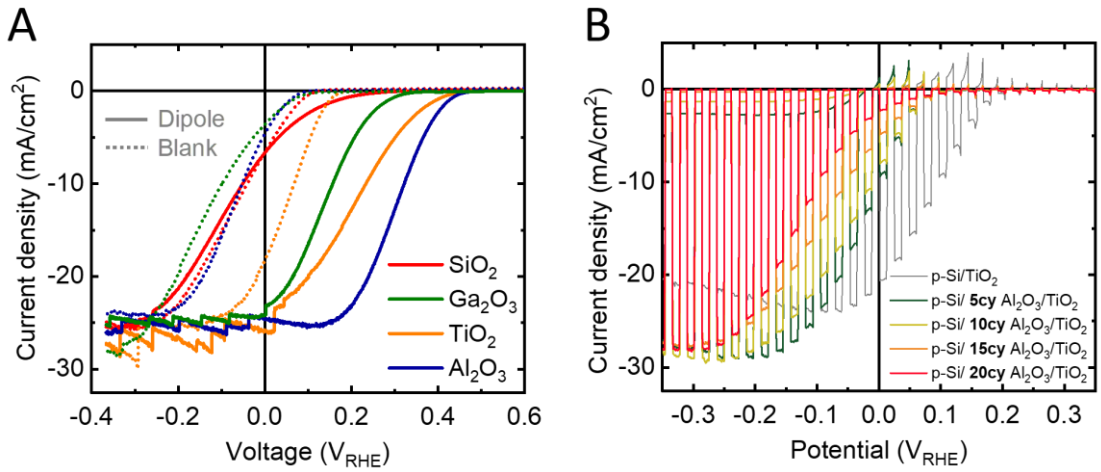

Figure 41. A: J-V plots of devices with the general structure p-Si/anchor layer/TiO_2/Pt (Blank) or p-Si/anchor layer/dipole/TiO_2/Pt (Dipole) recorded in 1M H_2SO_4 under 1 sun illumination. B: J-V plots of devices with varied Al_2O_3 anchor layer thickness. 5cy denotes that the layer was deposited using 5 subsequential pulses of trimethylaluminium and water in the ALD process. Illumination was chopped once per second. Reprinted with permission from ref 73.

The importance of the thickness of the anchor layer was discussed above and is also evident when we compare the devices with <1 nm anchor layers (Ga_2O_3 and Al_2O_3) in Figure 41A with the 1.5 nm SiO_2 device. This finding was confirmed when we fabricated devices with different Al_2O_3 anchor layer thicknesses (Figure 41B). The optimum seems to lie between 5 and 10 cycles of ALD-Al_2O_3, corresponding to 0.4 – 0.8 nm of Al_2O_3, while >15 cycles already increase the series resistance of the full device drastically. After fabricating more devices, we found that 10 cycle Al_2O_3 samples are more reproducible and therefore used 10 cycles for all subsequent experiments.

In all of the devices with p-Si as photoabsorber and n-TiO_2 as heterojunction partner and protection layer, the photoabsorber is not in direct contact with the electrolyte, making those devices buried junction PEC cells instead of “classical” PEC cells. Buried junction PEC cells are very similar to heterojunction PV cells, the main difference being whether a catalyst is deposited onto the heterojunction or a front contact. The PEC device with the catalyst can be placed in an electrolyte to split water, while the PV front contact is connected to a wire to allow the use of the photogenerated electricity. With the help of Johannes Löckinger from the thin films and PV laboratory at Empa, CH-Dübendorf, we fabricated PV cells from our samples by depositing AZO and a Ni grid on top of the TiO_2 instead of the Pt catalyst (Figure 42A). As expected, also the V_{oc} of the PV increased when an anchor layer/PA stack is introduced. Figure 42B compares the performance of blank and dipole modified PEC and PV cells. Both show a photovoltage increase of 200 mV, and in consequence a higher FF and power conversion efficiency. The figures of merit for the PEC and PV cells shown in Figure 42 are summarized in Table 1 (PV) and Table 2 (PEC).

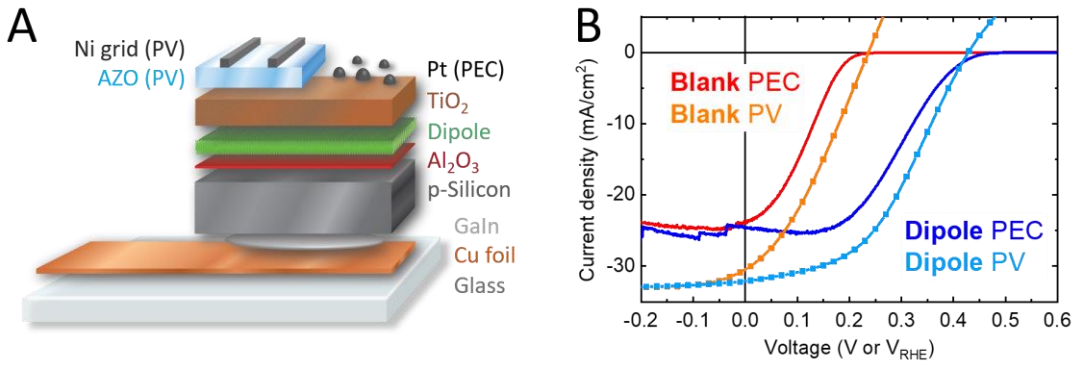

Figure 42. A: Device architecture of the PV and PEC cells used in this study. B: Current density-Voltage plots of PV and PEC cells made from p-Si/n-TiO_2 well as p-Si/anchor layer/PA/n-TiO_2. PEC measurements in 1 M H_2SO_4 and 1 sun. Adapted with permission from ref 73.

Table 1: Performance of PV cells in Figure 42B. Reprinted with permission from ref 73.

sample	**PCE (%)**	**V_{oc} (V)**	**J_{sc} (mA/cm^2)**	**FF (%)**
p-Si/TiO_2	2.6	0.237	31.9	34.4
p-Si/dipole/TiO_2	6.2	0.430	32.2	45.1

Table 2: Performance of PEC cells in Figure 42B. The onset potential was defined as the potential where the photocurrent reaches 0.5 mA/cm^2. Reprinted with permission from ref 73.

sample	**ABPE (%)**	**$V_{onset\ 0.5mA/cm2}$ (V_{RHE})**	**J at 0 V RHE (mA/cm^2)**
p-Si/TiO_2	1.5	0.190	23.9
p-Si/dipole/TiO_2	4.8	0.404	24.6

We observed an increase in V_{onset} shift with higher PA concentrations used for spin coating (Figure 43). From the blank sample and the one with 1 mM, which yields a sub-monolayer PA coverage, to 20 mM, (1.5 – 2 nm PA layer thickness), we were able to gradually move V_{onset} over a range of 400 mV. This experiment was similar to the one in Figure 40A. The big difference was that with TiO_2 as anchor layer, a PA solution concentration of 5 mM already resulted in resistive devices, while on Al_2O_3 anchor layer, we deposited thicker PA films from up to 10 mM PA solution without any increase in resistivity. This allowed us to obtain larger V_{onset} shifts, while maintaining a high FF. At PA concentrations ≥20 mM, the resistivity also increased, while V_{onset} stagnated and even deceased for PA concentrations of 50 or 100 mM. This trend is also evident from Figure 43B, where efficiency and V_{onset} of the devices are plotted against the PA concentration. PA layers spin coated from 10 - 20 mM solutions showed the highest V_{onset}, while retaining a low series resistance and in consequence the best performance.

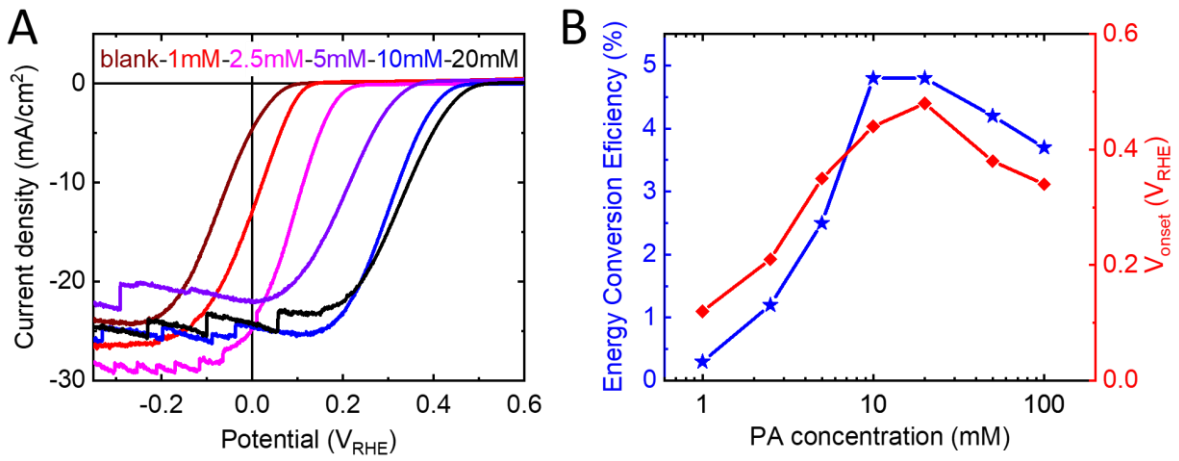

Figure 43. A: Current density-Voltage plots of PEC devices with the structure p-Si/Al_2O_3/PA/TiO_2/Pt with different PA concentrations used for spin coating of the dipole layer (maroon: no dipole layer; black: 20 mM PA). Linear sweeps were recorded in 1 M H_2SO_4 and 1 sun illumination at scan speed of 10 mV/s. B: Dependence of energy conversion efficiency and onset potential (V_{onset}) on the PA concentration used to make the dipole layer. Adapted with permission from ref 73.

Our stability measurements on p-Si/Al_2O_3/PA/TiO_2/Pt devices in 1 M H_2SO_4 and 1 sun illumination at 0 V_{RHE} confirm that the PA layer is well protected from the electrolyte and does not limit the stability of the PEC device. Figure 44A shows the J-V curves of a blank sample as well as PA modified sample before and after a 2 h stability test under the conditions mentioned above. V_{onset} and J_{SC} did not change after 2 h and the FF even increased slightly, probably due to some favorable stabilization process taking place in the device. After approximately 5 hours of stability test, both samples, blank and dipole, start to degrade and completely lose their performance after another few hours. This is due to detachment of the Pt catalyst from the surface and then degradation of the TiO_2 by accumulated charges that cannot be used for proton reduction in the absence of a catalyst.[75]

The stability of the PV devices was tested by Johannes Löckinger at Empa. Blank and dipole modified samples were kept at 80 °C under 1 sun illumination at maximum power point for 6 days (Figure 44B). After this so called "heat-light-soaking" experiment, all samples, blank and dipole modified, showed the same behavior: V_{oc} increased slightly (40 mV), J_{sc} was unchanged and FF decreased. The dark currents in Figure 44B (dotted lines), reveal that the series resistance increased during the heat-light-soaking and this higher series resistance is responsible for the lower fill factor under illumination.

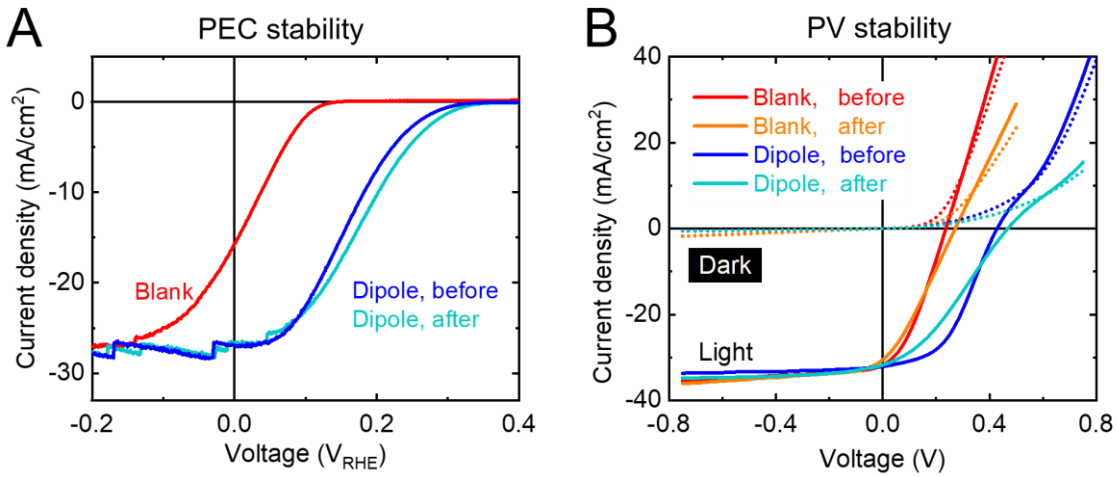

Figure 44. A: Current density-Voltage curves of a p-Si/Al_2O_3/PA/TiO_2/Pt sample before (blue) and after (light blue) a 2 hour chronoamperometry measurement at 0 V_{RHE} in 1 M H_2SO_4 under 1 sun illumination. A linear sweep measurement of the blank sample p-Si/TiO_2/Pt (red) is also included. B: Current density-Voltage plots of PV cells in the dark (dotted lines) and under 1 sun illumination (solid lines) before and after heat soaking at 80 °C and 1 sun illumination with max power point tracking for 6 days in N_2 atmosphere. Adapted with permission from ref 73.

From Figure 45 it is obvious that most of the changes in all samples took place in the first hours of the 6 day stability experiment and an equilibrium is established after that, and the samples would be stable for much longer. As a side effect, one of the processes responsible for this equilibrium also gives rise to a slightly improved V_{oc} after the stability experiment. The point we want to emphasize is that all of the observed processes taking place during the stability measurements (in PEC and PV) occur in the blank and PA modified samples and are therefore not induced by the PA. We therefore conclude that the PA dipole layer has no negative effect on the stability of the PEC and PV devices.

Mott-Schottky analysis was used to determine the built-in voltage of blank and dipole modified p-Si/TiO_2 PV cells (Figure 46A). The inverse of the squared space charge capacitance ($1/C^2$) was plotted against applied voltage. The negative slope of the curves confirm the p-type doping of the Si wafer. The PV cell with PA dipole layer has a built-in voltage of 0.49 V, which corresponds to a shift of 270 mV as compared to the blank sample (0.22 V). Those values are in good agreement with the V_{oc} observed for the same samples in Figure 42B and also the E_{fb} shifts obtained from PEC impedance on TiO_2 and TiO_2/PA (Figure 34) are very similar (270 – 300 mV).

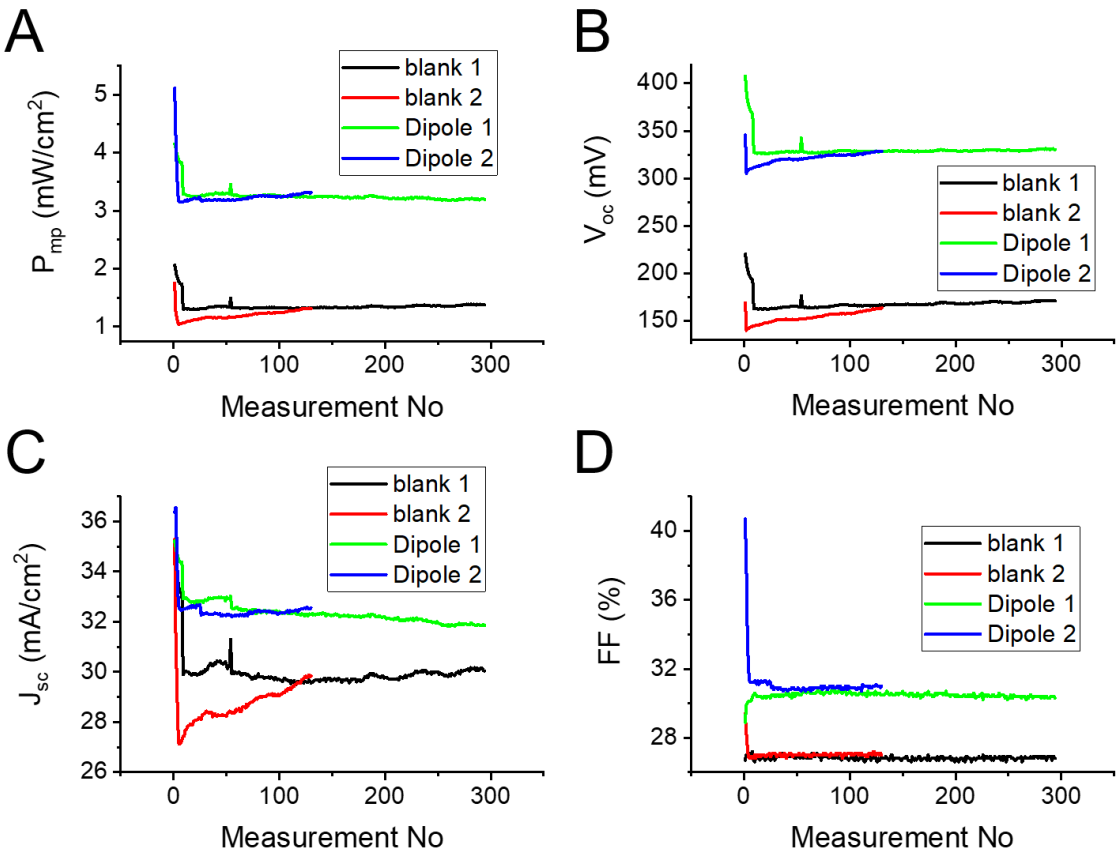

Figure 45. Figures of merit of four solar cells during heat-light soaking experiments. J-V curves were automatically recorded every 30 min and the full experiment lasted for 6 days (samples Blank 1 and Dipole 1) or 2.5 days (Blank 2 and Dipole 2). A: output power at maximum power point, B: development of the open circuit voltage V_{oc}, C: short-circuit current (J_{sc}), D: fill factor (FF). Adapted with permission from ref 73.

The effect on the performance of the devices if only anchor layer or only PA layer are deposited (p-Si/Al_2O_3/TiO_2 and p-Si/PA/TiO_2) is shown in Figure 46B. It turns out that an insulating Al_2O_3 layer drastically decreases the performance of the device, probably by introducing a dipole in the undesired direction. Al_2O_3 is known to passivate surfaces by the field passivation effect. if that is the case, negative charges would be incorporated in the Al_2O_3 layer, which would explain the parasitic dipole.[76–78] On the other hand, a PA layer without anchor layer still shows higher photovoltage than the blank sample. We assume that in this case, a very thin native SiO_2 layer, which we cannot exclude with our synthesis technique, can act as an alternative anchor layer.

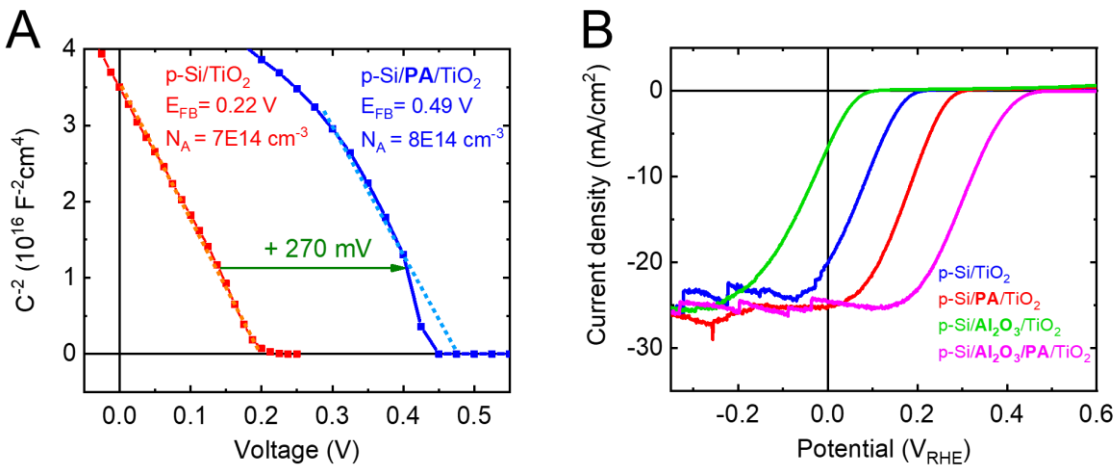

Figure 46. A: Mott-Schottky Analysis of p-Si/TiO_2 and p-Si/Al_2O_3/PA/TiO_2 PV cells obtained from impedance measurements in the dark. B: J-V plots of different devices recorded in 1M H_2SO_4 under 1 sun illumination. Adapted with permission from ref 73.

3.3 PA characterization

As a next step, we wanted to characterize the PA layer in depth. Some findings made us doubt that the PA layer remains chemically unchanged after spin coating and annealing. For example, crystalline PA readily dissolves in ethanol. When we spin coated 2 nm of PA onto a p-Si/TiO_2 substrate, this PA layer would not dissolve in ethanol even after prolonged ultrasonication. We therefore wanted to exclude that the PA (H_3PO_3) was oxidized to phosphoric acid (H_3PO_4) and maybe polymerized to polyphosphoric acid, which would explain the decreased solubility in ethanol. The XPS core level spectra for P 2s and P 2p (Figure 47) confirm firstly that a P containing layer is present on the samples, and secondly, that the P species is actually PA (H_3PO_3) and not some oxidized or polymerized species, as the binding energies match with the values reported for PA in literature.[79]

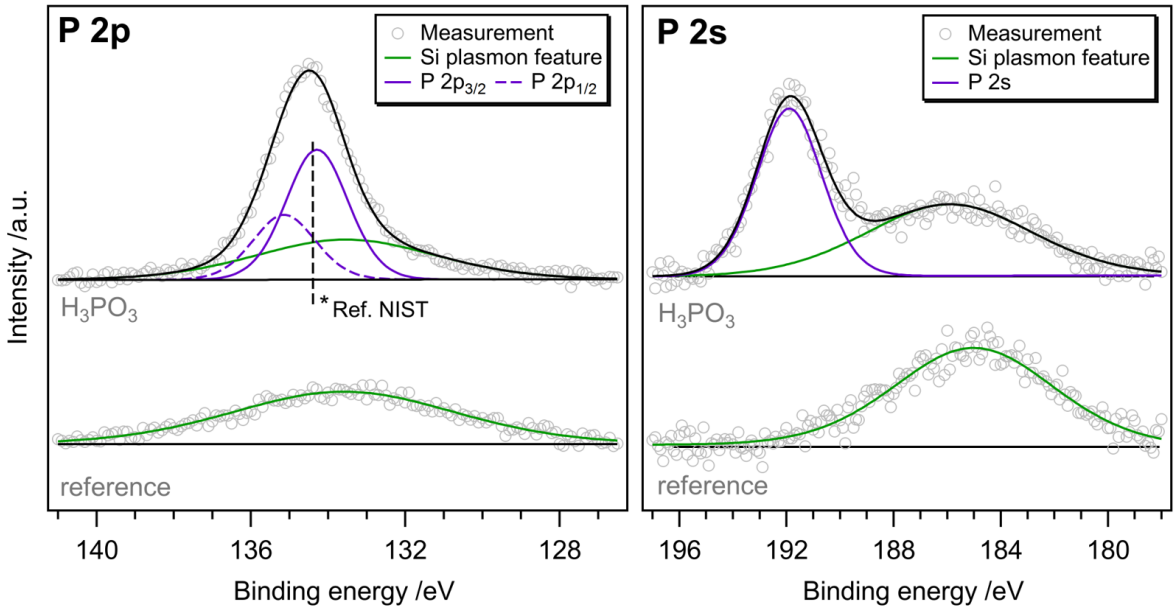

Figure 47. XPS core level spectra for P 2p (A) and P 2s (B) for p-Si/Al_2O_3/PA (top) and p-Si/Al_2O_3 reference (bottom). The P $2p_{3/2}$ core level binding energy for PA reported in the NIST database[79] (134.30 eV) is marked as black dashed line in A. Adapted with permission from ref 73.

We further confirmed this finding with high resolution ESI-MS. A p-Si/Al_2O_3/PA sample was ultrasonicated in 1 mM NaOH solution. The phosphonate anchoring group is unstable in basic conditions and therefore detached from the substrate. The resulting NaOH solution, containing the PA, was then injected into the HR-ESI-MS. The measurement revealed that only PA was present, and no oxidized or polymerized species could be detected (Figure 48).

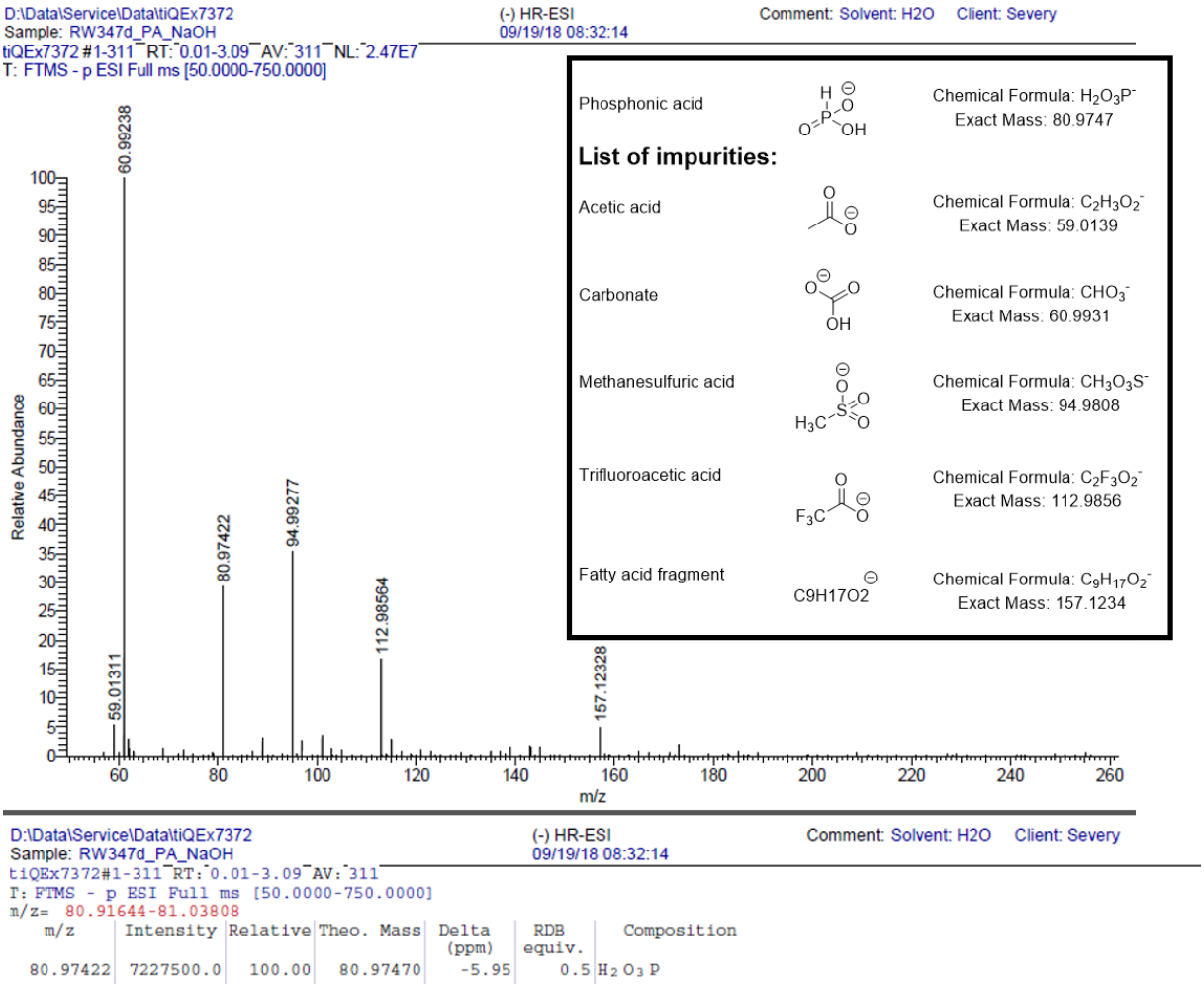

D:\Data\Service\Data\tiQEx7372
Sample: RW347d_PA_NaOH
(-) HR-ESI
09/19/18 08:32:14
Comment: Solvent: H2O Client: Severy

tiQEx7372#1-311 RT: 0.01-3.09 AV: 311
T: FTMS - p ESI Full ms [50.0000-750.0000]
m/z= 80.91644-81.03808

m/z	Intensity	Relative	Theo. Mass	Delta (ppm)	RDB equiv.	Composition
80.97422	7227500.0	100.00	80.97470	-5.95	0.5	H_2O_3P

Figure 48. High resolution electron spray ionization mass spectrum (HR-ESI-MS). PA was spin coated onto p-Si/Al_2O_3, annealed and then rinsed with EtOH and dried in N_2 stream. The sample was then ultrasonicated in 1 ml of 1 mM NaOH to remove the compounds bound to the Si surface and the obtained solution was analyzed by HR-ESI-MS, showing that PA is not oxidized during annealing and not washed away by EtOH rinsing. The inset shows a list of common impurities that are also detected. Adapted with permission from ref 73.

The morphology of the PA layer deposited by spin coating of a 10 mM PA solution was investigated by SEM and AFM. The SEM images in Figure 49A, B show that etched p-Si as well as p-Si/Al_2O_3 are very flat and no morphology is visible at the resolution limit of the SEM. We presume that nanofeatures of approximately 10 nm size could be observed. However, we expect that commercial p-Si wafers are almost atomically flat and also 0.5 nm Al_2O_3 should deposit homogeneously. The small white dots visible in Figure 49A, B, C are dust particles according to their high C content and were only used for focusing on the otherwise perfectly homogeneous surface. Spin coated PA (before annealing) is visible as slightly lighter pattern on the Si background (Figure 49C). For this sample, we detected a P content of 0.3% (±0.1) which is close to the detection limit of the EDX machine. After annealing, the PA pattern was mostly gone, but similar P and O contents were detected, implying that the PA layer is still present,

but its morphology has adopted the flatness of the surface and no nanostructure is visible anymore due to its homogeneity and thinness.

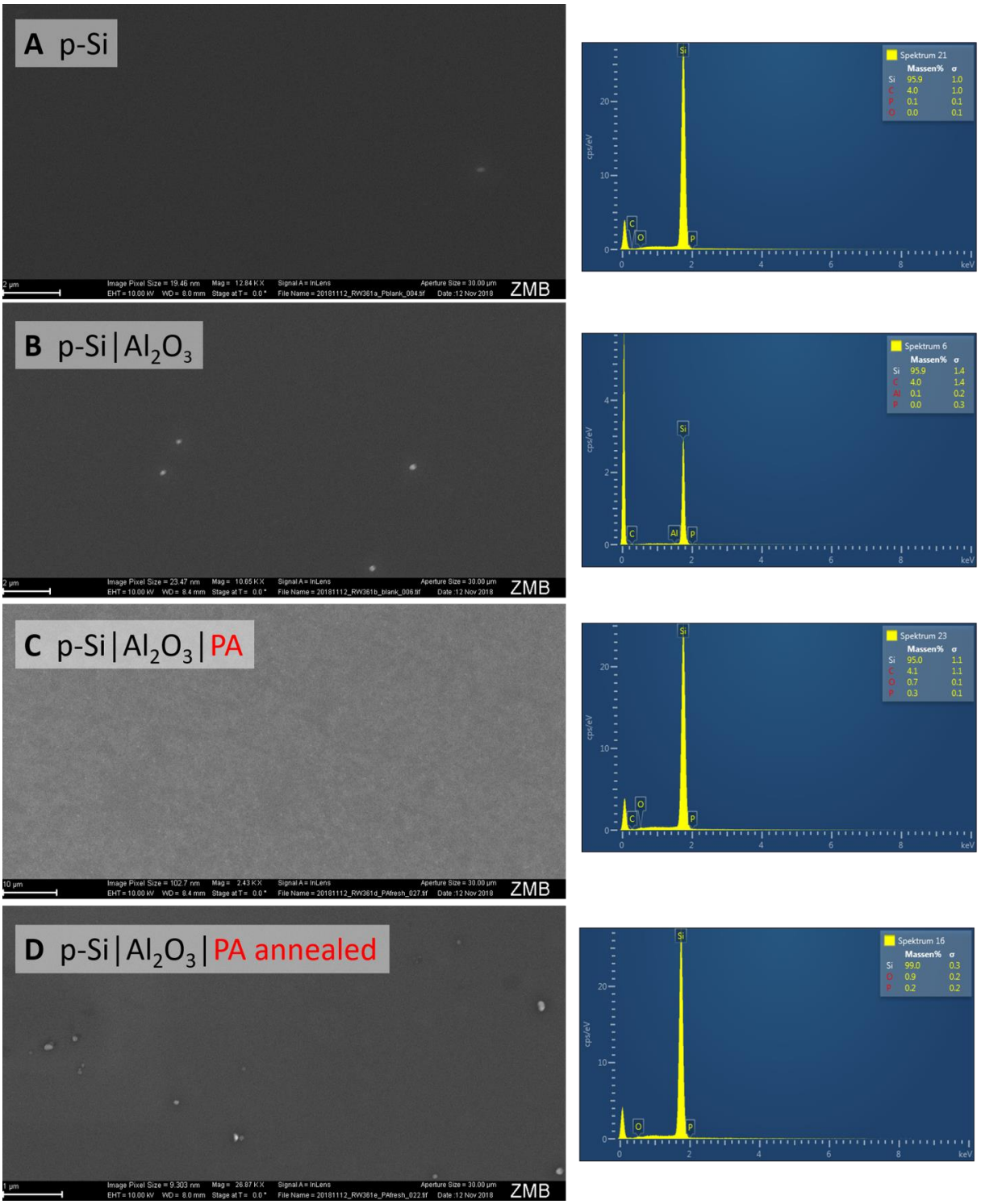

Figure 49. SEM images (left) and EDX analysis of a small section of the same area (right). A: etched p-Si surface. B: etched p-Si surface with 0.5 nm Al_2O_3 layer. C: p-Si/Al_2O_3 with PA spin coated. D: p-Si/Al_2O_3/PA after annealing, rinsing with EtOH and drying in N_2 stream. Note that the white spots visible in samples A, B and D are dust particles showing a high C content in EDX. Rerprinted with permission from ref 73.

Similar results were obtained from AFM mapping (Figure 50). Both samples, blank and PA modified, show a mean roughness of less than 0.5 nm.

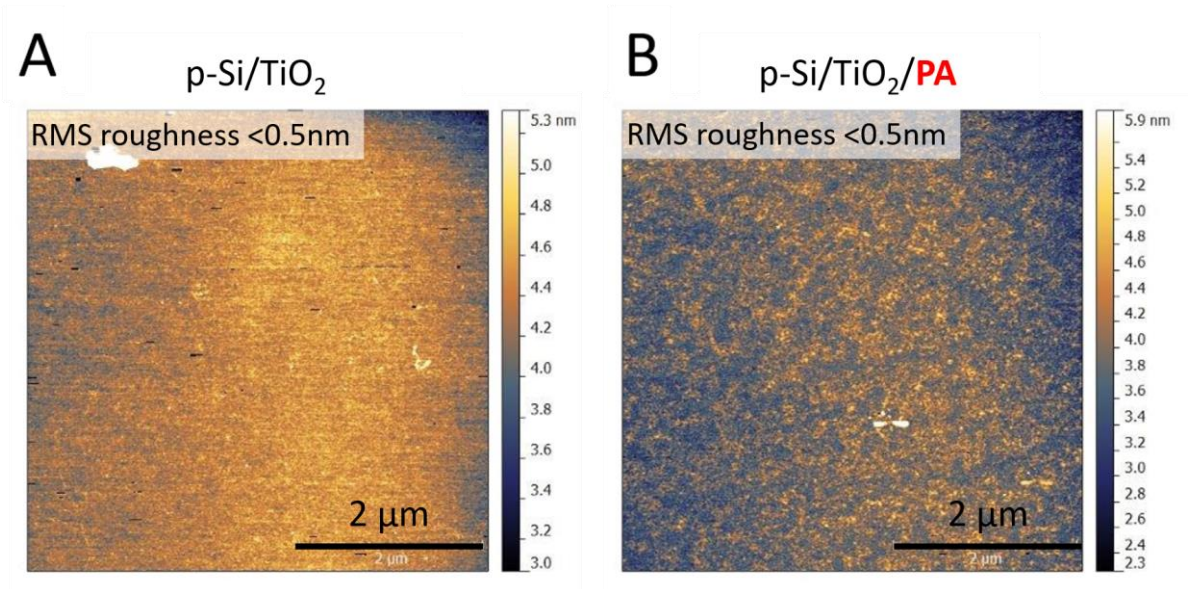

Figure 50. AFM mapping of p-Si with 1 nm TiO_2 layer (A) and p-Si/TiO_2/PA (B). The RMS roughness is <0.5nm for both samples. No increase in surface roughness could be observed after PA treatment suggesting the formation of a uniform and homogeneous PA layer. Reprinted with permission from ref 73.

In summary, the results of XPS and HR-ESI-MS confirm that the dipole layer is actually PA, which apparently does not undergo oxidation or polymerization or any other chemical reaction during annealing and the other deposition steps. SEM and AFM then revealed the flat and homogeneous nature of the PA layer obtained with optimized spin coating conditions (10 mM). Furthermore, those conditions gave very reproducible samples in contrast to the unpredictability induced by thick PA layers, which then undergo Ostwald-ripening (Figure 37, Figure 38).

3.4 DFT calculations TiO_2/PA

As mentioned previously, we attribute the dipole behavior we observe to the replacement of OH groups on the surface of the anchor layer with phosphonate groups as schematically represented in Figure 51A. According to this theory, more electron withdrawing (or less electron donating) functional groups on the substrate surface decrease the electron density on the surface of the substrate and therefore move its bands to more positive energies (on RHE scale). Or in other words, if the surface modification decreases the electron density in the substrate, it's harder to remove one more electron into the vacuum and the energy of the bands on the vacuum scale decreases. With this explanation,

it's trivial that replacing more of the surface OH groups with phosphonate groups will result in a larger band shift. However, this effect only explains the increasing band shift from bare substrate to full PA monolayer coverage. In our experiments, we found that the band shift is even larger when PA layers of 1.5 – 2 nm are deposited, corresponding to 4 – 5 PA monolayers.

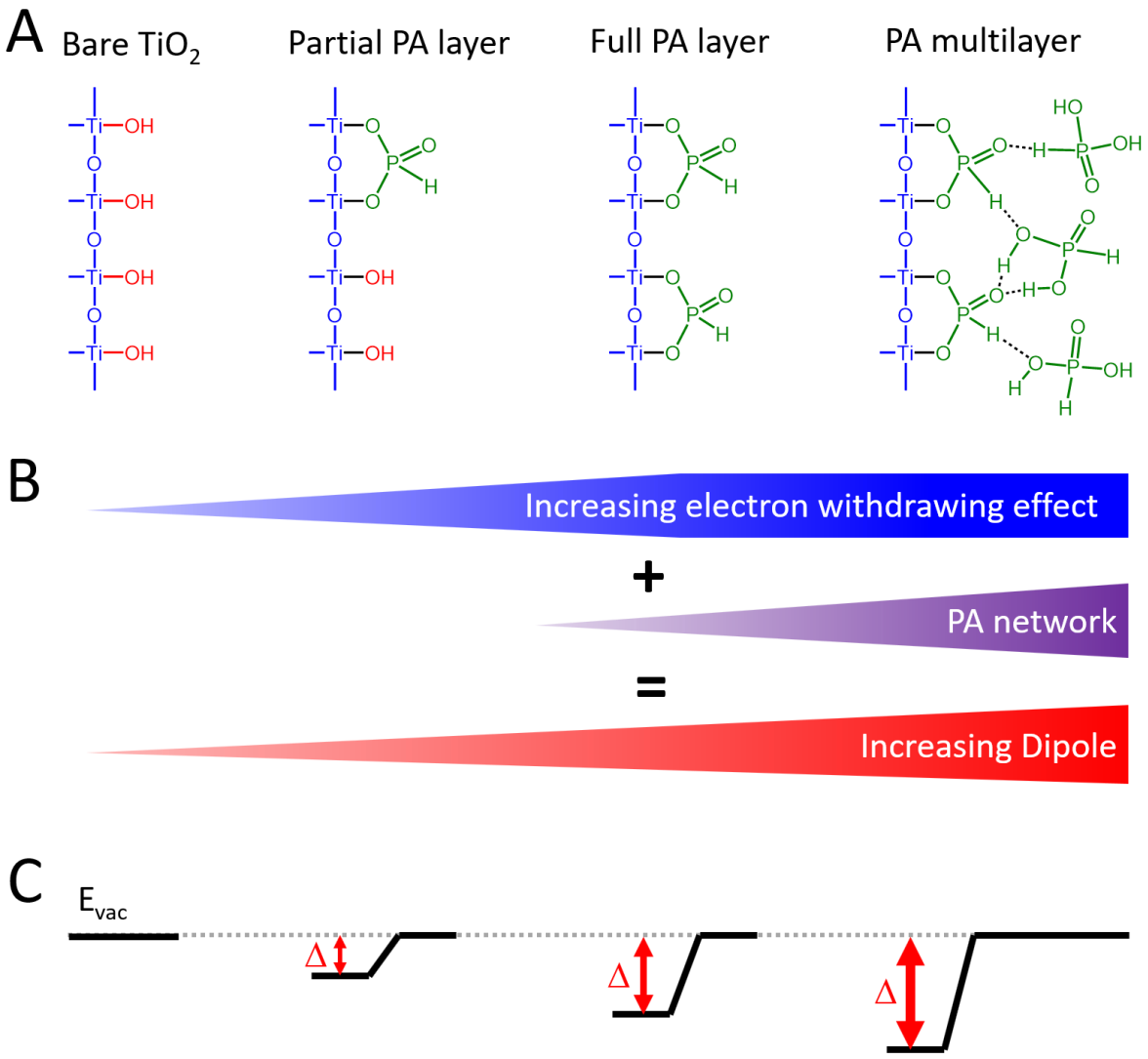

Figure 51. A: Schematic representation of -OH terminated TiO_2 with increasing PA surface coverage and PA multilayer. B: Electron withdrawing effect increases from bare TiO_2 to full monolayer. DFT calculations suggest that going from PA mono- to multilayer induces changes at the anchor layer/PA interface, resulting in an increased dipole. These combined effects add up to an increasing dipole over the range of sub-monolayer to full monolayer to multilayer. C: Dipole (Δ) represented as a step in the vacuum energy, with increasing magnitude going from sub-monolayer to multilayer. Adapted with permission from ref 73.

We suggest (and DFT results presented below confirm) that the PA multilayer network slightly rearranges the PA molecules, which are covalently bound to the substrate. This PA network effect results in a larger dipole than just a PA monolayer. Figure 51B and C show that the observed dipole is

an addition of the two effects of increasing electron withdrawal up to a PA monolayer and PA network for PA multilayers. For the DFT calculations, we started a collaboration with the computational chemistry group of Professor Jürg Hutter at UZH and all calculations reported herein were performed by Dr. Tiziana Musso.

At the time we planned the DFT modeling we only used TiO_2 as anchor layer and we therefore chose a TiO_2 substrate for all calculations. In the literature, a variety of different binding modes of PA to TiO_2 is reported, ranging from monodentate[80] to different bidentate modes.[81,82] For our calculations, a slab of 5 layers of bulk-like TiO_2 was modified with one molecule of PA. The PA molecule was mirrored on the bottom side of the TiO_2 slab to avoid spurious dipole effects. The results suggest the bidentate B2 binding mode to be the most stable one (Figure 52) and this binding was used for the following calculations.

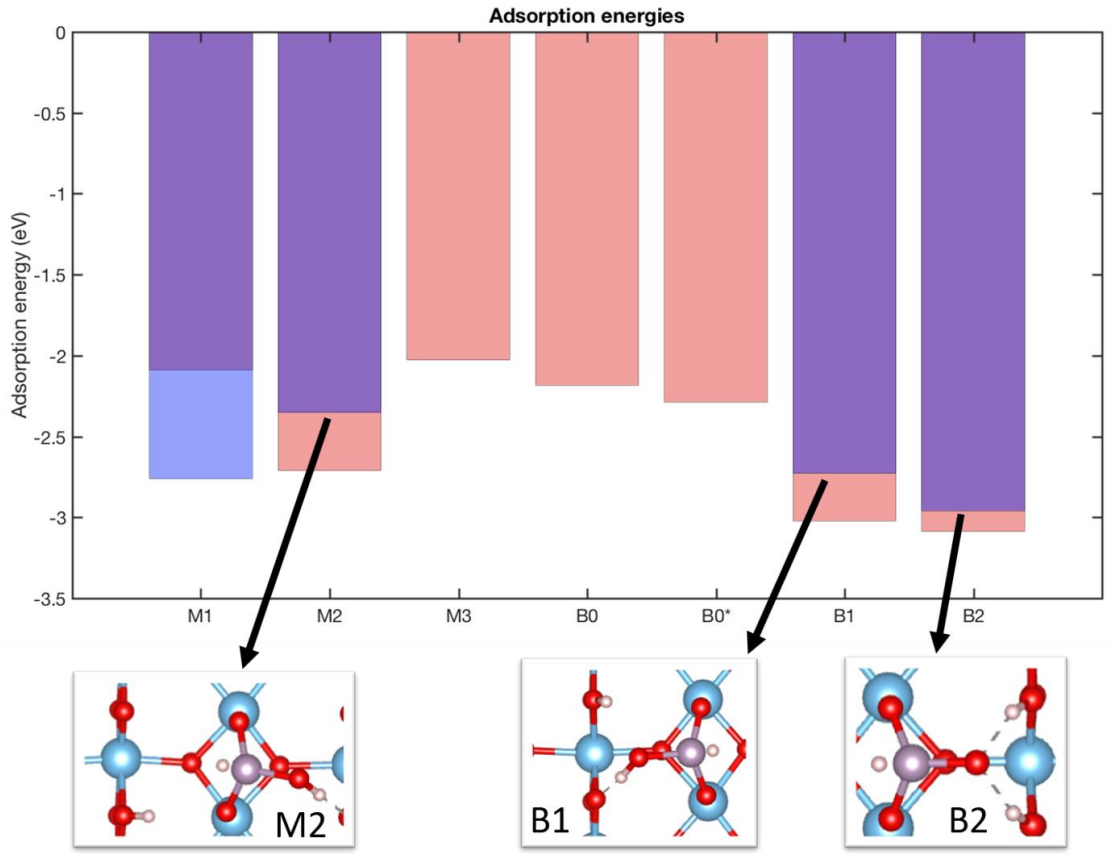

Figure 52. Adsorption energies of different PA binding modes on rutile TiO_2 (110). M stands for monodentate, B for bidentate. Pink trends are referred to our work, while violet ones are taken from Luschtinetz et al.[82] The atomic PA structures are shown in the insets. In the B2 mode 2 H atoms of PA form a bond with two adjacent titania O atoms, remaining coordinated to the O atom of PA. Calculations by T. Musso. Adapted with permission from ref 73.

Next, the TiO_2 anchor layer was modeled with a three layer rutile TiO_2 (110) slab with its surface terminated with hydroxyl groups (Figure 53A,B), because the presence of surface OH groups in the experimental devices is evident from the ALD growth mechanism (subsequent pulses of TDMAT and water) and OH groups on ALD grown TiO_2 were also found experimentally.[83–85] We then subsequently placed additional PA molecules onto the OH terminated TiO_2 until full PA coverage was reached with 4 PA molecules (Figure 53C, D). We found experimentally that the largest V_{onset} shifts were obtained with up to 2 nm thick PA layers and we modelled those thick PA multilayers by adding a crystalline PA layer on top of the fully PA covered TiO_2 slab. For this we had to slightly strain the crystalline PA to match the TiO_2 substrate. The stack was then equilibrated for a few picoseconds at 300 K with ab-initio molecular dynamics simulations. We modeled two different multilayer thicknesses with two and four layers of crystalline PA, hereafter referred to as "thin" and "thick" multilayer (Figure 53E,F).

The work function values (Φ) were calculated according to a procedure reported in literature.[86,87] Basically, we took the difference in electrostatic potential between surface of the TiO_2/PA slab (V_o^{slab}) and the average electrostatic potential in the middle of the slab (V_m^{slab}). The obtained values were then referenced to the work function of the bulk TiO_2 according to:

$$\theta = \left(V_o^{slab} - V_m^{slab}\right) - \left(E_F^{bulk} - V_m^{bulk}\right)$$

Where E_F^{bulk} is the Fermi energy of bulk TiO_2. Using this procedure, we obtained the band positions for all configurations.

The calculated band positions are shown in Figure 53G. With the exception of the "1 PA" configuration, where the bands are shifted to slightly more positive values, all other configurations shift the bands to more negative values (on the vacuum scale; more positive on a RHE scale) with increasing PA coverage. In our simulations the shift can be increased even more, as we go from a full PA monolayer ("4 PA" configuration) to a PA multilayer with 2 additional PA layers on top of the first PA monolayer ("thin" configuration). And the largest band shift is obtained with a "thick" PA layer, meaning that 4 PA layers were added on top of the first PA monolayer. We assume that the PA multilayer induces a restructuring at the TiO_2/PA interface, leading to an increased dipole. This restructuring could be a spatial effect, meaning that the covalently bound PAs are slightly moved or tilted, which could then result in a decreased electron donating effect of the PA. The same effect could arise from the extended hydrogen bonding network of the PA multilayer.

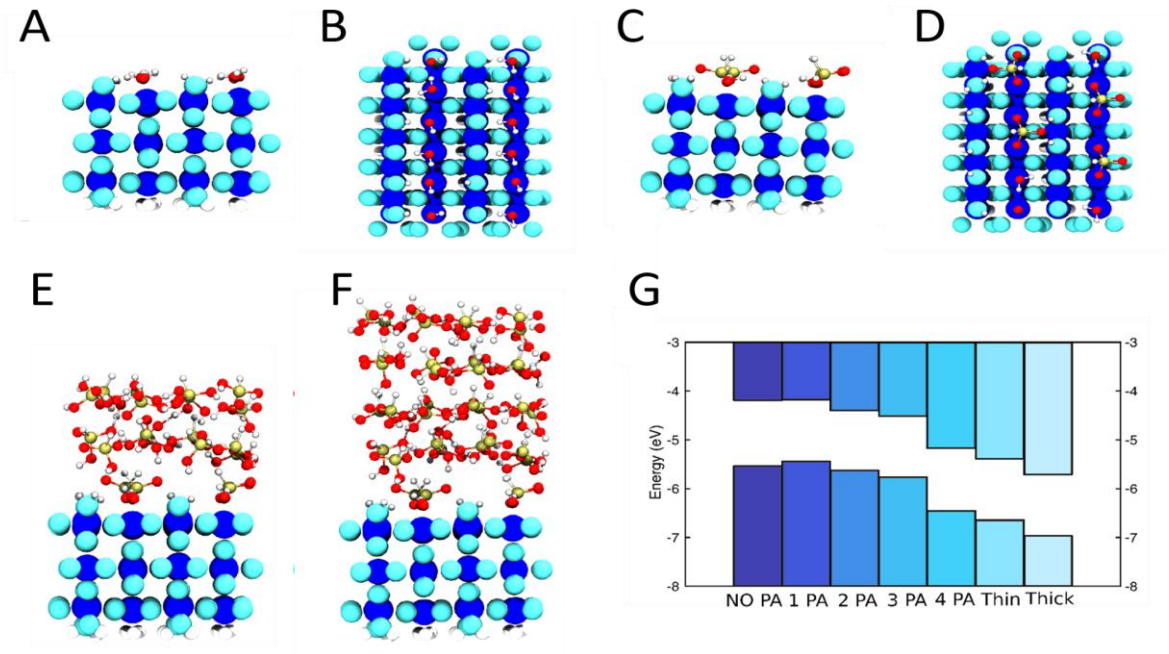

Figure 53. Optimized configurations of hydroxylated TiO_2 (A,B) and TiO_2/PA with maximum PA coverage (C,D), TiO_2 with a thin PA multilayer (E) and thick PA multilayer (F). Color code: blue atoms represent Ti, cyan atoms the O of titania, red is for O, gold for P and white for H. All titania atoms are enlarged for clarity purposes G: bands alignment (top: conduction band, bottom: valence band) for different coverages of PA on TiO_2, namely from left to right: fully hydroxylated TiO_2, TiO_2 with 1, 2, 3 and 4 PA molecules adsorbed on top as well as TiO_2 with a thin and thick PA multilayer. The bands are shifted downwards with increasing PA coverage. Reprinted with permission from ref 73.

Our calculations nicely reproduce the trends we observed experimentally. We therefore conclude that the 3 layer TiO_2 slab is an appropriate model for the anchor layer we used in our devices. Furthermore, we expect that the two observed trends, direction of the band shift and increasing shift with increasing PA coverage, would be the same for other metal oxide anchor layers.

Further experiments confirm that a dipole formed at the anchor layer/PA interface. Firstly, we performed XPS measurements in collaboration with Dr. Sebastian Siol from Empa in Dübendorf. We measured a device with the architecture p-Si/Al_2O_3 (called "reference" in Figure 54). From this sample we obtained binding energies for Si, SiO_2 (which naturally formed on the surface of the Si wafer) and Al_2O_3 as shown in Figure 54B, bottom trace. We thereafter measured p-Si/Al_2O_3/PA samples (with and without annealing at 120 °C for 10 minutes). We observed that all binding energies for Si, SiO_2 and Al_2O_3 were shifted to higher energies upon PA deposition (Figure 54B, middle and upper trace). And, more interestingly, the layers closer to the surface of the device (namely Al_2O_3 and SiO_2) are shifted more than the Si binding energy from deeper within the Si bulk. In Figure 54A the binding energies of the reference sample were set to 0, and binding energies for the PA modified samples are given relative

to the reference sample. This experiment told us that the PA layer induces an increased band bending on the order of 0.5 eV on the surface of p-Si/Al_2O_3/PA (the difference between the increase in binding energy in Al_2O_3 and the bulk Si). The increased band bending is induced by a shift in band edge, supporting our theory.

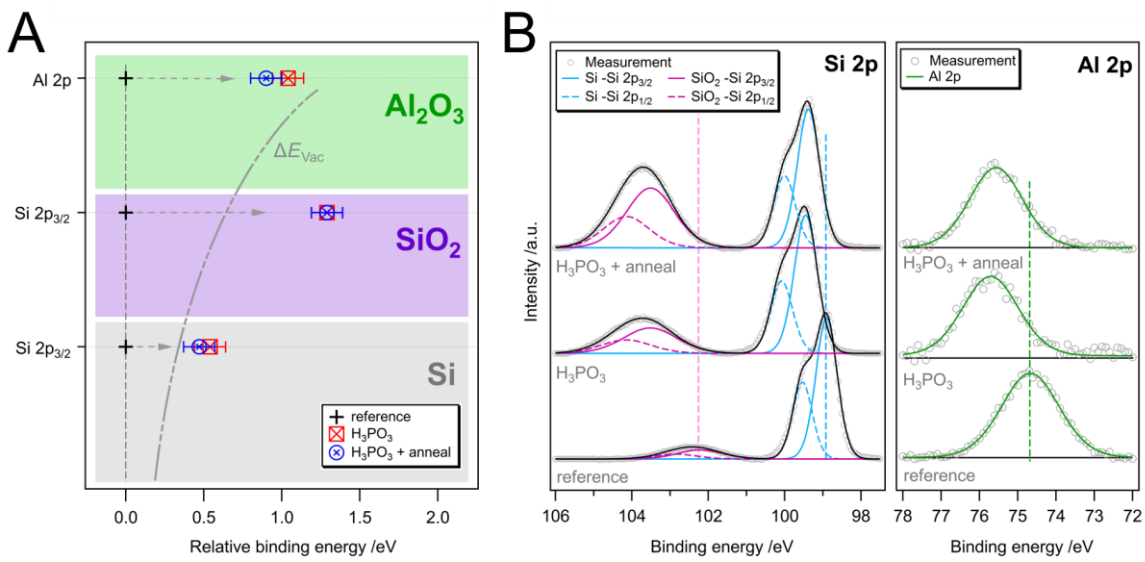

Figure 54. A: Comparison of Si, SiO_2 and Al_2O_3 binding energies between reference p-Si/Al_2O_3 and p-Si/Al_2O_3/PA. Compared to the reference sample, the relative binding energies increase more for layers closer to the surface of the sample (i.e. a stronger shift of the core level binding energy is observed for Al_2O_3 and SiO_2 than for Si). These results indicate a strong surface band bending in the PA modified sample. Annealing of the PA layer only has a minor influence on the observed band bending. B: XPS core level spectra for Si 2p and Al 2p for p-Si/Al_2O_3 reference sample (bottom) and p-Si/Al_2O_3/PA sample before (middle) and after annealing and rinsing with ethanol (top). Adapted with permission from ref 73.

In a buried junction PEC cell, the photovoltage is formed between the photoabsorber and its heterojunction partner. According to our hypothesis, the anchor layer/PA stack in between p- and n-type heterojunction partner alters the band alignment and therefore the photovoltage. For p-Si/TiO_2 this allowed us to increase the photovoltage by 200 mV. In analogy to this finding, we expected to *decrease* the photovoltage of a *n*-Si/TiO_2 photo*anode* also by 200 mV because in this case, the band shift is in the unfavored direction (same as for n-type WO_3 in the first part). The band diagrams of this blank and PA modified n-Si/TiO_2 stack are presented in Figure 55 making evident that a shift in the same direction would in this system worsen the band alignment and therefore the obtainable photovoltage.

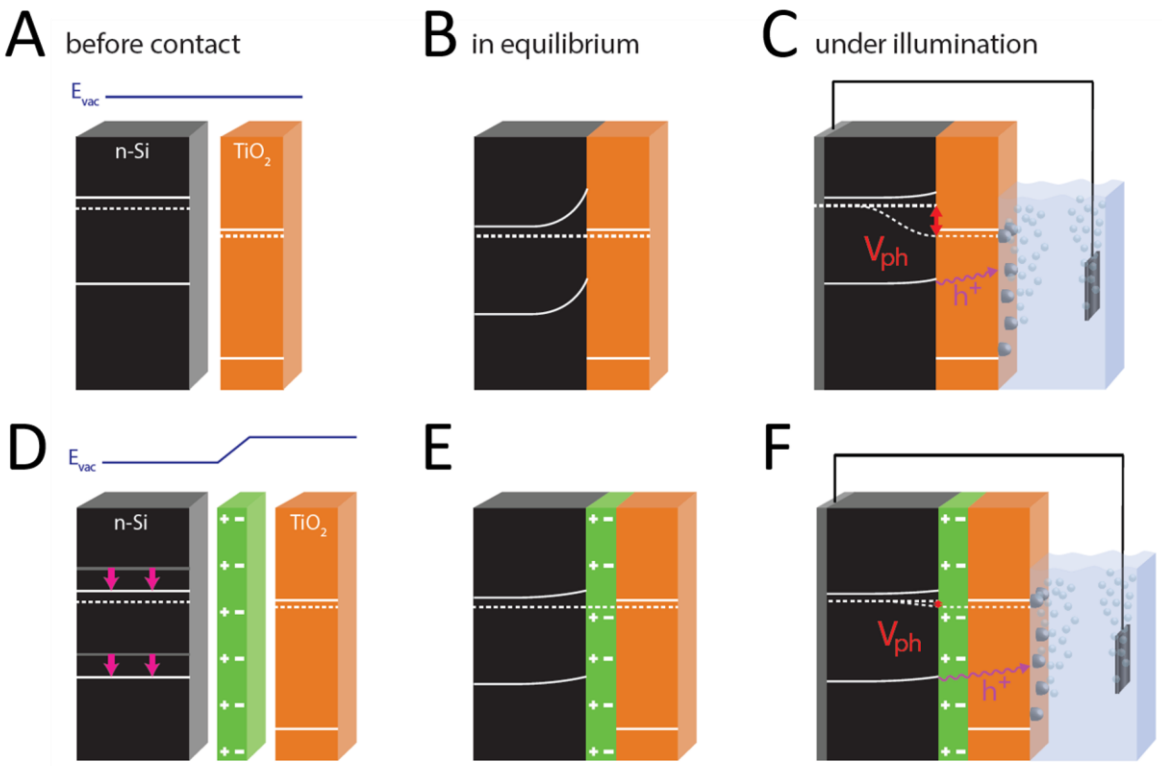

Figure 55. Band structure of n-Si/TiO_2 (A-C) and n-Si/PA/TiO_2 (D-E) before contact (or under flat band condition), in equilibrium in the dark, and under illumination. Adapted with permission from ref 73.

On the other hand, the situation is completely different if pn-Si/TiO_2 is modified with a PA layer. In that case, the photovoltage is generated inside the pn-Si homojunction and not at the Si/TiO_2 junction. Therefore, a dipole layer introduced in between pn-Si and TiO_2 was not expected to change the photovoltage of the device (Figure 56).

Our assumptions were confirmed by the experimental results show in Figure 57. The Ni redox pair as well as the V_{onset} of water oxidation are both shifted by 200 mV in positive direction upon introduction of a PA dipole layer into a n-Si/TiO_2 device. The V_{onset} of the pn-Si/TiO_2 device is equal for blank and dipole modified samples (Figure 57B). There is, however, a small increase in FF in the dipole sample. The band diagrams in Figure 56 gave us a hint to explain this finding. In blank pn-Si/TiO_2, an unfavorable barrier is forming between the n-Si and the protecting TiO_2. This barrier is usually assumed to be very thin due to the high doping densities of both n-Si and TiO_2 in this case. Nevertheless, as drawn in Figure 56, the band offset between n-Si and n-TiO_2 is smaller when a dipole layer moves the n-Si band down and therefore closer to the TiO_2 bands. The smaller barrier (pink circles in Figure 56B, D) in the case of the dipole modified sample might explain its slightly improved FF in the J-V curve.

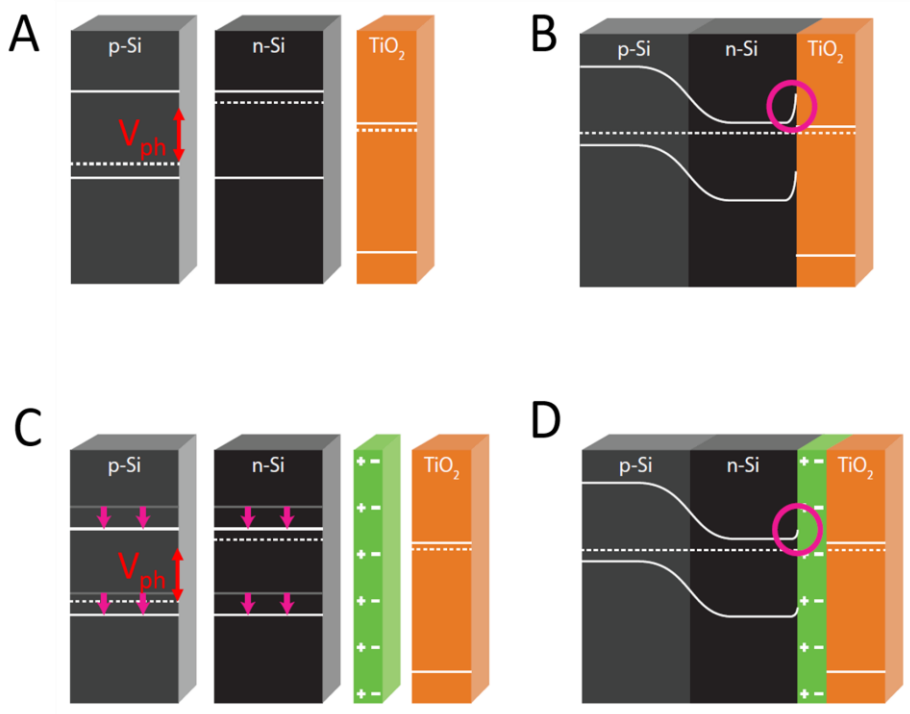

Figure 56. Band diagrams for pn-Si/TiO_2 before contact (A) and in equilibrium (B) and for pn-Si/PA/TiO_2 before contact (C) and in equilibrium (D). Note that the photovoltage (red arrow) is generated within the Si homojunction and its magnitude is not affected by a dipole layer placed outside the homojunction. Adapted with permission from ref 73.

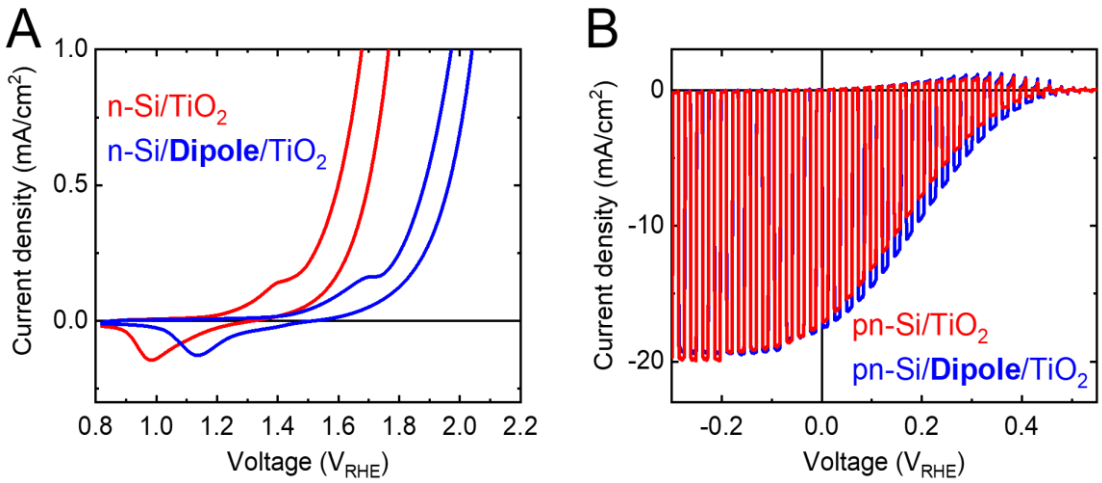

Figure 57. A: Current-Voltage plot of n-Si/TiO_2/Ni (red) and n-Si/anchor layer TiO_2/PA dipole/TiO_2/Ni (blue). Cyclic voltamograms recorded in 1 M KOH electrolyte under 1 sun illumination at 10 mV s^{-1} scan speed. The redox pair before the water oxidation onset shows reduction/oxidation of the Ni catalyst. Both, Ni redox peaks and water oxidation onset, are shifted by 200 mV to more positive voltages, indicating a smaller photovoltage upon PA modification of the heterojunction. B: Linear sweep voltametry of homojunction pn-Si/TiO_2 (red) and pn-Si/PA/TiO_2 (blue), recorded in 1M H_2SO_4 at a scan speed of 10 mV s^{-1} under chopped illumination. Adapted with permission from ref 73.

We already found during the work on WO_3 modification that the V_{onset} shift, and therefore the band shift, correlates with the gas phase dipole moment of the phosphonic acid derivative used to modify the WO_3 surface (Figure 30), but the direction of the band shift (and therefore its main contribution) is set by the increased electron withdrawing effect as compared to the unmodified (OH terminated) WO_3 surface. A similar experiment was performed with p-Si/Al_2O_3 substrate, which was modified by spin coating different phosphonic acid derivates and then protected with TiO_2. J-V curves of blank samples (p-Si/TiO_2) as well as dipole modified devices (p-Si/Al_2O_3/phosphonic acid/TiO_2) and the different phosphonic acids used are displayed in Figure 58. Obviously, all different phosphonic acids result in an early V_{onset} as compared to the blank. This finding matches well with the observation that all phosphonic acids tested led to a positive E_{fb} shift on WO_3 and further corroborates our hypothesis. A correlation between gas phase dipole moment of the phosphonic acids and the V_{onset} shift was not observed. For example, we would expect the strongest V_{onset} shift for FPA and the weakest shift for HBPA, where in fact, FPA resulted in the weakest, and HBPA in one of the strongest shifts. PA, with a modest dipole moment, gave the strongest V_{onset} shift. This points to the fact that besides the gas phase dipole moment, other effects influence the total dipole in the device which then determines the V_{onset} shift. Firstly, and this is also a result of the DFT calculations above, thickness of the phosphonic acid layer plays a very important role. We used phosphonic acid solutions of the same concentration (10 mM) for all devices shown in Figure 58, which resulted in different layer thicknesses for the various phosphonic acids. It's also not clear if one had to use the same layer thickness or the same number of phosphonic acid monolayers (which could be very different due to their different molecular size) in order to guarantee a "fair" comparison between the phosphonic acids. We decided not to further optimize the deposition conditions individually for all phosphonic acids, since under the same deposition conditions, PA performed much better than all of its derivatives.

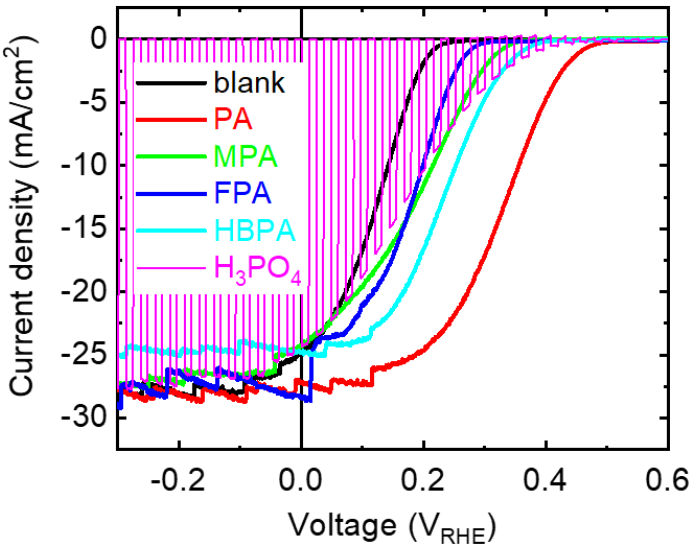

Name	Structure	DFT structure	Dipole direction	Dipole along Z direction
Phosphonic acid **PA**	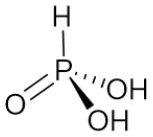	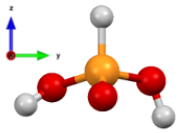		-0.3 D
Methylphosphonic acid **MPA**	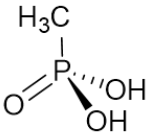	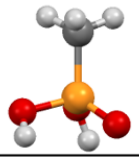		+0.6 D
Fluorophosphonic acid **FPA**	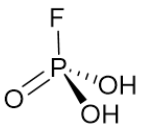	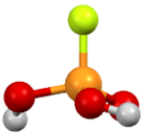		-1.1 D
Hydroxybenzyl phosphonic acid **HBPA**	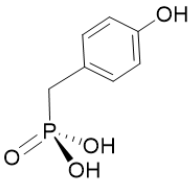	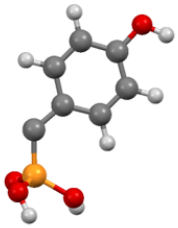		+4.8 D
Phosphoric acid **H_3PO_4**	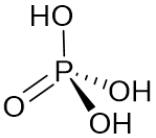	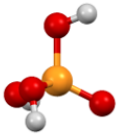		0.0 D

Figure 58. Top: J-V plots of devices with the general structure p-Si/anchor layer/dipole layer/TiO_2/Pt (blank) with different phosphonic or phosphoric acids acting as dipole layers recorded in 1 M H_2SO_4 under 1 sun illumination or chopped illumination (for H_3PO_4, pink). Bottom: Comparison of the structures of the phosphonic acid structures and their calculated gas phase dipole moment along the vertical z-axis (i.e. along the P-R bond) calculated from DFT relaxed structures with the direction and magnitude of the gas phase dipole moment. Reprinted with permission from ref 73.

3.5 Conclusion

The focus of this second part was on p-Si/TiO_2 photocathodes that were modified with an anchor layer on the p-Si onto which a PA layer was deposited to give devices with increased photovoltages.

Firstly, we showed that modification of TiO_2 with PA results in large (300 mV) E_{fb} shifts, which also affirmed our findings on phosphonic acid modified WO_3 from the previous part.

We chose to not directly deposit PA onto p-Si substrate, but to use an anchor layer. This thin layer with known binding to PA would at a later stage facilitate the usage of different photoabsorbing substrates.

Secondly, by using p-Si, 1 nm TiO_2 as anchor layer, a PA layer deposited by spin coating and a 50 nm TiO_2 layer as heterojunction partner and protection layer, we fabricated the first proof-of-principle device that actually showed an improved photovoltage by 200 mV.

Thirdly, we had to overcome some serious reproducibility issues related to PA nano- or microparticle formation by Ostwald-ripening. Careful optimization of the spin coating conditions using lower PA concentrations and the replacement of the TiO_2 anchor layer by Al_2O_3 allowed us to obtain large band shifts without increased series resistance and unpredictable nanoparticle formation.

Fourthly, by using either Pt catalyst or AZO/Ni front contact, we proved that our method is applicable to PEC as well as PV cells and equally increases the V_{onset} or V_{oc} of both devices.

Fifthly, we showed that the band shift can be gradually increased by using different PA concentrations in the spin coating step. We were able to tune V_{onset} over a range of 400 mV.

Sixthly, stability measurements of both, PEC and PV, confirmed that the PA layer is stable and not the limiting factor when the devices fail after hours in PEC. PV cells lost some performance in the first hours of operation and stabilized afterwards with no signs of further degradation after 6 days of heat-light-soaking.

Seventhly, we characterized the composition and morphology of the PA layer by XPS, ESI-MS, SEM, EDX and AFM and found that annealing does not alter the PA composition and the PA layers are thin, flat and homogeneous.

Lastly, DFT calculations confirmed our experimental findings of a PA thickness dependent band shift. According to our explanation, the band shift arises from a dipole formed as OH groups on the anchor layer surface are replaced by less electron donating phosphonate groups. This explains the band shift increase from sub-monolayer up to a full monolayer. For thicker PA films, we claim that the thick (1-2 nm) PA network induces some restructuring of the anchor layer/ PA interface, which decreases the electron donation into the substrate even more.

More experiments were employed to confirm this hypothesis, namely we fabricated dipole modified devices from n-Si (decreased photovoltage) and pn-Si (photovoltage not affected) and measured XPS to track the band bending changes upon PA modification. p-Si/TiO_2 devices fabricated with various phosphonic acid derivatives all showed an increased V_{onset} since the gas phase dipole moment of the phosphonic acid only plays a minor role for the observed dipole in the device and the replacement of OH by phosphonate is the crucial factor.

In the next chapter, we want to employ the knowledge gained from this model system p-Si/TiO_2 to emerging thin film materials like Cu_2O and Sb_2Se_3.

4 Part 3: Improvement of emerging thin film devices

After we had shown that a PA layer induces a dipole and increases the photovoltage of our model photosystem p-Si/n-TiO_2, we wanted to apply the same method to emerging thin film materials studied in our group. At first, we tried to use the very same conditions for anchor and PA layer deposition than for the p-Si system, but soon we realized that the process has to be optimized to some degree for the different photoabsorbers. This chapter describes our efforts to implement the dipole method to emerging materials Sb_2Se_3 and Cu_2O.

4.1 Sb_2Se_3/TiO_2 photocathode

The efficiencies for Sb_2Se_3 PV cells have rapidly increased in recent years. The record efficiency is now 9.2%, set by Li et al.[88] In contrast to that, PEC efficiencies are still very low. Some research groups, including our own, have reported high photocurrents at 0 V_{RHE}, but the efficiency is still limited by poor photovoltages.[89–91] Our group recently reported that selenization of Sb metal gives Sb_2Se_3, which was then decorated with MoS_x catalyst to give stable devices with 16 mA/cm^2 of photocurrent at 0 V_{RHE}.[92] For this project, we used the same Sb_2Se_3 synthesis process, deposited 1 nm of TiO_2 as anchor layer and spin coated PA before the protective TiO_2 layer was deposited by ALD. Figure 59A shows the J-V curves of the blank and dipole modified sample, with the latter showing an increased photovoltage by 40 mV.

The V_{onset} shift might appear small as compared to the shifts obtained in the p-Si system (and we will come to the reasons for the smaller shift later), but the effect on the energy conversion efficiency is quite substantial, as depicted in Figure 59B. Upon PA modification, the efficiency increased from 0.80% to 1.04%, which was the first time a Sb_2Se_3 photocathode reached an efficiency over 1%.

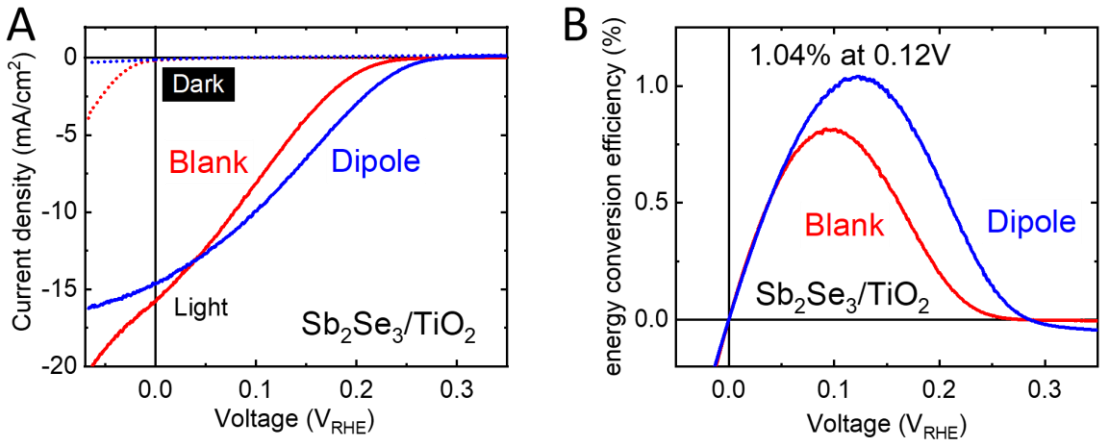

Figure 59. A: Current density-Voltage plots of Sb_2Se_3/TiO_2 (red) and Sb_2Se_3/TiO_2/PA/TiO_2 (blue). Linear sweeps were recorded in 1 M H_2SO_4 at a scan speed of 10 mV/s in the dark (dotted) and under 1 sun illumination (solid). B: Energy conversion efficiency of the same devices. Adapted with permission from ref 73.

4.2 Cu_2O/TiO_2 photocathode

Cuprous oxide (Cu_2O) is another promising semiconductor material extensively studied in our group.[49,75,93,94] Cu_2O quickly corrodes in contact with an electrolyte. It was only when researchers started to report successful protecting strategies for Cu_2O that involve ALD deposited TiO_2 layers that interest in this material started to rise in 2011.[95] All high-voltage Cu_2O PEC cells involve a so-called buffer layer, for example Ga_2O_3.[93] In those cases, the buffer layer serves as the heterojunction partner for Cu_2O, while a TiO_2 layer deposited on top of the buffer layer protects the device. For our study, we wanted to keep the system simple and omitted the buffer layer, so that the TiO_2 serves as heterojunction partner and protective layer, just like in the p-Si/TiO_2 cases described previously. The band alignment of Cu_2O/TiO_2 is not optimal and the photovoltages obtained from this junction are typically 400 – 500 mV (red traces in Figure 60). We deposited a 1 nm TiO_2 anchor layer on top of electrodeposited Cu_2O samples and spin coated PA on top of the TiO_2. The stack was then protected with 50 or 100 nm of TiO_2 and Pt was sputtered as catalyst. Figure 60 shows two examples where this procedure increased the photovoltage of the device by 70 mV and 110 mV, respectively.

We want to note that the dipole induced V_{onset} shift was on one hand smaller than for the p-Si/TiO_2 system and on the other hand not fully reproducible, meaning that for some fabrication series, the PA modified samples did not show any V_{onset} shift. We attribute this to parasitic surface states, the density of which strongly depends on small experimental details, which are very hard to identify and therefore influence. We identified the role of those surface states induced most likely by Cu^{2+} species on the

Cu_2O surface in another study conducted in our group and found that etching treatments can diminish some of the surface states, but not completely.[94]

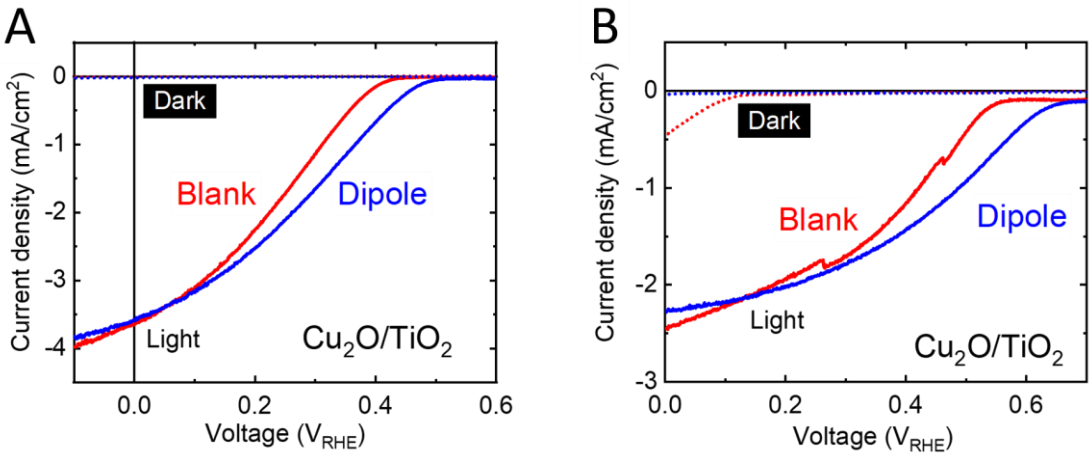

Figure 60. Current-Voltage plots of Cu_2O/TiO_2 (red) and Cu_2O/TiO_2/PA/TiO_2 (blue). Linear sweeps were recorded in 1 M phosphate solution at pH 7 at a scan rate of 10 mV/s in the dark (dotted) and under 1 sun illumination (solid). A and B are samples from two different batches. A was adapted with permission from ref 73.

4.3 Unsuccessful materials

Our early assumption was that the use of an anchor layer, onto which the PA is deposited, would allow a fast and easy application of the dipole strategy to emerging thin film photoabsorber systems. We quickly noticed that this assumption was a bit naïve and the deposition of the anchor as well as the PA layer require some optimization for each substrate material. Furthermore, on some substrates the anchor layer/PA stack did not lead to a V_{onset} increase at all. This was the case for InP/TiO_2 (4 batches with 8 modified samples tested) and Sb_2S_3/TiO_2 (2 batches with 4 samples) heterojunctions and we attribute it to the presence of surface states in those materials. Surfaces states with a certain energy can lead to fermi level pinning[96–99] in a material and, if this is the case, the photovoltage is no longer set by the difference in fermi level between p- and n- type heterojunction partner, but by the energy difference of the materials fermi level and its surface states (Figure 61). The consequences can be observed if different heterojunction partner materials always lead to the same photovoltage for a certain photoabsorber. And, similarly, surface states might be the reason, if a dipole layer is added but the photovoltage does not change. This behavior was observed for our experiments on InP/TiO_2 and Sb_2S_3/TiO_2. Another explanation would be that the dipole layer was not deposited at all (or partially), but we excluded this as we could measure the thickness of the anchor layer as well as the PA layer by ellipsometry and the very same deposition techniques were used as for the successful tests on p-Si,

Cu_2O and Sb_2Se_3. A third reason might be that the anchor layer as well as the PA are deposited correctly, but for whatever reason do not form a dipole on some substrates. Certainly, this last explanation strongly contradicts our assumptions on the origin of the dipole (replacement of OH groups by less electron donating phosphonate groups), and so we disfavor this explanation.

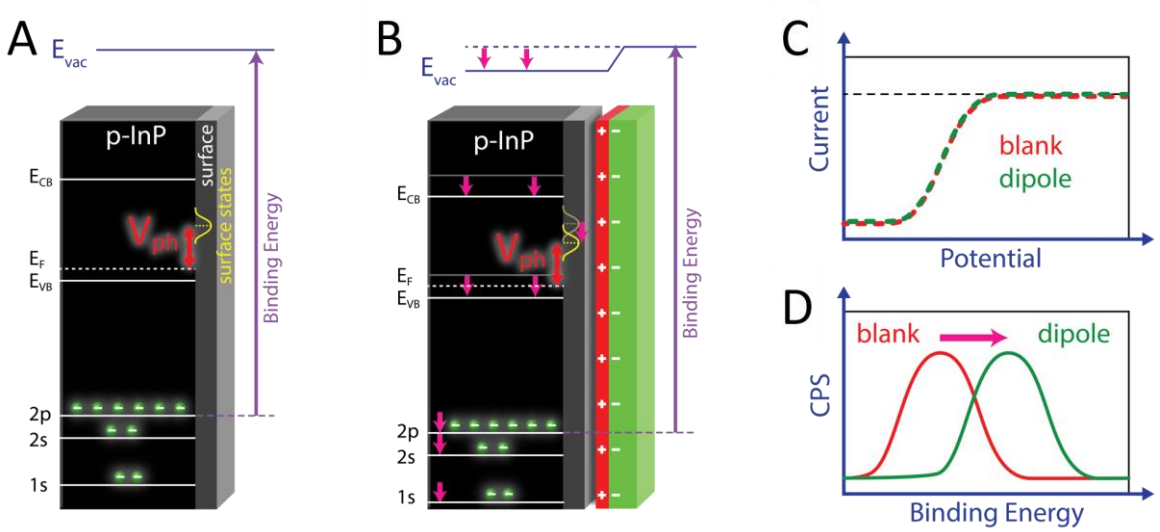

Figure 61. A: Qualitative sketch of the band positions of p-InP with surface states in the middle of the band gap, resulting in a limited V_{ph}. The difference between the energy level of the core electrons and E_{vac} is the binding energy and can be measured by XPS. B: A dipole consisting of anchor layer and PA were added resulting in a step in E_{vac} and shifting of all the band positions including core electrons. C: Hypothetical J-V curves of the devices depicted in A and B. The dipole in B has no influence on V_{ph} and the J-V curves overlap. D: Hypothetical XPS measurement revealing the increased core electron binding energy as an effect of the dipole (CPS stands for counts per second).

Two experimental findings would prove the surface state theory (which is the most likely theory in our opinion): Firstly, if surface states hinder the dipole layer from affecting V_{onset}, getting rid of them by some etching or surface passivation technique before depositing the anchor and PA layer would circumvent the problem. The effect of surface etching or passivation treatments could be monitored by photoluminescence measurements. Surface states usually act as recombination centers, therefore quenching the luminescence of a material. A successful surface treatment would lead to an increased photoluminescence and we would expect that the photovoltage can be tuned by dipoles as soon as the concentration of surface states is low enough.

Secondly, we expect that a dipole deposited onto a material with surface states shifts the bands of the material and the energetic position of the surface states by the same amount. For exactly that same reason, the photovoltage would not be affected by the presence of the dipole (Figure 61A-C). The absolute position of the bands could then be determined by either measuring the core level binding

energies of the substrate atoms (Figure 61D) or the work function of the material by Kelvin Probe measurements.

4.4 Conclusion

We successfully showed that the dipole method developed on p-Si substrates can be transferred to other materials. V_{onset} shifts of 110 mV and 40 mV were demonstrated for Cu_2O/TiO_2 and Sb_2Se_3/TiO_2, respectively. However, the V_{onset} shifts were substantially smaller than the ones observed on Si devices and for some batches, no shift was observe at all. For InP/TiO_2 and Sb_2S_3/TiO_2, we never measured a positive V_{onset} shift. We attribute this to the presence of surface states within the band gap, leading to fermi level pinning and therefore a fixed photovoltage that cannot be influenced by a dipole.

5 Work in Progress and Outlook

Currently, we are testing different surface etching and passivation techniques and trying to find a correlation between surface state concentration (accessed by photoluminescence measurements) and whether the dipole layer increases the photovoltage (J-V curves). Furthermore, detailed XPS measurement should reveal an increased binding energy of the core level electron when the dipole is added, even if this is not manifested as an increased photovoltage. The XPS results would be backed up with Kelvin Probe measurements ideally showing the same effect on the work function of the substrate (see Figure 61).

Furthermore, we are modifying photoabsorbing substrates in order to find more modifications that act as dipoles and give larger shifts than PA or even shift the bands in the other direction. This modification would then be used to increase the photovoltage in n-type photoabsorbers. Preliminary results have shown that fluoride modification of p-Si substrates with thin Al_2O_3 or TiO_2 anchor layer leads to photovoltage increases similar to PA. The reason for this behavior is in analogy to the PA method: OH groups on the anchor layer metal oxide are replaced with less electron donating F groups. Along the same line, we found that chloride, bromide and iodide modifications all lead to an increase in photovoltage of p-Si/anchor layer/halide/TiO_2 devices.

Now we have many different surface modifications (PA, different phosphonic acids and benzylic acids, halides) leading to band shifts with different magnitudes (although all in the same direction). Furthermore, after some testing we can get reliable photoluminescence results as well as work function values from our new AFM machine equipped with Kelvin Probe. With those tools combined, we are optimistic that we can soon explain why sometimes the presence of a dipole in the pn-heterojunction does not change the photovoltage and in a next step propose countermeasures to shift the bands of all substrates.

6 Experimental

Parts of this chapter are extracted from our publication.[73]

6.1 Sample fabrication WO_3

FTO cleaning. FTO on glass was purchased from Pilkington and cut into the desired dimension prior to cleaning by ultrasonication in acetone, soapy water (Deconex), Millipore water and ethanol for 10 min each. The samples were then stored in ethanol until they were used.

WO_3 spin coating technique was adapted from Wang et al.[59] and Deepa et al.[60] Tungsten powder (>99.9%, Sigma-Aldrich) was suspended in 10 ml water and 10 ml H_2O_2 (35%, Merck) while stirring. The tungsten powder was oxidized to tungstic acid (H_2WO_4) accompanied with H_2 and heat generation. After 5 – 10 min, the tungsten powder was completely dissolved, giving a clear, slightly yellow solution. The excess H_2O_2 was decomposed by immersing a Pt mesh into the solution at elevated temperatures of 50 – 70 °C. The Pt mesh was removed when O_2 formation ceased, typically after 2 – 3 hours. This tungstic acid solution was then stored in the fridge to delay WO_3 particle formation, which typically took place after 24 h at room temperature and after 2 – 3 weeks in the fridge. Tungstic acid solutions were therefore used for no longer than 1 week.

For a typical spin coating experiment, the tungstic acid stock solution was diluted 1:10 with ethanol to improve its wetting abilities. The spin coating was then performed by applying 100 µl of the this solution and spinning at 3000 rpm for 30 s, with an acceleration of 500 rpm/s. The resulting WO_3 film was then dried in air for 30 min, followed by annealing at 500 °C for 1 hour. For thicker films, the spin coating/drying/annealing cycle could be repeated multiple times.

WO_3 doctor blading was performed based on Santato et al.[62] Firstly, a plastic column was filled with 20 ml DOWEX resin (50WX2, 100-100 mesh, Acros Organics) and extensively washed with water. The resin was then protonated by flushing with 50 ml 1 M H_2SO_4, which decreases the volume of the resin by 25%. Na_2WO_4 (1 mmol, 330 mg, 99%, Sigma-Aldrich) was dissolved in 1 ml water and loaded onto the DOWEX column. After the tungstate solution completely infiltrated the DOWEX resin, water was added on top. A pale yellow fraction was collected (2 ml) and diluted with 40 ml ethanol. This solution was concentrated on the RotaVap to 2 ml (0.5 M tungstic acid), yielding a milky pale yellow solution. PEG 300 (462 mg, 412 µl, Sigma-Aldrich) was added while stirring.

For the doctor blading, a cleaned FTO slide was placed on the laboratory bench and taped to it along the left and right side. The roughly 20 µm thick tape serves as a spacer and defines the thickness of the resulting films. Varying amounts of stock solution (10 – 100 µl) were then applied to the top end of the FTO glass and spread over the sample by quickly moving a glass pipette from top to bottom of the sample. The samples were then dried in ambient conditions for 10 – 30 min and then annealed in oxygen at 500 °C for 30 min – 1 h.

WO_3 spraying procedure was adopted from Steier et al.[100] The stock solution was prepared the same way as the doctor blading stock solution by using an ion exchange DOWEX column. The tungstic acid from the DOWEX column (2 ml) was diluted in 8 ml ethanol, yielding a 0.1 M tungstic acid solution. Clean FTO samples were placed on a hot plate heated to 200 °C. Different volumes of the stock solution (1 – 4 ml) were then sprayed onto the sample using a low-tech glass spray device equipped with a rubber ball for manual pumping and spraying. Samples were then annealed at 500 – 550 °C in oxygen flow for 30 min.

WO_3 electrodeposition was performed similar to the procedure reported by the Lewis group.[64,65] Tungsten powder was suspended in 2.5 ml H_2O_2 (30 %, Merck). Water (9.5 ml) was added and the suspension was heated to 70 °C. After 1 min of vigorous gas formation (H_2) and heat release, the solution turns clear as all the tungsten was oxidized to tungstic acid. A Pt mesh was immersed into the solution to decompose the excess of H_2O_2 until gas formation (O_2) ceased and the mesh was removed again. Isopropyl alcohol (50 ml) was added and the solution was filled up with water to a total volume of 100 ml (50 mM tungstic acid).

Electrodeposition was done in a 2 electrode setup. As working electrode, a clean FTO slide was immersed 2 cm into the tungstic acid solution and a Pt wire was used as counter electrode. In chronopotentiometry mode, typically -0.1 mA/cm^2 were applied for 10 min, resulting in a dark blue film. Different current densities and deposition times yielded different thicknesses of the resulting WO_3 film, but too fast depositions yielded inhomogeneous films with lots of cracks and pinholes. The blue film was blown dry in a stream of nitrogen and preannealed on a hotplate at 275 °C for 5 min, resulting in pale yellow films. This electrodeposition/preannealing cycles was repeated up to 5 times, which yielded very thick films, which often flaked off from the FTO substrate quite easily. In the end, the samples were annealed at 500 – 550 °C in oxygen for 30 min.

Phosphonic acid modification. Electrodeposited WO_3 samples were modified with phosphonic acid using the T-BAG method[72] or a simple drop-casting method. At first, the T-BAG method gave good results and after some time, we realized that the same results can be obtained much faster using the drop-casting method. Here, both will be described: For the T-BAG method, a beaker is filled with ethanolic 10 mM solution of the desired phosphonic acid. The substrate WO_3 on FTO is immersed into

this solution. Over the course of hours (12-48 h), the solution evaporates and the phosphonic acid is deposited where the meniscus of the solution migrates slowly over the sample. The sample is removed when the solution level is low enough and not in contact with the sample anymore. The sample is usually covered in a white residue and heated to 140 °C for 3 h before removing the residue by washing with ethanol. For drop casting, the same ethanolic 10 mM phosphonic acid stock solution was dropped (50 µl for 1 cm^2 samples) onto the WO3 sample and the solvent was allowed to evaporate, which took 1-2 minutes and left a white residue, which was washed away with ethanol after annealing at 140 °C for 3 h. In this way, all the phosphonic acids in Figure 28 and Figure 29 (all purchased from Sigma-Aldrich with purities between 97% and 99%) were grafted onto WO_3 substrates.

6.2 Sample fabrication p-Si/TiO_2

Si wafer cleaning and etching. p-Si wafers were bought from Sil'Tronix, France, (Boron doping, 10-30 Ohm·cm, single side polished) and cut into 1x1cm pieces, which were then cleaned by ultrasonicating for 10 min each in acetone, soapy water (Deconex), water and ethanol, followed by 10 min at 50 °C in $H_2O/H_2O_2/NH_4OH$ (5:1:1) solution, 10 min at 50 °C in H_2O/H_2O_2/HCl 5:1:1 solution and 30 s in 2% HF solution at room temperature. Samples were then rinsed with water, dried in a stream of N_2 and immediately used for the next steps.

Anchor layer deposition. All anchor layers were deposited by ALD onto freshly cleaned and etched Si wafer pieces using a Picosun R-200 machine. TiO_2 deposition was carried out at 120 °C using sequential pulses of tetrakis(dimethylamino)titanium (T precursor: 85 °C) and H_2O (T precursor: 25 °C). Ten cycles were used for anchor layer yielding amorphous TiO_2 films with a thickness of 0.5 nm (0.52 Å/cycle), as determined by ellipsometry. Al_2O_3 deposition was done at 120 °C using pulses of trimethylaluminium (T precursor: 25 °C) and H_2O (T precursor: 25 °C). Unless stated otherwise, 5 cycles were deposited yielding Al_2O_3 thicknesses of 0.5 nm. For Ga_2O_3 deposition, a higher temperature of 160 °C was used with pulses of tris(dimethylamido)gallium (T precursor: 150 °C) and H_2O (T precursor: 25 °C). 10 cycles were used to obtain Ga_2O_3 thicknesses of 0.5 nm.

PA spin coating, annealing and rinsing. Solutions of phosphonic acid (**PA**, H_3PO_3, 99%, Sigma-Aldrich) in EtOH were spin coated onto Si wafer pieces at 2000 rpm for 20-30 s with an acceleration of 500 rpm/s. Typically, 0.1 ml of PA solution was used with a concentration of 10 mM, if not stated otherwise. After spin coating, the samples were annealed on a hot plate in air at 120 °C for 10 min, allowed to cool down to ~80 °C on the hot plate (ca. 30 min) and then quickly cooled to room temperature by removing them from the hot plate. The samples were then rinsed under a stream of EtOH for 2-3 s and then dried in a stream of N_2.

Different phosphonic acids. Layers of methylphosphonic acid (MPA, CH_5O_5P, 98%, Sigma-Aldrich), phosphoric acid (H_3PO_4, 99.999%, Sigma-Aldrich), fluorophosphoric acid (FPA, H_2FO_3P, 70 wt% in H_2O, Sigma-Aldrich), hydroxybenzylphosphonic acid (HBPA, $C_7H_9O_4P$, 97%, Sigma-Aldrich) were spin coated from 10 mM ethanolic solutions, annealed and rinsed with the same procedure used for PA.

TiO_2 ALD. ALD of the protective layer was carried out analogously to TiO_2 anchoring layer but using 930 cycles, yielding 50 nm of TiO_2.

Pt sputtering. To finalize the PEC cells, nominally 1 nm of Pt was sputtered using a Safematic CCU-010 device.

AZO/Ni. For PV cells, the front contact was fabricated by sputtering 260 nm of Al:ZnO (2 at% Al, 1.8 W cm^{-2}) and 105 nm of MgF_2. A 4 µm Ni/Al grid was deposited by e-beam evaporation.

6.3 Sample fabrication emerging materials

Sb_2Se_3 fabrication. Sb_2Se_3 thin films were prepared by selenization of electrodeposited Sb as reported elsewhere.[92] Briefly, Sb metal was electrodeposited on Au coated FTO substrates using an electrolyte of antimony potassium tartarate and citric acid with the pH adjusted to 1.3 by addition of concentrated sulfuric acid. After electrodeposition the samples were annealed in a tube furnace at 350 °C in the presence of Se.

Cu_2O fabrication. Electrodeposition substrates were prepared by sputtering 100 nm of Au onto FTO coated glass. Cu_2O was electrodeposited at 30 °C in galvanostatic mode at a current density of -0.1 mA/cm^2 for 100 min using a Keithley source meter. The aqueous copper sulfate solution was prepared with the following initial concentrations: 0.2 M $CuSO_4$ (Sigma-Aldrich, ≥99%), 0.5 M K_2HPO_4 (Sigma-Aldrich, ≥99.5%), 3 M lactic acid (Fisher Scientific, 85%). The pH was adjusted to 12 by adding a large volume of 2 M KOH (Honeywell, extra pure).

6.4 Characterization

SEM-EDX. SEM images were obtained from a Zeiss Supra 50 VP equipped with EDX detector Oxford X-MAX80. An electron beam voltage of 10 kV was used. Images were recorded using the in-lens detector.

Ellipsometry. Thicknesses of PA layers as well as TiO_2, Al_2O_3, Ga_2O_3 layers deposited by ALD were measured using a J.A. Woollam Co. alpha-SE ellipsometer with standard scan speed at 65° and 70°. The layers were modeled with a Si substrate and transparent film on top.

JV, CA (PEC). Electrochemical measurements were conducted in 1 M H_2SO_4 using a Biologic SP-200 potentiostat equipped with impedance module. Pt wire was used as counter electrode and $Hg/HgSO_4$ as reference electrode (+0.634 V vs RHE). Current-Voltage sweeps were recorded at scan velocities of 10 or 20 mV/s, in the dark, under 1 sun illumination (AM 1.5, LOT mercury lamp solar simulator) or under chopped illumination (1 sec chopping). The photoanode n-Si/TiO_2/Ni was measured in 1 M KOH using Ag/AgCl as reference. Chronoamperometric measurements were performed by applying 0 V_{RHE} under 1 sun illumination.

JV, EQE, stability (PV). A Keithley 2400 source meter with four-terminal sensing was used to record J-V curves under standard test conditions (1000 W m^{-2}, 298 K, ABA solar simulator). External quantum efficiency (EQE) spectra were recorded at 298 K using a triple-grating monochromator with a chopped white light source and a lock-in amplifier with 100 W m^{-2} white light bias. Data were referenced to a monocrystalline Si solar cell certified by Fraunhofer ISE. Stability of the PV cells was tested in a heat-light soaking experiment at 80 °C under 1 sun illumination at maximum-power-point in dry N_2 atmosphere. An I-V curve was recorded every 30 min.

Electrochemical Impedance Spectroscopy (EIS). The space charge capacitance (C_{sc}) was obtained from EIS measurements. From C_{sc} in the depletion region the doping density, flat band potential and n- or p-type character of a semiconductor can be obtained using Mott-Schottky analysis. The measurements on PV cells were performed on solar cells using a BioLogic SP-200 potentiostat in two electrode configuration in the dark and light with frequencies from 1 MHz to 0.1 Hz with potential steps of 25 or 50 mV with a waiting time of 10 s after each potential step. FTO/TiO_2/PA samples were measured in PEC mode with three electrode configuration in 1 M H_2SO_4 (pH 0) or 1 M Na_2SO_4 (pH 2) with mercury sulfate reference electrode in the dark. A frequency range from 200 kHz to 0.1 Hz and potential steps of 25 mV or 33 mV were used. For both cases (PV and PEC) a voltage perturbation of 10 mV was applied. The data were fitted with ZView software. A constant phase element (CPE) was used to model the space charge capacitance and the CPE was then converted to C_{sc} using this equation:

$$C_{sc} = \frac{(R_{ct} \times Q)^{(\frac{1}{n})}}{R_{ct}}$$

with R_{ct} being the charge transfer resistance, Q the charge from the CPE and n as the CPE exponent. The flat band potential (E_{fb}) and doping density (N_A) were obtained by plotting $1/C_{sc}^2$ versus the applied

potential, giving E_{fb} as the x-axis intercept and the doping density as the slope according to the Mott-Schottky equation:

$$\frac{1}{C_{sc}^2} = \frac{2}{N_A A^2 \varepsilon \varepsilon_0 q}(E - E_{fb} - \frac{kT}{q})$$

with q as the electron charge, ε as the dielectric constant of the material, ε_0 as permittivity of free space, and N_A as acceptor density (for p-type materials, N_D for n-type semiconductors), E is the applied potential, k is the Boltzmann constant, A is the area and T is the temperature.

Atomic force microscopy (AFM, VEECO E-Scope) was performed to retrieve information about the surface topography of the sample. The measurement was performed in tapping mode using a Pt–Ir metal coated tip with a nominal spring constant k = 2.8 N m^{-1} and a resonance frequency of 100 kHz.

X-ray photoelectron spectroscopy (XPS) was conducted using a Physical Electronics (PHI) Quantum 2000 spectrometer featuring monochromatic Al-Kα radiation, generated from an electron beam operated at 15 kV and 35.8 W. The energy scale of the instrument was calibrated using Au and Cu reference samples. The analysis was conducted at 2 E^{-9} mbar, with an electron take off angle of 45° and a pass-energy of 23.5 eV for all samples. The measurements were conducted without charge neutralization. Spectra of select samples were fitted using Voigt profiles (GL30) after Shirley background subtraction. A doublet splitting of ΔE = 0.63 eV was used for the Si 2p core level emission, whereas a single Voigt profile was used to fit the Al 2p.

Electrospray-ionisation mass spectroscopy (ESI-MS). High-resolution mass spectra were acquired on a QExactive instrument (ThermoFisher Scientific) equipped with a heated electrospray ionization source. PA was spin coated onto p-Si/Al_2O_3, annealed and then rinsed with EtOH and dried in N_2 stream. The sample was then ultrasonicated in 1 ml of 1 mM NaOH to remove the compounds bound to the Si surface, and the obtained solution was analyzed by HR-ESI-MS.

References

1. OECD. Primary energy supply (indicator). (2018). doi:10.1787/1b33c15a-en

2. United Nations. *World Population Prospects: The 2017 Revision, Key Findings and Advance Tables*. (2017).

3. The World Bank. *Poverty and Shared Prosperity 2018 Piecing Together the Poverty Puzzle*. (2018).

4. International Energy Agengy. *Key World Energy Statistics 2017*. (OECD, 2018).

5. Mcglade, C. & Ekins, P. The geographical distribution of fossil fuels unused when limiting global warming to 2 °C. *Nature* **517**, 187–190 (2015).

6. Cook, J. *et al.* Consensus on consensus: a synthesis of consensus estimates on human-caused global warming. *Environ. Res. Lett.* **11**, 048002 (2016).

7. Tol, R. S. J. Comment on 'Quantifying the consensus on anthropogenic global warming in the scientific literature'. *Environ. Res. Lett.* **11**, 048001 (2016).

8. Huber, M. & Knutti, R. Anthropogenic and natural warming inferred from changes in Earth's energy balance. *Nat. Geosci.* **5**, 31–36 (2012).

9. SCRIPPS Institution of Oceanography. Keeling Curve. Available at: https://scripps.ucsd.edu/programs/keelingcurve/. (Accessed: 8th June 2019)

10. Lüthi, D. *et al.* High-resolution carbon dioxide concentration record 650,000-800,000 years before present. *Nature* **453**, 379–382 (2008).

11. MacFarling Meure, C. *et al.* Law Dome CO_2, CH_4 and N_2O ice core records extended to 2000 years BP. *Geophys. Res. Lett.* **33**, L14810 (2006).

12. Abbott, D. Keeping the Energy Debate Clean: How Do We Supply the World's Energy Needs? *Proc. IEEE* **98**, 42–66 (2010).

13. Sathre, R. *et al.* Life-cycle net energy assessment of large-scale hydrogen production via photoelectrochemical water splitting. *Energy Environ. Sci.* **7**, 3264–3278 (2014).

14. Fischer, F. & Tropsch, H. Über die direkte Synthese von Erdöl-Kohlenwasserstoffen bei gewöhnlichem Druck. (Erste Mitteilung). *Berichte der Dtsch. Chem. Gesellschaft (A B Ser.* **59**, 830–831 (1926).

15. Haber, F. & R., L. R. Zeitschrift Fur Elektrochemie. **19**, 53 (1913).

16. Mertens, K. *Photovoltaik - Lehrbuch zu Grundlagen, Technologie und Praxis*. (Hanser Verlag, 2018).

17. Barton, E. E., Rampulla, D. M. & Bocarsly, A. B. Selective Solar-Driven Reduction of CO 2 to Methanol Using a Catalyzed p-GaP Based Photoelectrochemical Cell. *J. Am. Chem. Soc.* **130**, 6342–6344 (2008).

18. Schreier, M. *et al.* Efficient and selective carbon dioxide reduction on low cost protected Cu 2 O photocathodes using a molecular catalyst. *Energy Environ. Sci.* **8**, 855–861 (2015).

19. Li, T. *et al.* Photoelectrochemical oxidation of organic substrates in organic media. *Nat. Commun.* **8**, 390 (2017).

20. Cha, H. G. & Choi, K.-S. Combined biomass valorization and hydrogen production in a photoelectrochemical cell. *Nat. Chem.* **7**, 328–333 (2015).

21. Anderson, R. L. Germanium-gallium arsenide heterojunctions. *IBM J. Res. Dev.* **4**, 283–287 (1960).

22. Fritsche, J., Klein, A. & Jaegermann, W. Thin Film Solar Cells: Materials Science at Interfaces. *Adv. Eng. Mater.* **7**, 914–920 (2005).

23. Chuang, C.-H. M., Brown, P. R., Bulović, V. & Bawendi, M. G. Improved performance and stability in quantum dot solar cells through band alignment engineering. *Nat. Mater.* **13**, 796–801 (2014).

24. Shaheen, S. E. *et al.* Band-Offset Engineering for Enhanced Open-Circuit Voltage in Polymer–Oxide Hybrid Solar Cells. *Adv. Funct. Mater.* **17**, 264–269 (2006).

25. Siol, S. *et al.* Band Alignment Engineering at Cu2O/ZnO Heterointerfaces. *ACS Appl. Mater. Interfaces* **8**, 21824–21831 (2016).

26. Cahen, D. & Kahn, A. Electron energetics at surfaces and interfaces: Concepts and experiments. *Adv. Mater.* **15**, 271–277 (2003).

27. Jägermann, W. The Semiconductor/Electrolyte Interface: A Surface Science Approach. *Mod. Asp. Eectrochemistry* **30**, 1–186 (1996).

28. Kim, S. H., Ahn, S. J. & Kim, K. Vibrational Spectroscopic Study of 4-Cyanobenzoic Acid Adsorbed on Silver. 7174–7180 (2001). doi:10.1021/jp953309r

29. Choi, H., Kim, H.-B., Ko, S.-J., Kim, J. Y. & Heeger, A. J. An Organic Surface Modifier to Produce a High Work Function Transparent Electrode for High Performance Polymer Solar Cells. *Adv. Mater.* **27**, 892–896 (2015).

30. Lange, I. *et al.* Tuning the work function of polar zinc oxide surfaces using modified phosphonic acid self-assembled monolayers. *Adv. Funct. Mater.* **24**, 7014–7024 (2014).

31. Guerrero, G., Alauzun, J. G., Granier, M., Laurencin, D. & Mutin, P. H. Phosphonate coupling molecules for the control of surface/interface properties and the synthesis of nanomaterials. *Dalt. Trans.* **42**, 12569–12585 (2013).

32. Kovalchuk, A. *et al.* Dipole-induced asymmetric conduction in tunneling junctions comprising self-assembled monolayers. *Rsc Adv.* **6**, 69479–69483 (2016).

33. Gärtner, M. *et al.* Understanding the Properties of Tailor-Made Self-Assembled Monolayers with Embedded Dipole Moments for Interface Engineering. *J. Phys. Chem. C* **122**, 28757–28774 (2018).

34. Kraack, J. P., Lotti, D. & Hamm, P. 2D attenuated total reflectance infrared spectroscopy reveals ultrafast vibrational dynamics of organic monolayers at metal-liquid interfaces. *J. Chem. Phys.* **142**, 212413 (2015).

35. Goh, C., Scully, S. R. & McGehee, M. D. Effects of molecular interface modification in hybrid organic-inorganic photovoltaic cells. *J. Appl. Phys.* **101**, 1–12 (2007).

36. Khodabakhsh, S. *et al.* Using self-assembling dipole molecules to improve charge collection in molecular solar cells. *Adv. Funct. Mater.* **16**, 95–100 (2006).

37. Kim, J. S. *et al.* Control of the electrode work function and active layer morphology via surface modification of indium tin oxide for high efficiency organic photovoltaics. *Appl. Phys. Lett.* **91**, 1–4 (2007).

38. Ma, H., Yip, H.-L., Huang, F. & Jen, A. K.-Y. Interface Engineering for Organic Electronics. *Adv. Funct. Mater.* **20**, 1371–1388 (2010).

39. Zuo, L. *et al.* Enhanced Photovoltaic Performance of $CH_3NH_3PbI_3$ Perovskite Solar Cells through Interfacial Engineering Using Self-Assembling Monolayer. *J. Am. Chem. Soc.* **137**, 2674–2679 (2015).

40. Shih, Y. C., Wang, L. Y., Hsieh, H. C. & Lin, K. F. Enhancing the photocurrent of perovskite solar cells via modification of the TiO 2 /CH 3 NH 3 PbI 3 heterojunction interface with amino acid. *J. Mater. Chem. A* **3**, 9133–9136 (2015).

41. Kim, G. H. *et al.* High-Efficiency Colloidal Quantum Dot Photovoltaics via Robust Self-Assembled Monolayers. *Nano Lett.* **15**, 7691–7696 (2015).

42. Azmi, R. *et al.* Low-Temperature-Processed 9% Colloidal Quantum Dot Photovoltaic Devices through Interfacial Management of p-n Heterojunction. *Adv. Energy Mater.* **6**, 1–10 (2016).

43. Azmi, R. *et al.* Improved performance of colloidal quantum dot solar cells using high-electric-dipole self-assembled layers. *Nano Energy* **39**, 355–362 (2017).

44. Koldemir, U. *et al.* Molecular Design for Tuning Work Functions of Transparent Conducting Electrodes. *J. Phys. Chem. Lett.* **6**, 2269–2276 (2015).

45. MacLeod, B. A. *et al.* Phosphonic Acid Modification of GaInP 2 Photocathodes Toward Unbiased Photoelectrochemical Water Splitting. *ACS Appl. Mater. Interfaces* **7**, 11346–11350 (2015).

46. Smith, W. A., Sharp, I. D., Strandwitz, N. C. & Bisquert, J. Interfacial band-edge energetics for solar fuels production. *Energy Environ. Sci.* **8**, 2851–2862 (2015).

47. Rivest, J. B., Li, G., Sharp, I. D., Neaton, J. B. & Milliron, D. J. Phosphonic Acid Adsorbates Tune the Surface Potential of TiO 2 in Gas and Liquid Environments. *J. Phys. Chem. Lett.* **5**, 2450–2454 (2014).

48. Bae, D., Seger, B., Vesborg, P. C. K., Hansen, O. & Chorkendorff, I. Strategies for stable water splitting via protected photoelectrodes. *Chem. Soc. Rev.* **46**, 1933–1954 (2017).

49. Niu, W. *et al.* Extended Light Harvesting with Dual Cu 2 O-Based Photocathodes for High Efficiency Water Splitting. *Adv. Energy Mater.* **8**, 1702323 (2018).

50. Moehl, T., Suh, J., Sévery, L., Wick-Joliat, R. & Tilley, S. D. Investigation of (Leaky) ALD TiO 2 Protection Layers for Water-Splitting Photoelectrodes. *ACS Appl. Mater. Interfaces* **9**, 43614–43622 (2017).

51. Septina, W., Prabhakar, R. R., Wick, R., Moehl, T. & Tilley, S. D. Stabilized Solar Hydrogen Production with CuO/CdS Heterojunction Thin Film Photocathodes. *Chem. Mater.* **29**, 1735–1743 (2017).

52. Cox, C. R., Winkler, M. T., Pijpers, J. J. H., Buonassisi, T. & Nocera, D. G. Interfaces between water splitting catalysts and buried silicon junctions. *Energy Environ. Sci.* **6**, 532–538 (2013).

53. Scheuermann, A. G. *et al.* Design principles for maximizing photovoltage in metal-oxide-protected water-splitting photoanodes. *Nat. Mater.* **15**, 99–105 (2016).

54. Dai, P. *et al.* Forming Buried Junctions to Enhance the Photovoltage Generated by Cuprous Oxide in Aqueous Solutions. *Angew. Chemie Int. Ed.* **53**, 13493–13497 (2014).

55. Seo, J., Kim, H. J., Pekarek, R. T. & Rose, M. J. Hybrid Organic/Inorganic Band-Edge Modulation of *p* -Si(111) Photoelectrodes: Effects of R, Metal Oxide, and Pt on H_2 Generation. *J. Am. Chem. Soc.* **137**, 3173–3176 (2015).

56. Li, S., Zhang, P., Song, X. & Gao, L. Photoelectrochemical Hydrogen Production of TiO_2 Passivated Pt/Si-Nanowire Composite Photocathode. *ACS Appl. Mater. Interfaces* **7**, 18560–18565 (2015).

57. Zheng, H. *et al.* Nanostructured tungsten oxide - Properties, synthesis, and applications. *Adv. Funct. Mater.* **21**, 2175–2196 (2011).

58. Jiang, C., Moniz, S. J. A., Wang, A., Zhang, T. & Tang, J. Photoelectrochemical devices for solar water splitting – materials and challenges. *Chem. Soc. Rev.* **46**, 4645–4660 (2017).

59. Wang, Z. & Hu, X. Electrochromic properties of TiO2-doped WO3 films spin-coated from Ti-stabilized peroxotungstic acid. *Electrochim. Acta* **46**, 1951–1956 (2001).

60. Deepa, M., Saxena, T. K., Singh, D. P., Sood, K. N. & Agnihotry, S. a. Spin coated versus dip coated electrochromic tungsten oxide films: Structure, morphology, optical and electrochemical properties. *Electrochim. Acta* **51**, 1974–1989 (2006).

61. Solarska, R., Jurczakowski, R. & Augustynski, J. A highly stable, efficient visible-light driven water photoelectrolysis system using a nanocrystalline WO3 photoanode and a methane sulfonic acid electrolyte. *Nanoscale* **4**, 1553 (2012).

62. Santato, C., Odziemkowski, M., Ulmann, M. & Augustynski, J. Crystallographically oriented mesoporous WO3 films: Synthesis, characterization, and applications. *J. Am. Chem. Soc.* **123**, 10639–10649 (2001).

63. Hodes, G., David, C. & Joost, M. Tungsten trioxide as a photoanode for a photoelectrochemical cell (PEC). *Nature* **260**, 312–313 (1976).

64. Mi, Q., Zhanaidarova, A., Brunschwig, B. S., Gray, H. B. & Lewis, N. S. A quantitative assessment of the competition between water and anion oxidation at WO3 photoanodes in acidic aqueous electrolytes. *Energy Environ. Sci.* **5**, 5694 (2012).

65. Shaner, M. R. *et al.* Photoelectrochemistry of core–shell tandem junction n–p+-Si/n-WO3 microwire array photoelectrodes. *Energy Environ. Sci.* **7**, 779 (2014).

66. Butler, M. a. Photoelectrolysis and physical properties of the semiconducting electrode WO 2. *J. Appl. Phys.* **48**, 1914–1920 (1977).

67. Mi, Q., Coridan, R. H., Brunschwig, B. S., Gray, H. B. & Lewis, N. S. Photoelectrochemical oxidation of anions by WO3 in aqueous and nonaqueous electrolytes. *Energy Environ. Sci.* **6**, 2646 (2013).

68. Hong, S. J., Lee, S., Jang, J. S. & Lee, J. S. Heterojunction BiVO4/WO3 electrodes for enhanced photoactivity of water oxidation. *Energy Environ. Sci.* **4**, 1781 (2011).

69. Nenadovic, M. T., Rajh, T., Micic, O. I. & Nozik, A. J. Electron transfer reactions and flat-band potentials of tungsten(VI) oxide colloids. *J. Phys. Chem.* **88**, 5827–5830 (1984).

70. Rühle, S. *et al.* Molecular adjustment of the electronic properties of nanoporous electrodes in dye-sensitized solar cells. *J. Phys. Chem. B* **109**, 18907–18913 (2005).

71. McNeill, A. R., Hyndman, A. R., Reeves, R. J., Downard, A. J. & Allen, M. W. Tuning the Band Bending and Controlling the Surface Reactivity at Polar and Nonpolar Surfaces of ZnO through Phosphonic Acid Binding. *ACS Appl. Mater. Interfaces* **8**, 31392–31402 (2016).

72. Hanson, E. L., Schwartz, J., Nickel, B., Koch, N. & Danisman, M. F. Bonding Self-Assembled, Compact Organophosphonate Monolayers to the Native Oxide Surface of Silicon. *J. Am. Chem. Soc.* **125**, 16074–16080 (2003).

73. Wick-Joliat, R. *et al.* Stable and tunable phosphonic acid dipole layer for band edge engineering of photoelectrochemical and photovoltaic heterojunction devices. *Energy Environ. Sci.* **12**, 1901–1909 (2019).

74. Seger, B. *et al.* Silicon protected with atomic layer deposited TiO2: durability studies of photocathodic H-2 evolution. *Rsc Adv.* **3**, 25902–25907 (2013).

75. Cui, W., Niu, W., Wick-Joliat, R., Moehl, T. & Tilley, S. D. Operando deconvolution of photovoltaic and electrocatalytic performance in ALD TiO 2 protected water splitting photocathodes. *Chem. Sci.* **9**, 6062–6067 (2018).

76. Hoex, B., Schmidt, J., Pohl, P., van de Sanden, M. C. M. & Kessels, W. M. M. Silicon surface passivation by atomic layer deposited Al2O3. *J. Appl. Phys.* **104**, 044903 (2008).

77. Hoex, B., Heil, S. B. S., Langereis, E., van de Sanden, M. C. M. & Kessels, W. M. M. Ultralow surface recombination of c-Si substrates passivated by plasma-assisted atomic layer deposited Al2O3. *Appl. Phys. Lett.* **89**, 042112 (2006).

78. von Gastrow, G. *et al.* Analysis of the Atomic Layer Deposited Al2O3 field-effect passivation in black silicon. *Sol. Energy Mater. Sol. Cells* **142**, 29–33 (2015).

79. Alexander V. Naumkin, Anna Kraut-Vass, Stephen W. Gaarenstroom, C. J. P. *NIST X-ray Photoelectron Spectroscopy Database*. (2012). doi:10.18434/T4T88K

80. Nilsing, M., Lunell, S., Persson, P. & Ojamäe, L. Phosphonic acid adsorption at the TiO2 anatase (1 0 1) surface investigated by periodic hybrid HF-DFT computations. *Surf. Sci.* **582**, 49–60 (2005).

81. Wagstaffe, M. *et al.* An Experimental Investigation of the Adsorption of a Phosphonic Acid on the Anatase TiO 2 (101) Surface. *J. Phys. Chem. C* **120**, 1693–1700 (2016).

82. Luschtinetz, R. *et al.* Adsorption of phosphonic and ethylphosphonic acid on aluminum oxide surfaces. *Surf. Sci.* **602**, 1347–1359 (2008).

83. Kukli, K. *et al.* Real-Time Monitoring in Atomic Layer Deposition of TiO 2 from TiI 4 and H 2 O−H 2 O 2. *Langmuir* **16**, 8122–8128 (2000).

84. Haukka, S., Lakomaa, E. L., Jylha, O., Vilhunen, J. & Hornytzkyj, S. Dispersion and distribution of titanium species bound to silica from titanium tetrachloride. *Langmuir* **9**, 3497–3506 (1993).

85. Bronneberg, A. C., Höhn, C. & Van De Krol, R. Probing the Interfacial Chemistry of Ultrathin ALD-Grown TiO2 Films: An In-Line XPS Study. *J. Phys. Chem. C* **121**, 5531–5538 (2017).

86. Fall, C. J., Binggeli, N. & Baldereschi, A. Deriving accurate work functions from thin-slab calculations. *J. Phys. Condens. Matter* **11**, 2689–2696 (1999).

87. Shan, B. & Cho, K. Ab initio study of Schottky barriers at metal-nanotube contacts. *Phys. Rev. B* **70**, 233405 (2004).

88. Li, Z. *et al.* 9.2%-efficient core-shell structured antimony selenide nanorod array solar cells. *Nat. Commun.* **10**, 125 (2019).

89. Yang, W. *et al.* Adjusting the Anisotropy of 1D Sb 2 Se 3 Nanostructures for Highly Efficient Photoelectrochemical Water Splitting. *Adv. Energy Mater.* **8**, 1–11 (2018).

90. Lee, H. *et al.* Cu-Doped NiO x as an Effective Hole-Selective Layer for a High-Performance Sb 2 Se 3 Photocathode for Photoelectrochemical Water Splitting. *ACS Energy Lett.* **4**, 995–1003 (2019).

91. Yang, W. *et al.* Time-Resolved Observations of Photo-Generated Charge-Carrier Dynamics in Sb 2 Se 3 Photocathodes for Photoelectrochemical Water Splitting. *ACS Nano* **12**, 11088–11097 (2018).

92. Prabhakar, R. R. *et al.* Photocorrosion-resistant Sb 2 Se 3 photocathodes with earth abundant MoS x hydrogen evolution catalyst. *J. Mater. Chem. A* **5**, 23139–23145 (2017).

93. Wick, R. & Tilley, S. D. Photovoltaic and Photoelectrochemical Solar Energy Conversion with Cu 2 O. *J. Phys. Chem. C* **119**, 26243–26257 (2015).

94. Moehl, T., Cui, W., Wick-Joliat, R. & Tilley, S. D. Resistance-based analysis of limiting interfaces in multilayer water splitting photocathodes by impedance spectroscopy. *Sustain. Energy Fuels* (2019).

95. Paracchino, A., Laporte, V., Sivula, K., Grätzel, M. & Thimsen, E. Highly active oxide photocathode for photoelectrochemical water reduction. *Nat. Mater.* **10**, 456–461 (2011).

96. Dow, J. D. & Allen, R. E. Surface defects and Fermi-level pinning in InP. *J. Vac. Sci. Technol.* **20**, 659–661 (1982).

97. Tung, R. T. Chemical Bonding and Fermi Level Pinning at Metal-Semiconductor Interfaces. *Phys. Rev. Lett.* **84**, 6078–6081 (2000).

98. Lenfant, S. *et al.* Electron Transport through Rectifying Self-Assembled Monolayer Diodes on Silicon: Fermi-Level Pinning at the Molecule−Metal Interface. *J. Phys. Chem. B* **110**, 13947–13958 (2006).

99. Le Formal, F., Sivula, K. & Grätzel, M. The Transient Photocurrent and Photovoltage Behavior of a Hematite Photoanode under Working Conditions and the Influence of Surface Treatments. *J. Phys. Chem. C* **116**, 26707–26720 (2012).

100. Steier, L. *et al.* Understanding the Role of Underlayers and Overlayers in Thin Film Hematite Photoanodes. *Adv. Funct. Mater.* **24**, 7681–7688 (2014).

Acknowledgements

I want to acknowledge several people who supported me in the last years and therefore largely contributed to the success of this doctoral thesis:

Firstly, a big thank you goes to Prof. Dr. David Tilley. He hired me as his first PhD student and always supported and motivated me. While being an excellent supervisor scientifically, he also creates a respectful, helpful and pleasant atmosphere in our group. His helpfulness, the transparency when it comes to decisions affecting the group and the way he treats each student according to their individual needs is inspiring and worth copying.

I am thankful to Prof. Dr. Roger Alberto and Prof. Dr. Jürg Osterwalder, the members of my PhD committee, for fruitful discussions during our annual committee meetings or on other occasions. Roger also supervised my Masters Thesis, which brought me on the track of solar energy conversion and triggered my interest in this topic.

I am deeply grateful to all current Tilley Group members: Dr. Thomas Moehl, Laurent Sévery, Wei Cui, Rajiv Ramanujam Prabhakar, Jihye Suh, Xi Zhang, Jonas Zurflüh, Dhananjeya Kumaar, Casey Beall and Dr. Laxman Gouda as well as the former group members: Dr. Magda Marszalek, Dr. Wilman Septina, Connor Firth, Marin Nikolic, Dr. Wenzhe Niu, Antony Sibilia. All of them have become good friends over the years and it was mostly thanks to them that I always liked coming to the lab, even if the progress in my project was sometimes very slow. We spent uncountable hours in the lab or seminar rooms together, trying to make sense of strange electrochemistry results or whatever. But mainly our countless apéros, karaoke parties, boardgame nights, barbeque evenings, group trips, extended coffee breaks etc. will always remain in my memories.

I want to specially highlight Dr. Thomas Moehl, who, with angelic patience, taught me everything I know about electrochemistry, impedance measurements and more. His huge knowledge and humorous nature are very inspiring.

My Master student, Dhananjeya Kumaar, always asks the tough questions and therefore helps to deepen the understanding and push our project forward.

It was always a pleasure working with Dr. Tiziana Musso and Dr. Marcella Ianuzzi, who backed up our sometimes counterintuitive experimental results with DFT calculations and therefore helped a lot to interpret our results.

Dr. Sebastian Siol from Empa was always very helpful when it came to XPS measurements and Johannes Löckinger, also from Empa, increased the impact of our work by demonstrating that the whole concept of this project can also be applied to photovoltaics.

Furthermore, I want to thank the whole Department of Chemistry, the CMSZH graduate school as well as the URPP LightChEC for their financial support, providing the infrastructure and organizing events such as summer schools and the graduate school retreat.

A special thank you goes to the workshop team Hanspeter Stalder and Serkan Sariyildiz as well as the administrative staff, Ramona Erni, Nathalie Melusky-Fichter, Dr. Sabine Stockhause, Dr. Valeria Mozzetti Rohrseitz and Dr. Elisabetta Vannoni Thäler for taking care of all the bureaucratic issues.

A very big thanks also goes to all my friends and family, especially my parents Heidi and Urs for their lifelong support, for financing my undergraduate studies and for taking care of Noelia very frequently. And, most importantly, I want to thank my amazing wife Evelyne and my sweet daughter Noelia, who always made me forget any struggle in no time. They are the best I could ever wish for.